Lensless microscopy using visible and extreme ultraviolet radiation

Noom, D.W.E.

2016

document version
Publisher's PDF, also known as Version of record

VRIJE UNIVERSITEIT

Lensless microscopy using visible and extreme ultraviolet radiation

ACADEMISCH PROEFSCHRIFT

ter verkrijging van de graad Doctor aan
de Vrije Universiteit Amsterdam,
op gezag van de rector magnificus
prof.dr. V. Subramaniam,
in het openbaar te verdedigen
ten overstaan van de promotiecommissie
van de Faculteit der Exacte Wetenschappen
op donderdag 30 juni 2016 om 11.45 uur
in de aula van de universiteit,
De Boelelaan 1105

door

Daniël Wilhelmus Emile Noom

geboren te Assendelft

promotor:	prof.dr. K.S.E. Eikema
copromotor:	dr. S.M. Witte

reading committee:	prof.dr. G. Cerullo
	prof.dr. W. Steenbergen
	prof.dr. D. Iannuzzi
	prof.dr. A.P. Mosk
	prof.dr. P.C.M. Planken

Nederlandse Organisatie voor Wetenschappelijk Onderzoek

The work in this thesis was performed at the LaserLaB Amsterdam, VU University Amsterdam. Investment support was provided by the Nederlandse Organisatie voor Wetenschappelijk Onderzoek (NWO) and the Seventh Framework Programme of the European Commission through JRA INREX.

Contents

Chapter 1

Introduction

1.1 Soft X-ray microscopy

The first microscopes used light and lenses, and gave us an insight in the world of living things which are impossible to see with the naked eye. Their use has been expanded by new imaging techniques and improvements in detectors and sources, and there is now a broad range of scattering and probing techniques that vastly improved the resolution and applications of microscopy. Wavelengths even outside of the infrared to ultraviolet regime are used, as are electrons, while lenses are sometimes omitted from imaging systems. There is an ongoing effort in many research groups to get the most information out of a sample and reach the highest resolution [1].

An important aspect of a microscope is its ability to resolve small features. This can be quantified by the spot size of a point source after the imaging system. This is limited by the diffraction limit, which can be defined as

$$d = \frac{\lambda}{2n \sin \theta}, \tag{1.1}$$

where d is the distance between resolvable point sources, λ is the wavelength of the illuminating light source, and $n \sin \theta$ the effective numerical aperture of the imaging system (which depends on the refractive index n and the total angle θ of the collected light). Note that it is not always clear what 'resolvable' means; this depends on the coherence of the source [2].

Since it is difficult to reach a numerical aperture far higher than 1.6, we can either use techniques that circumvent the diffraction limit [3, 4] or use shorter wavelengths. This is one reason to look at sources in the UV and X-ray regime. There is, however, another reason to use much

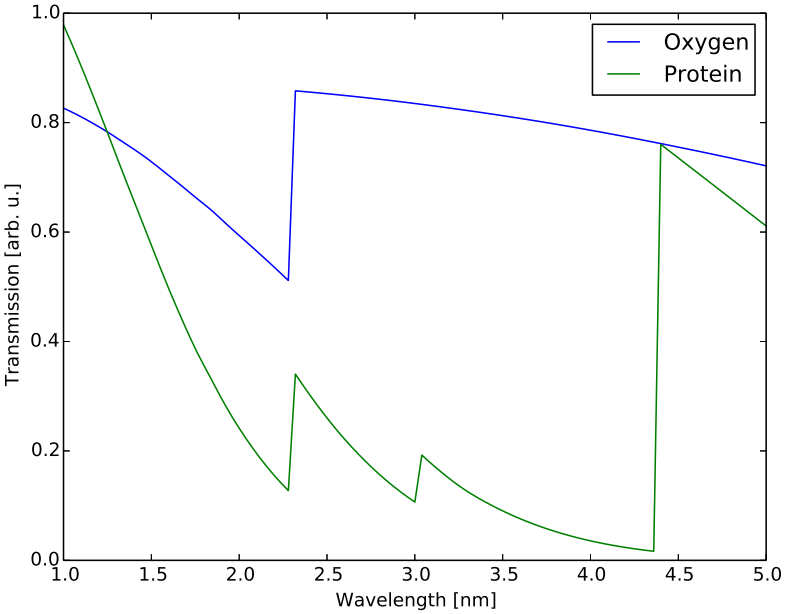

FIGURE 1.1: Absorption of atomic oxygen and average protein consistency around the so called water window. The absorption of proteins in this wavelength region is modeled by using a ratio of elements of CO_2N_4. The levels are not scaled according to the particle densities of water molecules and proteins. Data are taken from [5].

shorter wavelengths, in the soft-X-ray region of the spectrum ($<$10 nm). When the photon energy of the radiation increases beyond the binding energy of an electron in the K-shell of an atom, which is the energy shell closest to the nucleus, there is a sudden increase in absorption of the radiation, and the energy is said to be above the K-edge of the atom. In the wavelength region between 2.34 and 4.4 nm, the photon energy is higher than the K-edge of carbon, and lower than the K-edge of oxygen. This gives a natural contrast between water and proteins, as shown in Fig. 1.1, which is very interesting for microscopy of biological samples.

One way to generate soft X-rays is by using synchrotron light sources. In these large scale facilities high-energy electrons are kept on a circular orbit by bending magnets, leading to short wavelength emission. Because of the high demand for beam time, time slots are limited at synchrotrons, and there is usually little time to set up an experiment and take data.

However, by using these sources with either Fresnel zone plates or diffraction techniques, one can reach nanometer-level resolution. For example, in 2004, X-ray tomography resulted in 60 nm resolution 3-D reconstruction of a yeast cell [6], and in 2005 15 nm resolution was reached in imaging test objects [7].

Free electron lasers have even less beamlines available, but can reach much higher peak intensities than synchrotrons. Even proteins in nanocrystals have been imaged by using femtosecond hard X-ray pulses; by using such short pulses, imaging can be completed before damage from the energetic photons occurs [8].

Another way to shorten the wavelength for improved resolution is by using electrons instead of electromagnetic radiation. Accelerated electrons illuminate a sample and the absorption profile is measured, or the electrons are scanned over a surface where the radiation or e.g. secondary electrons produced by loss processes is used to probe the location of scattering. Transmission electron microscopes have reached 50 pm resolution [9].

1.2 Lensless imaging

In the previous section already diffraction was mentioned as a method for imaging. If diffraction from objects is recorded with a digital camera, then this opens up the possibility of eliminating lenses from an imaging setup by using algorithmic phase reconstruction on a computer (see Fig. 1.2). Without lenses, the propagated electric field after a sample forms a diffraction pattern. If the phase and the intensity of the electric field are known at a certain distance from the sample, it can be propagated back to the sample to form an image.

If only the intensity of the electric field is measured (as is the usual case with a charge coupled device (CCD)), the phase information is lost, and recovery is an underdetermined problem. More information is required, which can come from many sources. It can be added in a holographic setup [10], or it can be done via multiple measurements, for example by scanning an aperture used for illumination [11]. Another possibility is to exploit known information about e.g. the maximum size of a sample. While direct reconstruction of the phase is possible in certain measuring conditions, usually phase reconstruction is done via iterative algorithms.

Image reconstruction from diffraction patterns can be performed with

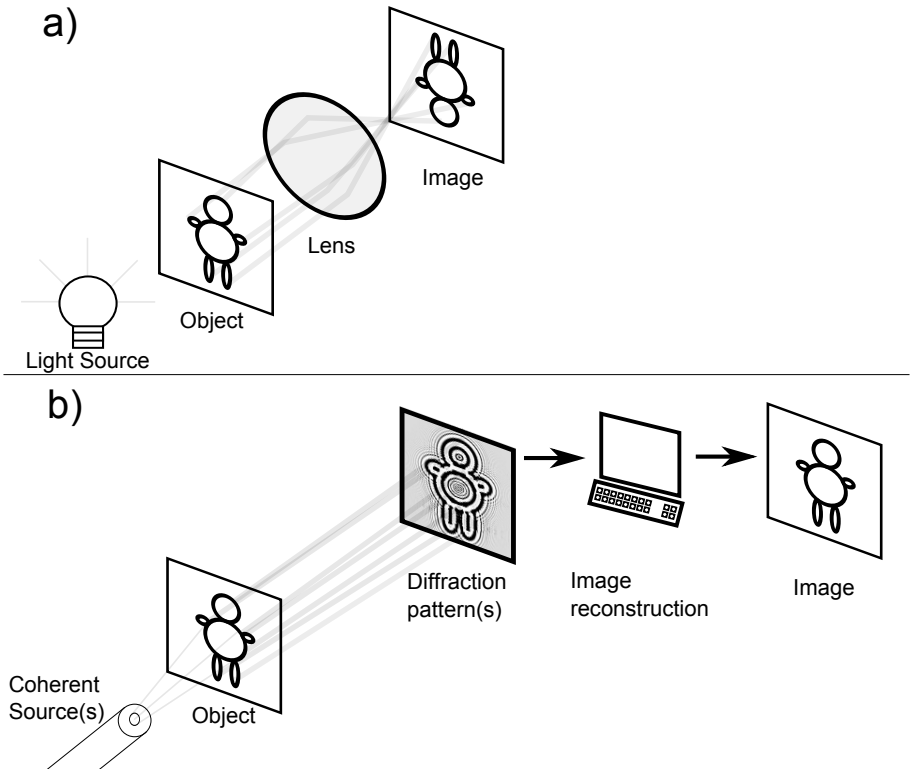

FIGURE 1.2: a) Image formation using a lens. b) Using a detector and a computer to calculate the image of the object.

infrared and visible wavelengths (as shown in Chapter 3 and 4), but also at short wavelengths. This is particularly appropriate, as traditional optics of any form for wavelengths below 100 nm are hard to produce. An interesting way to generate these short wavelengths is with powerful ultrafast pulsed lasers. However, as will be explained in the next two sections, this typically leads to broad bandwidth emission, which requires new methods to perform diffractive (lensless) imaging.

1.3 Coherent short wavelength generation with lasers

Lensless imaging via diffraction requires spatially coherent radiation, and the usual approach to generate spatially coherent radiation is to use

lasers. This requires population inversion, a situation where an excited state has a higher population than a lower state.

Because the ratio between the rate of spontaneous decay (A) to the rate of stimulated absorption and emission (B) scales with the wavelength λ as

$$\frac{A}{B} \propto \lambda^{-3}, \tag{1.2}$$

shorter wavelengths are much harder to generate using amplification by stimulated emission.

Another way of generating short-wavelength radiation is by using high-harmonic generation (HHG), discussed in more detail in Chapter 2. This is an extension of harmonic generation into the non-perturbative regime. A simple way to view the process is the three-step model [12]: First, the laser electric field deforms the Coulomb potential so that an electron (wavepacket) can tunnel out of the atom and becomes ionized. Then the electron gains energy in the electric field of the surrounding radiation. When the electric field of the laser field reverses sign, the electron (wavepacket) returns to the parent ion, recombines with the parent ion, and short wavelength radiation is released in a burst. This produces radiation with photon energies up to a certain threshold, called the cutoff, which is determined by the intensity and wavelength of the fundamental laser light driving the HHG process, and the atoms used in the process. A peak power on the order of 10^{14} W cm^{-2} is required for HHG, leading to a typical conversion efficiency of 10^{-6}.

To reach high intensities without using an excessive amount of average power, pulsed lasers are used. Ultrashort pulses necessarily have a large bandwidth, and a commonly used gain material for the required ultrashort pulse generation and amplification is Ti:sapphire. It has a full-width at half-maximum (FWHM) fluorescence bandwidth of 230 nm around a peak emission wavelength of 780 nm [13].

A typical Ti:sapphire based laser oscillator can generate pulses of $\sim$ 10 fs duration, but the pulse energy is only 10 nJ for a 1W laser at a 100 MHz repetition rate. To increase this to the mJ level, which is needed to achieve the required peak intensity for HHG, pulses are amplified at a much lower repetition rate. There are two main techniques to obtain enough gain to reach the peak power required for HHG: either by using stimulated emission in laser materials or by optical parametric amplification.

By using Ti:sapphire in traditional multipass laser amplifiers, peak power levels over a petawatt have been reached [14], but with one shot

in 20 minutes in a laser facility. Because not all energy that is absorbed by the crystals is used for amplification, there is heating of the material, which needs to be controlled and can deform the beam or damage the crystal. An important limitation apart from amplification of fluorescence and parasitic lasing is the gain narrowing by the laser material. For this reason Ti:sappire systems are limited to pulses longer than ~ 17 fs [15].

In contrast, we have developed (see chapter 2 and 5) a system based on optical parametric amplifiers (OPA) [16, 17]. These devices do not need to store energy, but energy is transferred directly from one beam to two other beams (the signal and idler beam) through a nonlinear interaction in a crystal. A simple way to view this process is that one photon is split up in two lower energy photons, and this process can be stimulated, so that it effectively acts as an amplifier. Because the medium is not excited this greatly relaxes cooling conditions and no lasing inside the material is induced (although other processes such as generation of spontaneous parametric fluorescence can occur).

One difficulty with these systems is that the required high peak powers of 'pump' pulses and amplified ultrashort pulses can damage the nonlinear crystals and other optics. After amplification reflective optics can be used, but to protect the crystals used for amplification, we need a technique called chirped pulse amplification. Here pulses are stretched in time to lower the peak power by an extremely dispersive optical setup, and after amplification this is reversed to compress the pulse back again to a short pulse.

1.4 Lensless imaging with broadband sources

Although short pulse lasers can generate short wavelengths through the HHG process, the generated radiation consists of many 'harmonics' and therefore effectively has a broad bandwidth. However, phase reconstruction in imaging traditionally requires a narrow bandwidth. If a broadband source is present it is also possible to narrow the spectrum using a monochromator. This means the rest of the spectrum is not used, and even the used part of the spectrum incurs losses due to the optics that are used, such as gratings. So because high-harmonic sources are inherently broadband, and it is important to use as much flux as possible to prevent long measurement times, we want to directly use broadband sources for lensless imaging.

If a broadband source is used, and the detector used to measure the

diffraction pattern cannot differentiate between different wavelengths, then the diffraction patterns will be blurred, reducing the image quality or even preventing image reconstruction altogether. When working with visible light, red-green-blue (RGB) detectors can be used, while for X-rays photon energies some energy resolution has been obtained by using the pixel brightness of single-photon events on a CCD camera [18]. To get a much better resolution in the separation of wavelengths, we show that it is possible to combine Fourier transform spectroscopy and microscopy [19], and in Chapter 6 this is demonstrated for high-harmonic generation and lensless imaging.

Similar to Fourier-transform spectroscopy, this technique requires two pulses which are coherent with respect to each other, and with an adjustable time delay between them. This can be achieved by using a Michelson interferometer or similar devices. Each pixel of the image sensor (typically a CCD) can then be treated as an intensity detector in a Fourier transform spectroscopy experiment. The two main challenges in achieving this are the required stability of the interferometer, and the disturbing influence of the first pulse on the second pulse in high-harmonic generation. In section 6.6 these challenges are met, and a stable interferometer is shown to be feasible even in the soft X-ray region.

1.5 Outline of this thesis

One of my main goals during my work for this PhD research was to develop a coherent extreme ultraviolet/soft-X-ray source for imaging at short wavelengths, based on parametric ultrashort pulse amplification and subsequent high-harmonic generation. For this I first developed a special pump laser that is based on newly developed pulsed diode-pumped Nd:YAG gain modules that recently became commercially available. Control of the effects of high thermal stress and dealing with high peak powers in this system resulted in the article described in section 5.1.

In section 5.2 the optical parametric amplifier is described which is used to generate powerful ultrashort pulses for high-harmonic generation of extreme ultraviolet radiation.

At the same time we also needed to develop techniques for lensless imaging, mainly focused on the ability to use a broadband source, such as light produced by high-harmonic generation. We first looked at visible

light broadband sources as a model system. By using Fourier-transform spectroscopy in combination with microscopy we obviated the need for narrowband sources. At the same time, since this technique gave us information at different wavelengths we tried to use this in an iterative algorithm, which is detailed in Chapter 6.

Since this lensless imaging technique used for radiation at multiple wavelengths worked very well, we investigated the possibilities for microscopy at visible and infrared wavelengths. Even though lenses are easily manufactured for this spectral region, the reconstruction method used for lensless imaging gives better phase information than can be obtained in a normal bright-field microscope. Lensless microscopes can also be easier to set up, and be much smaller. The usefulness of this approach is demonstrated with imaging a sample of neurons. In this case we show that absorption pictures do not give much information about the structure of the sample, while the phase contrast picture shows much more detail, as described in Chapter 3.

In the first implementation, the image acquisition rate of our microscope was limited by the need to change the illumination wavelengths sequentially by computer. However, with an RGB camera one can in principle record three patterns for three different wavelengths at the same time. This does not only speed up the acquisition process, but also solves the 'blurring' problem of recording moving objects. In this manner we have been able to do lensless imaging at video rates, so that movies could be recorded. The results of these efforts are shown in Chapter 4, and the movies can be found with the original published article [20].

Chapter 2

Principles of lensless imaging, short-pulse physics and harmonic upconversion

2.1 Phase reconstruction for lensless imaging

For our lensless imaging experiments we need phase reconstruction procedures (see section 1.2). While in some cases it is possible to directly retrieve the phase from an experiment, iterative algorithms are often used because there are far less strict demands on the optical system. In the next paragraphs, I will derive a transformation between diffraction patterns resulting from different wavelengths and then outline our algorithm used in phase retrieval.

2.1.1 Propagation of the electric field of light

Transformation of the diffracted electric field $\mathbf{E}$ between different wavelengths is derived in this section in the scalar approximation. From Maxwell's equations, we can derive the vector wave equation:

$$\nabla^2\mathbf{E} - \frac{1}{c^2}\frac{\partial^2\mathbf{E}}{\partial t^2} = 0, \tag{2.1}$$

and for monochromatic fields, we can use $e^{-i\omega t}$ for the time dependent factor, write $k = \omega/c$, and use the *scalar approximation* by only looking at one component of the electric field vector to get the scalar Helmholtz equation

$$(\nabla^2 + k^2)E = 0. \tag{2.2}$$

By looking at the field as a plane wave e^{ikz} in the z-direction multiplied by an envelope function $\Theta(x, y, z)$, we can insert this into equation 2.2, and apply *slowly varying envelope approximation* to discard the

$d^2\Theta/dz^2$ terms, to get to the paraxial wave equation [21]

$$\frac{d^2\Theta}{x^2} + \frac{d^2\Theta}{dy^2} + 2ik\frac{d\Theta}{z} = 0. \tag{2.3}$$

A solution to this equation for a wave traveling from the $(x', y', 0)$-plane to the (x, y, z)-plane is

$$\Theta(x, y, z) = \frac{1}{i\lambda z}\iint \Theta(x', y', 0)e^{\frac{i\pi}{\lambda z}[(x-x')^2+(y-y')^2]}dx'dy' \tag{2.4}$$

where we can plug in the e^{ikz}-term and replace k with $2\pi/\lambda$ to reach the Fresnel integral:

$$E(x, y, z) = \frac{e^{i\frac{2\pi z}{\lambda}}}{i\lambda z}\iint E(x', y', 0)e^{\frac{i\pi}{\lambda z}[(x-x')^2+(y-y')^2]}dx'dy' \tag{2.5}$$

To facilitate quick calculations using the fast Fourier transform (FFT) method, we recognize that this integral can be written as a convolution

$$E(x, y, z) = g(x, y) * h(x, y) = \iint g(x', y')h(x - x', y - y')dx'dy' \tag{2.6}$$

where

$$g(x', y') = E(x', y', 0) \tag{2.7}$$

and

$$h(x - x', y - y') = \frac{e^{i\frac{2\pi z}{\lambda}}}{i\lambda z}e^{\frac{i\pi}{\lambda z}[(x-x')^2+(y-y')^2]}. \tag{2.8}$$

The Fourier transform of $h(x, y)$ is

$$H_F(f_x, f_y) = \mathcal{F}\left\{\frac{e^{i\frac{2\pi z}{\lambda}}}{i\lambda z}e^{\frac{i\pi}{\lambda z}[(x-x')^2+(y-y')^2]}\right\} = e^{i\frac{2\pi z}{\lambda}}e^{-i\pi\lambda z(f_x^2+f_y^2)}, \tag{2.9}$$

which is the transfer function when using the scalar- and slowly varying envelope approximation. The last approximation is also called the Fresnel approximation [22], and we will see that in the Fourier domain this requires small spatial frequencies, or small angles and is therefore called the paraxial approximation.

To find the transfer function without the Fresnel approximation, we note that the electric field can be written as the Fourier transform of its angular spectrum:

$$E(x, y, z) = \iint A(f_x, f_y, z)e^{i2\pi(f_x x+f_y y)}df_x df_y \tag{2.10}$$

with

$$A(f_x, f_y, z) = \iint E(x, y, z) e^{-i2\pi(f_x x + f_y y)} dx dy \tag{2.11}$$

If we insert this into eq. 2.2 we get the requirement that

$$\frac{d^2}{dz^2} A(f_x, f_y, z) + \left(\frac{2\pi}{\lambda}\right)^2 (1 - (\lambda f_x)^2 - (\lambda f_y)^2) A(f_x, f_y, z) = 0 \tag{2.12}$$

where we find the solution

$$A(f_x, f_y, z) = A(f_x, f_y, 0) e^{i\frac{2\pi z}{\lambda}\sqrt{1-(\lambda f_x)^2-(\lambda f_y)^2}}, \tag{2.13}$$

which means the transfer function using only the scalar approximation is

$$H_S = e^{i\frac{2\pi z}{\lambda}\sqrt{1-(\lambda f_x)^2-(\lambda f_y)^2}}. \tag{2.14}$$

If we want to propagate the electric field we can now use a two-dimensional FFT and this transfer function for quick calculations.

We can check that for small angular frequencies we have

$$\sqrt{1 - (\lambda f_x)^2 - (\lambda f_y)^2} \approx 1 - \frac{(\lambda f_x)^2}{2} - \frac{(\lambda f_y)^2}{2} \tag{2.15}$$

which gives us the Fresnel approximation.

We can now propagate optical fields numerically along an optical axis, or between wavelengths, which forms the basis for Fresnel-type phase retrieval algorithms. More details can be found in Chapter 6, and specifically in Chapter 6.6.5.

2.1.2 Multi-color phase retrieval algorithm principle

Various phase-retrieval algorithms [23] use intensity diffraction patterns from different parallel planes to determine the phase of the electric field. Even though no phase information is measured, the propagation between the planes depends on the phase of the electric field. This can be used to iteratively reconstruct the total electric field by replacing intensity data with the measured intensity in one plane while keeping the phase information. Then this field is propagated to another plane, where again the phase is kept, but the intensity is replaced with the measured one at that plane. This procedure is then repeated at more planes or previous planes [24].

The algorithm we used is a variant of this where we do not propagate between spatially separated planes but between wavelengths, by using

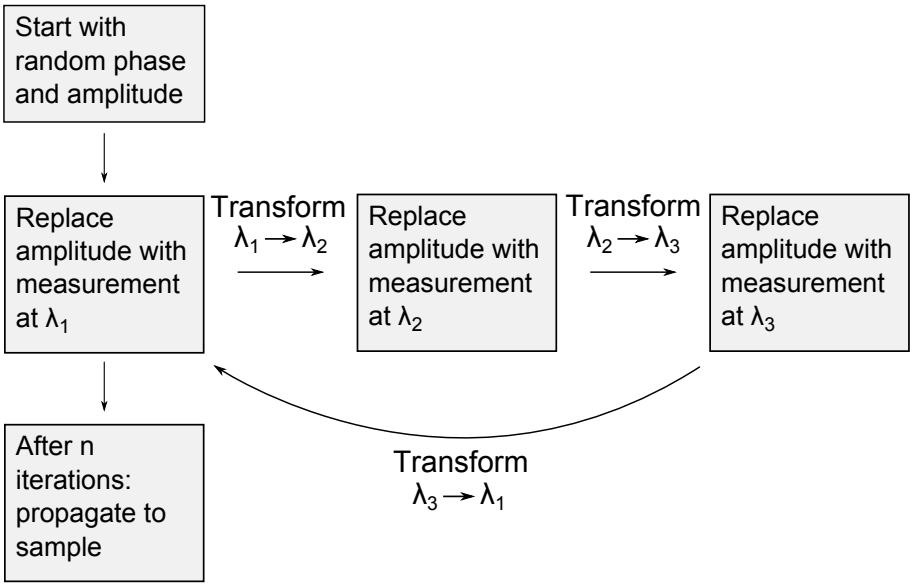

FIGURE 2.1: The multi-wavelength phase retrieval algorithm illustrated for three wavelengths. It can easily be expanded to more than three wavelengths or restricted to two. The number of iterations n can be fixed beforehand or determined during the process. Wavelengths are transformed using the procedure described at the end of section 2.1.1.

the following procedure: we propagate from a diffraction pattern at a certain distance d to the sample by using a Fourier transform and eq. 2.14 with a distance $z = -d$. To change to a different wavelength we divide the phase by the current wavelength used, and multiply it by the new wavelength. We can then propagate back to the same distance by using eq. 2.14 again, but now by using $z = d$. This is a complete transformation of a diffraction pattern at one distance from one wavelength to another.

The algorithm is illustrated for three wavelengths in Fig. 2.1. After starting out with a random phase and amplitude, the amplitude is replaced using the measured intensity of a diffraction pattern at wavelength λ_1. Then we propagate to the second wavelength, and replace the amplitude with the measurement at λ_2. We continue this procedure until we reach the last wavelength and then propagate to the first. After stopping the iterations we propagate back to the sample by using eq. 2.14 one more time to get the phase and amplitude at the sample. More details can be found in Chapters 4 and 6.

2.2 Picosecond and femtosecond pulses

2.2.1 Mode-locking

In this thesis ultrashort pulses are used in the range of a tens of fs to tens of ps. These pulses are generated by different types of modelocked lasers. The general principle is that many modes of a laser resonator are made to lase simultaneously. Pulses can be created as a result of interference of these modes. More modes lead to shorter pulses. For this process to happen, the phase of all the modes need to be locked to each other, hence the term mode-locked laser [25]. There are several different types of modelocking mechanisms, which are typically more easily understood in the time domain. In general one wants a situation where higher intensities have a higher total net gain than lower intensities. By definition this requires nonlinear processes. This can be done in several ways, for example by using a polarization change dependent on intensity and polarizers [26], using saturable absorbers where higher intensities have lower losses [27], or using the optical Kerr effect [28] to, for example, have a higher intensity beam be shaped in a different way which overlaps better with the pump laser for more gain.

The Nd:YVO_4 picosecond modelocked laser that is a part of the pump laser (see Chapter 5.1) uses a semiconductor saturable absorber mirror (SESAM) [29] as modelocking element. It has a certain modulation depth, which is the difference between the power lost when it is saturated and when it is not. The saturation threshold is given as a fluence, which is energy per unit area, and the recovery time gives an indication of how long the absorber remains saturated after a pulse has passed. Modelocking is self starting with a SESAM if the right saturation fluence and recovery time is chosen. Small disturbances lead to pulses that experience less loss in the SESAM due to the higher intensity. After a while such a laser works purely pulsed in a regular pattern that is normally repeated with the round-trip time of the resonator.

The femtosecond modelocked laser used in this thesis uses a different mode-locking mechanism: a 'soft Kerr lens', This is based on the Kerr effect which results in a refractive index increase proportional to the intensity of the light beam in the laser crystal. This leads to intensity-dependent focusing, which can be used to induce losses or increase the gain of a beam (pulse) propagating in the resonator. In this manner pulses can be generated down to approximately 5 fs.

2.2.2 Damage processes

For the high-power laser system developed during this thesis, we are limited in peak intensity by damage to optics in the pump laser and the optical parametric amplifier system. The high *average* power is also an important issue when working with the system, because of finite damage thresholds of power meters and filters. We look at these issues by using the treatment in chapter 11 of Koechner [13].

It is possible to define the damage threshold by looking at the onset of output performance degradation, because this does not necessarily occur when visible defects are present. However, because in our system diffraction effects are an important source of damage, a visible defect can lead to hotspots at other components and damage more optics. This is why we check components using cameras, look for intensity hotspots before fully amplifying our beam, and immediately turn the system off if any damage occurs.

In general, and also noticeable in this system, surfaces are the most prone to damage. This is due to the fact that many kinds of defects only occur there, such as surface contamination and polishing imperfections. Coatings also generally have lower damage thresholds than the substrates they are on. Because of different interference effects at the entrance and exit surfaces of optics, the exit intensity I_{ex} is higher than the entrance intensity I_{en} by a factor [13]

$$\frac{I_{ex}}{I_{en}} = \left(\frac{2n}{n+1}\right)^2, \tag{2.16}$$

where n is the refractive index of the material, so exit surfaces are more prone to damage than entrance surfaces.

Values for damage thresholds given by manufacturers are usually not measured with the same beam parameters as in our setup. Therefore, some scaling laws are needed to estimate damage thresholds for a setup. Nanosecond pulses are mostly used for quoted damage thresholds, and for a scaling parameter τ^α for a pulse duration τ, experiments have shown α to be between 0.3 and 0.6 [13] for dielectric materials. This means that the damage threshold intensity goes up by roughly an order of magnitude if ps instead of ns pulses are used.

2.2.3 Stretching and compressing ultrashort pulses

One of the main goals of our research is imaging using short wavelength radiation produced by high-harmonic generation, which requires high-

intensity laser pulses. In sections 2.3 and 5.2 the amplification of these pulses in an optical parametric amplifier is discussed. In this process, pump pulses of tens of picoseconds are used, and seed pulses should be about one third of this length for the highest conversion efficiency [30]. Pulses generated at the Ti:sapphire oscillator are only tens of femtoseconds long and need to be stretched.

Short pulses necessarily have a broad range of frequency components, and if we apply group velocity (or delay) dispersion by means of a grating pair setup, we can delay the various spectral components in the spectrum of the pulses in a nonlinear way. In effect the pulse then becomes 'chirped' and stretches in length. It also means that the peak intensity goes down, which allows amplification to a higher energy. After this amplification the chirp has to be compensated in the 'compressor' (using e.g. gratings in a different geometry than in the stretcher) to obtain a short pulse again. The shortest possible pulse for a given spectrum is called Fourier- or transform-limited, and here the phases of the spectral components have a linear relation with each other. The simplest form of stretching is to apply a quadratic spectral phase to a pulse.

The group delay dispersion (GDD) D_2 at an angular frequency ω is a property of an optical element. It depends on the induced change in spectral phase ϕ by [31]

$$D_2(\omega) = \frac{\partial^2 \phi}{\partial \omega^2}. \tag{2.17}$$

The GDD per unit length is the group velocity dispersion (GVD). For tranform-limited pulses with length τ_0, the pulse length after passing an optical element is

$$\tau_c = \tau_0 \sqrt{1 + \left(\frac{D_2}{\tau_0^2}\right)^2} \tag{2.18}$$

For a large dispersion ($D_2 \gg \tau_0^2$) the resulting chirped pulse length can be estimated by

$$\tau_c \approx \frac{D_2}{\tau_0} \tag{2.19}$$

From this it is clear that short pulses are more easily stretched; to stretch a Fourier-limited 10 fs pulse to 10 ps, a GDD of $D_2 \approx 10^5$ fs^2 is needed, which is easy to accomplish. However, for stretching a Fourier-limited 10 ps pulse to 60 ps, we need a GDD on the order of 10^9 fs^2, which is quite unpractical.

It is possible to stretch pulses by passing them through a transparent material, because of its dispersion. Different refractive indices at differ-

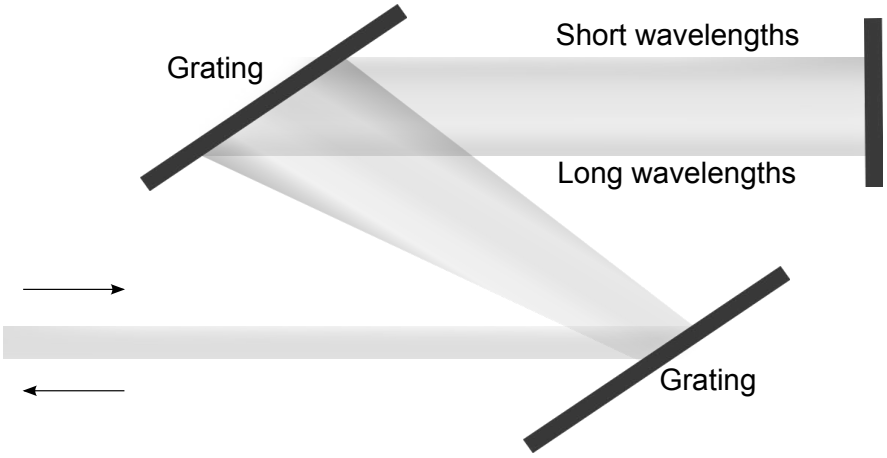

FIGURE 2.2: The -1st diffraction order off two gratings introducing a different path length which depends nonlinearly (mostly quadratically) on the wavelength. In this configuration negative GDD is produced, which is typically used to compress pulses after amplification. The end mirror is used to remove the transverse separation of wavelengths and doubles the total GDD.

ent wavelengths will cause a nonlinear time delay between components without a complex setup, but with the length and type of the material as the only control parameters. Spectral dependence of the angle of refraction or reflection can also be used to let different colors take a different path in a more complex setup using prisms or gratings (see Fig. 2.2). One of the challenges in these setups is to only have different delays between spectral components and not also have an angular or spatial dependence on wavelength. If this problem does occur it is often called spatial chirp. The GVD of fused silica is 35 fs^2 per mm at 800 nm, and a shoebox-sized grating based stretcher can reach 10^5 fs^2 at the same wavelength. From these values and eq. 2.18 it is clear that such methods can be used to effectively stretch femtosecond pulses, but are less practical for picosecond pulses.

2.2.4 Stretching picosecond pulses

The pulses generated at our Nd:YVO_4 oscillator are already 10 ps long, but need to be stretched to 60 ps to prevent damage to optics when the pulse energy reaches ~100 mJ after amplification. The high dispersion

required for picosecond pulses seems much harder to accomplish than stretching femtosecond pulses, but in this case the pulses do not need to be compressed again. This means higher orders of dispersion do not need to be controlled and known as well. Therefore we can use an intracavity etalon to stretch the pulses. They narrow the spectrum of the radiation in a cavity by reflecting radiation with wavelengths outside a small bandwidth, which is then coupled out of the cavity mode. Because light is also internally reflected inside the etalon, the phase is shifted in such a way to cause significant stretching for picosecond pulses.

While for a laser cavity a steady-state description of a intracavity etalon will suffice, for a regenerative amplifier it is more appropriate to use the theory of linear systems [32]. In our case we tried different etalons inside our regenerative amplifier and chose one that gave a pulse length closest to 60 ps. We used an etalon with 0.5 mm thickness and 30% reflectivity on both sides of the etalon, and reached a pulse length of 64 ps.

2.3 Optical parametric amplification

2.3.1 Parametric gain

Traditionally, laser amplification in e.g. Ti:sapphire crystals is used to amplify pulses from modelocked oscillator lasers to mJ-level energies. However, due to effects such as gain narrowing, this can limit the shortest pulse that can be amplified. A more versatile approach is to use parametric amplification (see also section 5.2), based on nonlinear crystals such as BBO. In an optical parametric amplifier, the energy of a pump beam is split up in the nonlinear crystal into a signal and an idler beam, where the signal wavelength is determined by a seed beam. As a result the seed is amplified by parametric interaction with the crystal. Energy conservation requires that for the angular frequencies ω_p, ω_s and ω_i of the pump, signal and idler respectively, the following relation holds (see Fig. 2.3):

$$\omega_s + \omega_i = \omega_p. \tag{2.20}$$

The setup of a noncollinear OPA is shown in Fig. 2.4.

Using the slowly varying envelope approximation and assuming high gain, and negligible dispersion and pump depletion, the signal intensity is given by [30]

$$I_s(z) \approx I_s(0)\frac{1}{4}e^{2gz} \tag{2.21}$$

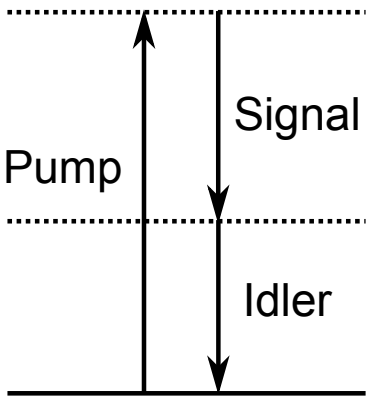

FIGURE 2.3: Energy conservation in an OPA. The dotted lines indicate virtual energy levels.

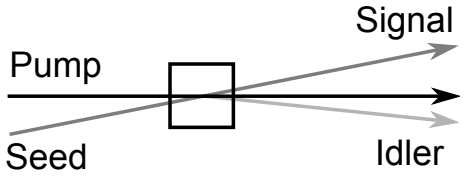

FIGURE 2.4: An OPA seeded with a narrow spectrum. For different seed wavelengths the idler has a different direction to fulfil momentum conservation.

where z is the distance traveled in the crystal, $I_s(0)$ is the seed intensity at the beginning of the crystal, and the parametric gain g is given by

$$g = \sqrt{CI_p(0) - \left(\frac{\Delta k}{2}\right)^2} \tag{2.22}$$

where C depends on the material and the wavelengths used, $I_p(0)$ is the undepleted pump intensity and Δk is the phase mismatch discussed in the next section. To optimize the output, these three parameters should be optimized. However, the pump intensity is limited by the damage threshold of the gain material and the onset of parametric fluorescence. For this reason the OPA system presented in this thesis consist of three nonlinear crystals to parametrically amplify in three separate stages, so that a high gain and output is achieved, with low levels of fluorescence.

2.3.2 Phasematching

Amplification by stimulated emission is automatically in phase over the whole laser crystal. However, if a nonlinear process such as parametric amplification is used, then the light generated in different positions in the crystal are not necessarily in phase, due to dispersion. So the refractive index experienced by the driving wavelength (the pump) and the generated wavelengths (signal and idler) can be different. To ensure constructive interference for the signal and idler beams to reach a high output, the phase velocity of the idler and signal combined should be equal to that of the pump wavelength, which is called phase matching. Phasematching can also be viewed as achieving the conditions under wich momentum is conserved. In optical parametric amplification, where beam 1 is split into beams 2 and 3,

$$\boldsymbol{k}_1 = \boldsymbol{k}_2 + \boldsymbol{k}_3 \tag{2.23}$$

should hold, where $\boldsymbol{k}_n$ is the wavevector of beam n. Any imbalance between the left and right side of this equation is called a phase mismatch, denoted by Δk.

The phase matching method employed in the optical parametric chirped pulse amplification setup is based on the fact that the pump and signal beams have a perpendicular polarization. Because the OPA crystals (BBO) are birefringent, the pump and idler experience a different refractive index. This can be tuned by varying the angle between the pump beam and the optical axis of the BBO crystals [17, 33] to achieve phase matching between the pump wavelength at 532 nm and the amplified signal wavelength of 800 nm.

2.3.3 Group velocity matching

Because of dispersion, the phasematching conditions are different for different wavelengths. This results in a difference in group velocities. By letting the seed and pump beam travel at a different angle, the system can be set up in such a way that projection of the group velocity of the idler on the direction of the signal beam is equal to the group velocity of the signal [34], see Fig. 2.5. This can be used for even more broadband amplification than what is generally possible with collinear optical parametric amplification.

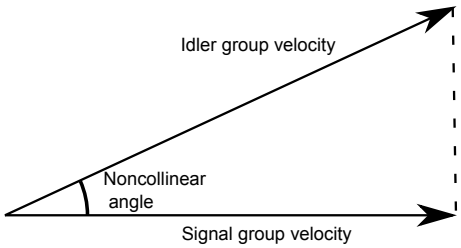

FIGURE 2.5: Group velocity matching for phasematching a broader bandwidth.

2.4 Cavity and amplifier design

2.4.1 ABCD matrices

To analyse optical systems where a beam travels along an optical axis with small angles θ such that $\sin\theta \approx \theta$, it is easy to use matrices of the form

$$\begin{pmatrix} x_2 \\ \theta_2 \end{pmatrix} = \begin{pmatrix} A & B \\ C & D \end{pmatrix} \begin{pmatrix} x_1 \\ \theta_1 \end{pmatrix}, \tag{2.24}$$

where 1 and 2 indicate input and output, and x is the distance from the beam to the optical axis. The same matrices are used in Gaussian optics, but a different interpretation of their meaning is used.

A lens with focal distance f has a describing matrix of

$$F = \begin{pmatrix} 1 & 0 \\ -\frac{1}{f} & 1 \end{pmatrix}, \tag{2.25}$$

while passing through a material with refractive index n and length d is described by

$$D = \begin{pmatrix} 1 & \frac{d}{n} \\ 0 & 1 \end{pmatrix}. \tag{2.26}$$

We can also see that any system can be modeled as two lenses a certain distance apart. The matrix resulting from traveling a distance d_1 through air ($n \approx 1$), a lens with focal length f_1 and then d_2 and f_2 is

$$F_2{*}D_2{*}F_1{*}D_1 = \begin{pmatrix} 1 - \frac{d_2}{f_1} & d_1 + d_2 - \frac{d_1 d_2}{f_1} \\ -\frac{1}{f_1} - \frac{1}{f_2} + \frac{d_2}{f_1 f_2} & 1 - \frac{d_1}{f_1} - \frac{d_2}{f_2} - \frac{d_1}{f_2} + \frac{d_1 d_2}{f_1 f_2} \end{pmatrix}, \tag{2.27}$$

so all four components of the matrix can be adjusted by changing the distances and the focal lengths of the lenses.

For optical systems consisting only of thin lenses and beam propagation this application of the transformation matrix formalism is sufficient to find the optical beam path. In the case of cavities, the modes inside can be found by the requirement that the beam should be at the same position and angle after a roundtrip. A third situation encountered in the research for this thesis is cylindrical rod amplifiers under radial thermal stress. In this case it is possible to use the description of a medium of length d with a refractive index dependent on the distance from the center r with $n = n_0 - \frac{1}{2} n_2 r^2$:

$$\begin{pmatrix} \cos(d\sqrt{\frac{n_2}{n_0}}) & \frac{1}{\sqrt{n_0 n_2}} \sin(d\sqrt{\frac{n_2}{n_0}}) \\ -\sqrt{n_0 n_2} \sin(d\sqrt{\frac{n_2}{n_0}}) & \cos(d\sqrt{\frac{n_2}{n_0}}) \end{pmatrix}. \tag{2.28}$$

but while d is known, and the resulting focal distance can be measured, this does not give enough information to model the whole system. If the A- and D-entries of the matrix are assumed to be small we can model the system as described in section 2.4.4.

2.4.2 Thermal lensing and birefringence

To estimate the focal lengths of the Nd:YAG amplifying rods depending on the repetition rate of the system (and therefore on the heat load), we measured the focal lengths at certain repetion rates and diode powers and extrapolated by using the power dependence of thermal lensing. Thermal lensing in a cylindrical rod geometry is caused by the stress- and temperature induced refractive index variation in the rod, and end-face bulging [13]. The lensing is not influenced by the length of the rod, but only by its diameter, and the pump power P that is absorbed in the rod. We can therefore write the focal length f as

$$f = \frac{M}{P}, \tag{2.29}$$

where M contains all material properties of the rod [13].

The thermal stress also causes a radial birefringence, which then results in a change of polarization for the laser beam going through the rod, depending on the position and initial polarization state. Because we use many polarizing optics and polarization-dependent nonlinear processes, this effect needs to be compensated. The compensation method is shown in section 2.4.4 and section 5.1.

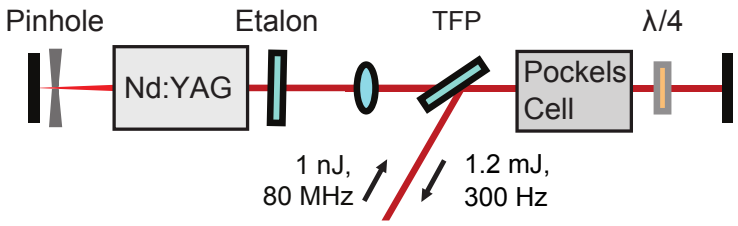

FIGURE 2.6: Schematic of a regenerative amplifier with our pulse energies and repetition rates shown as an example of its abilities. TFP, thin-film polarizer; $\lambda/4$, quarter wave plate. The end mirrors can be curved to change the beam profile and the stability of the cavity.

2.4.3 From nJ to mJ: regenerative amplifier design

As part of the pump laser we use a regenerative amplifier to amplify the nJ-level pulses from the Nd:YVO_4 oscillator to an energy of ~1mJ. A regenerative amplifier is a type of multipass amplifier where a pulse is coupled into a laser cavity and then completely coupled out by using a fast switch. Our setup is shown in Fig. 2.6. For the laser cavity we use a continuously diode-pumped Nd:YAG rod as a gain medium, and take its thermal lensing into account to choose the length of the setup and the curvature of the end mirrors. Our Pockels cell functions as a voltage-switched quarter waveplate. The thin-film polarizer (TFP) inside the cavity reflects depending on the polarization of the passing beam, so with the Pockels cell we have voltage-switched in- and outcoupling.

Any incoming pulse should be vertically polarized and reflects off the TFP into the cavity. By passing two times through the quarter waveplate, the pulse is then horizontally polarized and transmitted through the TFP. It then passes through the gain medium, and back through the TFP again. If the Pockels cell remains off, the polarization is again rotated and the beam is coupled out. If the Pockels cell is turned on while the pulse is on the left side, the Pockels cell compensates for the quarter wave plate, the polarization remains unchanged, and the pulse remains in the cavity as long as the Pockels cell is on.

The cavity should be long enough so the Pockels cell can switch after a pulse passed through it, but before it returns. The length also depends on the divergence and size of the beam through the amplifying medium. With a large parallel beam, the most energy can be extracted from a cylindrical rod, which leads to a higher ouput energy. The typical output power of the regenerative amplifier is 1.2 mJ after approximately

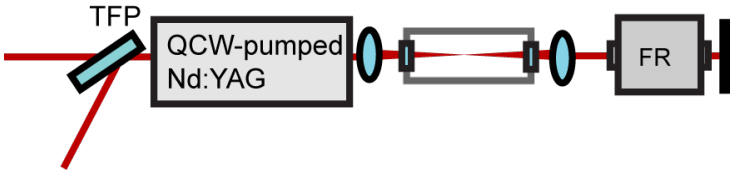

Figure 2.7: Single arm of the double-pass amplifiers. TFP, thin-film polarizer; FR, Faraday rotator.

60 roundtrips in the cavity. The Nd:YAG RD50 module from Cutting Edge Optronics (part of Northrop Grumman) is pumped at 18 A to reach this output.

2.4.4 Double-pass amplifier design

The Nd:YAG amplification system after the regenerative amplifier consists mainly of two arms where the beam passes through the diode pumped Nd:YAG rods twice, shown in Fig. 2.7.

The combination of the thin film polarizer and the Faraday rotator allows the beam to exit in a different direction than the way it entered. The rotator in combination with the imaging system also compensates for thermal birefringence by exchanging the horizontal and vertical polarizations before passing the beam through the amplifier rod. This is based on the effect that the Faraday rotator rotates the polarization by 45 degrees, independent of the input polarisation and beam propagation direction. As a result the polarization components are exchanged after passing through the rotator twice. This in turn means that both polarization components will see the same total phase shift, restoring the original linear polarization.

The relay-imaging system consisting of two lenses projects the beam on the folding mirror, and a vacuum tube is required around the focus when the intensities are high enough to cause electrical breakdown in air. The image position of the top hat should be inside the rod and should be optimized together with the folding mirror for the best thermal birefringence compensation. We used a non-magnifying imaging system, which assumes the A- and D-parameters in matrix 2.28 are close to unity.

To extract as much energy from the rods as possible and to reduce the peak intensity for a given pulse energy, we want the beam to fill the amplifying rods with a flat intensity distribution. This requires a large aperture to shape the beam, and lenses to expand, collimate, and

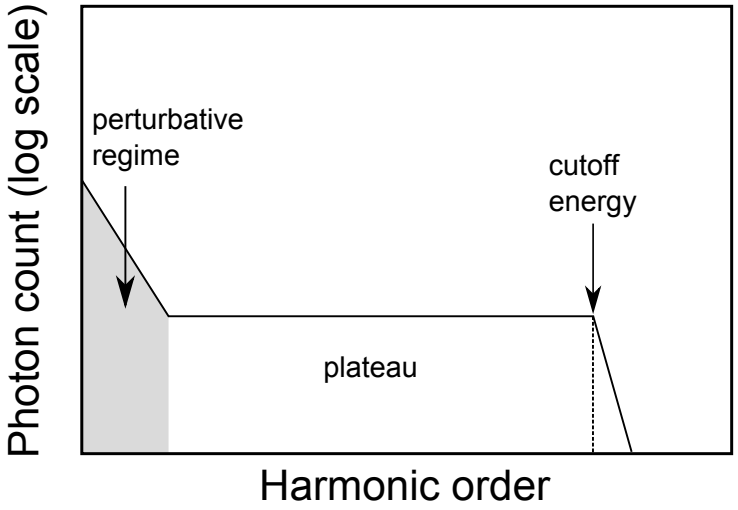

Figure 2.8: Schematic of the efficiency of high-harmonic generation at different harmonic orders.

image the beam through the whole setup. Using the first rod itself as an aperture caused diffraction effects which would form a hot spot in the beam. Therefore a separate aperture was used well before the amplifier unit, and relay imaged to the entrance surface to minimize the diffraction effects. Further details of the system can be found in Chapter 5.

2.5 High-harmonic generation

In harmonic generation at lower orders, a perturbative approach is still sufficient to calculate the efficiencies for the produced energies. In this regime, the conversion efficiency is reduced with harmonic order. However, at the higher orders required to reach the water window [35] this approach is insufficient to explain the results. At high electric fields, the conversion reaches a plateau, and then diminishes again after a cutoff energy [36], which is shown in Fig. 2.8.

2.5.1 Three-step model

According to the three-step model, shown in Fig. 2.9, in this non-perturbative regime called high-harmonic generation, a strong electric field ionizes an atom, after which the released electron gains energy in the electric field and is recombined with the parent ion. This model cap-

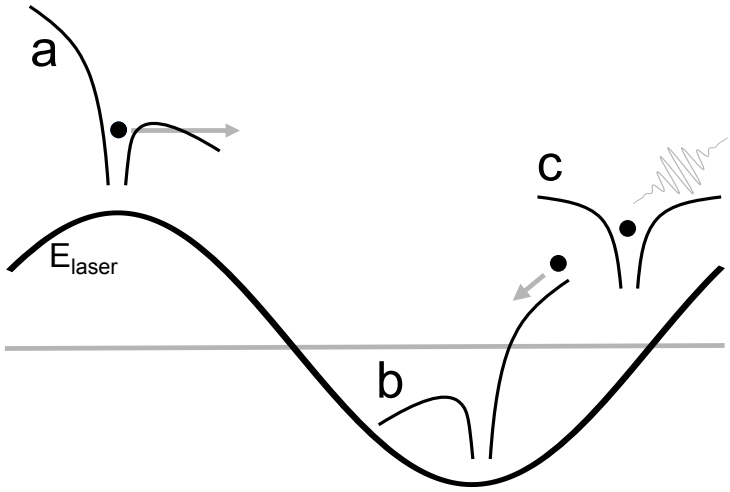

Figure 2.9: The three-step model. (a) An atomic potential is deformed by the high electric field of an incoming pulse. This allows a bound electron to tunnel out, which ionizes the atom. (b) The electron accelerates in the electric field of the laser. (c) The electron recombines with its parent ion and emits radiation.

tures some of the important aspects of high-harmonic generation. First, the electric field must be strong enough to deform the atomic potential. This allows the electron to tunnel out.

The frequencies of the generated radiation after recombination can then be classically [37] or quantum-mechanically [38] calculated. For these calculations it is assumed that the electron is stationary relative to the atom after ionization. The model also shows how the cutoff energy scales with the wavelength λ and intensity I of the generating source beam and the ionization potential E_i of the atoms used in the process [12]. An approximation of these results for the cutoff energy E_c is given by

$$E_c = E_i + 3.2U_p \tag{2.30}$$

where U_p is the ponderomotive potential, and $U_p \propto I\lambda^2$. From this it looks like the highest photon energies can be reached by choosing a gas with a high ionization potential such as noble gasses like argon and using high intensities at long wavelengths. However, it is important to note that this is only the result for a single atom, without phasematching considerations. It also does not take into account the influence of the wavelength and intensity on the total efficiency.

With longer seed wavelengths it takes a longer time for the ionized electron to recombine. This lets the electron gain more energy, but it also spreads out the electron wavepacket more, so its recombination probability is lower [39]. This results in a lower efficiency at longer wavelength for a single atom. However, it is impossible to do phasematched high-harmonic generation in noble gasses from 800 nm into the water window, while it is possible to span the water window when driving the HHG process with 2 micrometer or longer wavelengths [40]. In this case phasematching has to be done at high gas pressures, which also increases efficiency, and these combined effects can overcome the reduced single-atom response compared to using shorter wavelengths [41].

Another result from the semi-classical calculations is that the efficiency of high-harmonic generation depends strongly on the ellipticity of the fundamental (driving) laser, because an electron in an elliptically polarized beam will have a lower chance of recombining with its parent ion.

2.5.2 Phasematching of high-harmonic generation

Even though it deals with the same underlying physics, phasematching in high-harmonic generation is handled very differently from low-order parametric processes. High-harmonic generation is usually done in gasses [42], which are isotropic by nature. This symmetry means that only odd-harmonics of the fundamental beam are possible, and it removes the possibility to use polarization for phase velocity control. The three important factors for phasematching high-harmonic generation are the refractive index of the neutral gas, the ionization dependent refractive index and the geometrical phase factor. In low-order processes usually parallel beams are used so the geometry can be neglected, and there should be no ionization because of the far lower peak powers.

The geometrical phase factor present in a focused beam is called the Gouy phase, and is a gradual π phase shift over a focus which changes faster in a tighter focus. When high harmonics are generated with a focused beam in a gas cell, a balance needs to be struck between a high intensity for greater single atom efficiency and the difficulty of compensating for a fast Gouy phase shift in a tight focus [43]. This can be resolved by using differential pumping, where a small hole at the end of the gas cell lets the beam through and the gas pressure drops rapidly behind the gas cell. When a beam is focused at the end of this gas cell, the fast Gouy fase shift occurs after the pressure drop and no more

harmonics are generated that could destructively interfere with the already generated harmonics. Another way to produce a rapidly changing gas pressure in the direction of the seed beam is to use a gas jet. It is also possible to mix gases, or tune the phase matching by varying the gas pressure. In our experiments described in Chapter 6 we used the method of focusing the fundamental beam in a gas cell just in front of a small hole. After that hole differential pumping was applied to avoid cancellation and reabsorption of the generated harmonics (near 50 nm).

Chapter 3

Lensless phase contrast microscopy based on multi-wavelength Fresnel diffraction

Abstract

We demonstrate a compact, wide-field, quantitative phase contrast microscope that does not require lenses for image formation. High-resolution images are retrieved from Fresnel diffraction patterns recorded at multiple wavelengths, combined with a robust iterative phase retrieval algorithm. Quantitative phase contrast images of living cultured neurons are obtained with a transverse resolution of < 2 μm. Our system is well suited for high-resolution live cell imaging and provides a compact, cost-effective alternative to full-sized phase-contrast microscopes.

Ever since its invention, microscopy has been an essential technology in life science research. Microscope development has seen tremendous improvements, resulting in advanced approaches such as multiphoton microscopy [45] and super-resolution imaging [46, 47]. In many cases, there is a need to record images of living cells with a compact and/or cost-effective device. Such a situation occurs for instance in cases where space or environmental constraints make the use of a full-size microscope challenging. Furthermore, compact, robust and therefore easily transportable devices may provide a solution for clinical diagnostics in remote areas, or to reduce health care costs by providing low-cost imaging tools

This chapter is adapted from: D. W. E. Noom, K. S. E. Eikema, and S. Witte, "Lensless phase contrast microscopy based on multiwavelength Fresnel diffraction," *Optics letters*, vol. 39, pp. 193–6, jan 2014

for point-of-care diagnostics. Since the main factor that determines both cost and size of a microscope is usually the imaging optics, a significant step towards a compact device can be expected if the imaging can be performed without lenses. In practice, this means that the effects of wave propagation and diffraction need to be overcome in a different way. A variety of solutions to this challenge have been reported. These include minimization of the sample-camera distance by growing cells directly on a complementary metal-oxide-semiconductor (CMOS) sensor [48], in-line holographic methods [49, 50], and numerical reconstruction of an image from a coherent diffraction pattern [24, 51].

Here we demonstrate a compact, high-resolution lensless microscope, which can image complex (i.e. modulating both phase and amplitude of the incident field), extended objects without requiring any a-priori knowledge of the sample itself. The microscope does not contain any moving parts, and only uses commercially available diode lasers and a CCD sensor. To obtain an image, we record Fresnel diffraction patterns of the sample at multiple wavelengths, and use these patterns as input in an iterative phase-retrieval algorithm. After retrieving the phase of the diffraction patterns, numerical back-propagation results in a near-diffraction-limited image of the illuminated object. This approach provides quantitative phase contrast images of the sample, making it ideally suited for live cell imaging studies.

In the near-field regime, the propagation of an electromagnetic field distribution over a distance z can be described by the Fresnel diffraction integral:

$$E(x,y,z) = \frac{e^{i2\pi z/\lambda}}{i\lambda z} \iint E(x,y,0) e^{\frac{i\pi}{\lambda z}[(x-x')^2+(y-y')^2]} dx'dy' \qquad (3.1)$$

To enable back-propagation of a recorded diffraction pattern to the object plane, the phase associated with this diffraction pattern needs to be retrieved through numerical means. Both in-line holographic reconstruction and Gerchberg-Saxton-based iterative algorithms have been applied to this end, although these methods are usually limited in their abilities by the fact that only a single diffraction pattern is recorded. Iterative phase retrieval algorithms rely on propagation to couple amplitude and phase, and therefore require some knowledge at an additional position besides the measurement plane. This introduces the need for support constraints in the object plane [51, 52]. Such constraints can be circumvented if multiple measurements are taken under different propagation conditions, e.g. by recording diffraction patterns at multiple distances

from an object [53–55]. However, this approach requires either sample or camera movement, making it slow and sensitive to transverse displacements. Ptychography is an approach that uses multiple images at that are transversely displaced from each other to introduce redundancy and enable robust phase retrieval [11, 56, 57], although a large set of diffraction patterns needs to be recorded. Alternatively, we show that diffraction patterns at a single position but with multiple wavelengths can also be used as input for iterative phase retrieval. A major advantage of this 'wavelength diversity' approach is that no moving parts are needed, while still allowing robust phase retrieval even with complex, extended samples. Wavelength-dependent diffraction of incoherent light has recently also been exploited in wide-field and fluorescence microscopes for imaging of several axial planes simultaneously [58]. We have recently implemented this approach to facilitate imaging at extreme-ultraviolet wavelengths, using spectrally resolved input images from a Fourier-transform-based two-pulse lensless imaging scheme [59]. When using visible light, it allows microscopy with a highly compact and simple setup, and allows for fast image acquisition.

To retrieve an image of an object, we record a diffraction pattern of that object at either two or three different wavelengths. These diffraction patterns are used as input in an iterative phase retrieval algorithm, in which we start with a single diffraction pattern at wavelength λ_1 with a random phase, and 'propagate' this field numerically to the second wavelength λ_2. After propagation, we retain the phase but replace the amplitude by the actually measured amplitude at λ_2, and propagate back to λ_1 (or onwards to a third wavelength). To propagate the diffraction pattern from λ_1 to λ_2, we first propagate to the object plane by Fourier transformation, multiplication with the free space propagation transfer function [22]:

$$H(f_x, f_y, \lambda_1) = e^{i2\pi z\sqrt{\frac{1}{\lambda_1^2} - f_x^2 - f_y^2}}, \tag{3.2}$$

and inverse Fourier transformation. In Eq. (3.2), f_x and f_y are the spatial frequencies along the $x-$ and y-axis, respectively. At the object plane, we divide the phase pattern by the wavelength ratio λ_2/λ_1 to account for the difference in phase shift that the object introduces for different wavelengths, and subsequently propagate back from the object plane using the conjugate propagation transfer function $H^*(f_x, f_y, \lambda_2)$. This calculation is more general than the Fresnel propagation Eq. (6.1), as it is not restricted to small angles. The algorithm typically requires

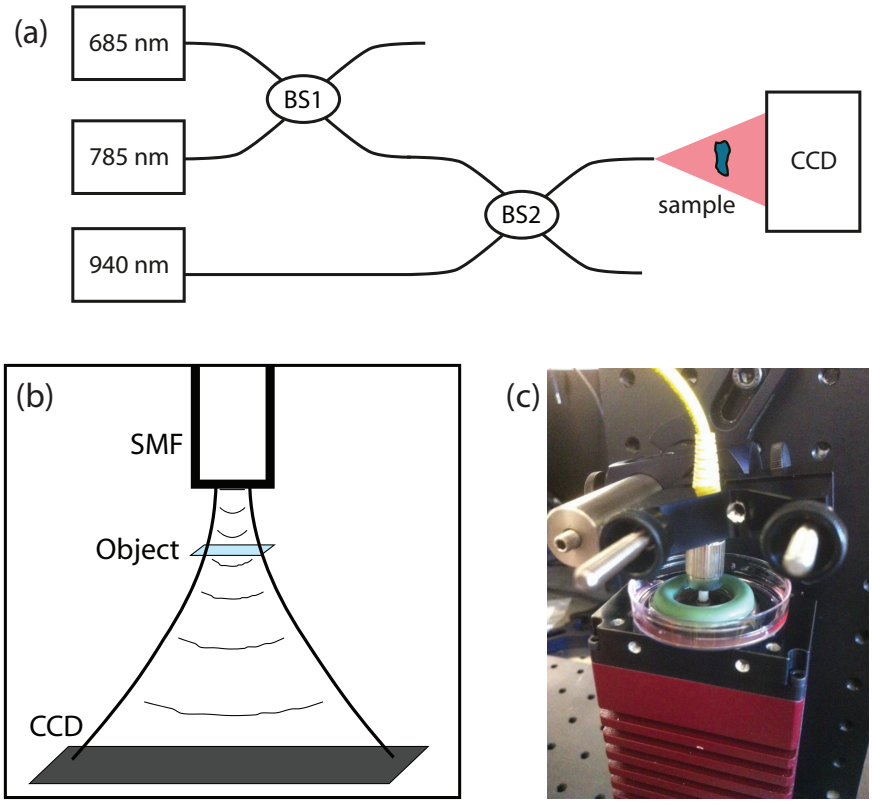

FIGURE 3.1: (a) Schematic of the all-fiber-based lensless imaging setup. Three fiber-coupled laser diodes are combined into a single fiber using 2×2 fiber beamsplitters (BS1 and BS2). The fiber output beam propagates towards a sample, and a CCD camera records the diffraction pattern for each wavelength by turning the lasers on and off sequentially. (b) Schematic of the Fresnel diffraction geometry used in the microscope. The diverging beam from the single-mode fiber (SMF) is transmitted through an object onto a CCD. The beam divergence introduces a magnification factor in the microscope. (c) Picture of the imaging setup, showing the fiber output, the CCD camera, and the dish containing a coverslip with cells.

10-40 iterations over all wavelengths to converge to a final solution for the phase. The retrieved field is then propagated back to the object plane to recover the exit surface wave, which is the product of the illumination function and the complex object transmission function. As the illumination is a smooth Gaussian profile, a clear image of the object is readily obtained. Both the amplitude and phase are retrieved, providing a bright-field and a quantitative phase contrast image simultaneously.

A schematic of the lensless microscope is shown in Fig. 3.1(a). We use three diode lasers at wavelengths of 685 nm, 785 nm and 940 nm, butt-coupled to single-mode fibers. The laser outputs are combined by broadband 2×2 fiber-beamsplitters, resulting in an alignment-free light source where all three wavelengths are emitted by a single-mode fiber, ensuring perfect spatial overlap and spatial coherence. The light emanating from the fiber output is directly sent onto the sample, and a CCD camera (AVT Prosilica GC1920, 14 bits, 1936×1456 pixels, 4.54 μm pixel size) records the resulting diffraction patterns. We acquire diffraction patterns at each of the three wavelengths consecutively by sequentially switching the lasers on and off.

As a first test we perform imaging of a USAF 1951 test target in transmission. The fiber output is placed at a distance of 1.2 mm in front of the object, and the CCD is placed at 9 mm behind the object. This results in a numerical aperture of 0.36 for detection of the diffracted light (determined by the size of the CCD sensor), which would allow a diffraction-limited resolution of 1.2 μm. The field-of-view (FOV) as determined from the CCD size and number of pixels is then 1.1×0.87 mm, although in practice the illuminated area is the limiting factor due to the required magnification factor (see below), which restricts the FOV to a slightly smaller area.

Fresnel diffraction patterns are recorded at the three different wavelengths with an exposure time of 0.8 ms per image. Near-infrared wavelengths are used to minimize absorption and scattering by biological samples, while still having sufficient photon energy record the diffraction patterns with a Si-based CCD detector. Also, the dispersion of water and biological material is low in the near-infrared, so that it does not affect the phase retrieval. If this is not the case (e.g. when using visible wavelengths), the refractive index change can be explicitly incorporated into the phase retrieval algorithm through e.g. known Sellmeier equations of water and/or bulk protein.

In the Fresnel diffraction regime, the pixel size of the CCD camera may be a limiting factor for the resolution, as this limits the resolution

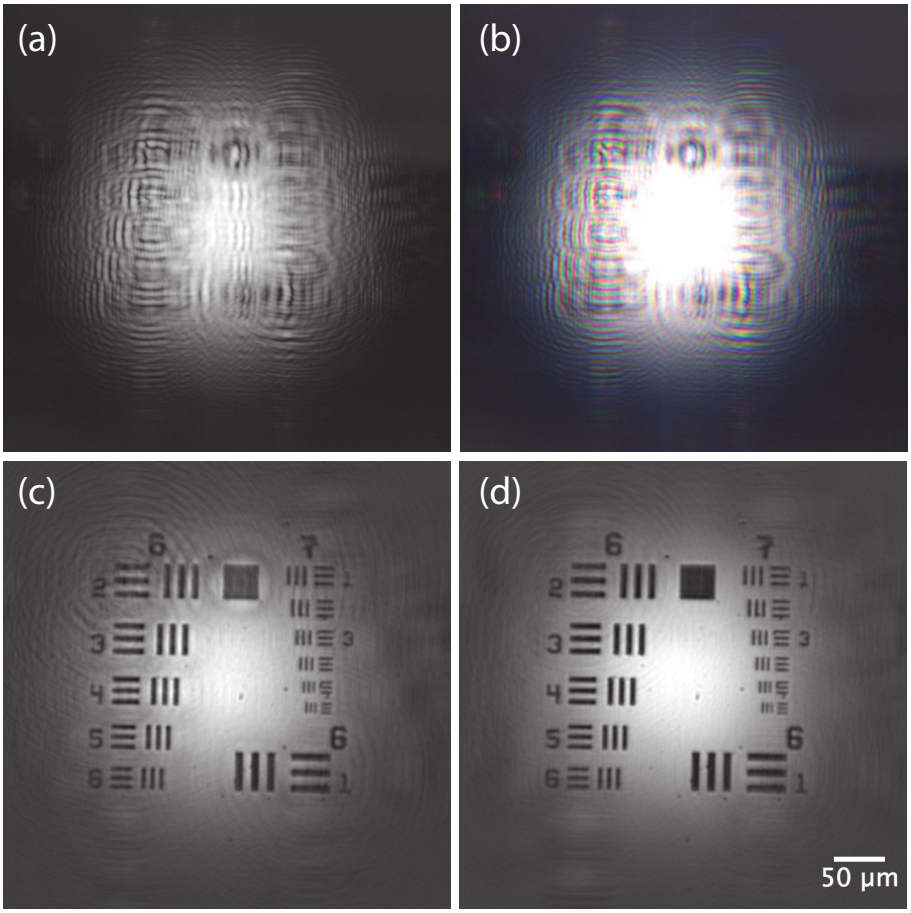

FIGURE 3.2: (a) Diffraction pattern of a USAF1951 resolution test target at 785 nm wavelength (logarithmic intensity scale). (b) Overlay of three diffraction patterns of the same object (log scale), recorded at 685 nm (blue), 785 nm (green) and 940 nm (red). (c) Retrieved image after 30 iterations of the multi-wavelength phase retrieval algorithm and backpropagation to the object plane. Two diffraction patterns at 685 nm and 785 nm are used as input. (d) Retrieved image after a the same phase retrieval procedure, using three diffraction patterns (wavelengths 685, 785 and 940 nm) as input.

at which the diffraction pattern is sampled and therefore reconstructed. To remove this limitation, we introduce a magnification by illuminating the sample with a strongly diverging wave, which is readily obtained by using the output beam of a single-mode optical fiber, as shown in Fig. 3.1(b). The magnification of the recorded diffraction pattern can be controlled by adjusting the distance between the fiber output and the sample, while keeping the sample-camera distance fixed. In this geometry, the effective pixel size at the image plane is given by the CCD pixel size divided by the magnification. In the geometry used to image the USAF target the magnification is 7.5, and the resulting pixel size at the object plane is 0.6 μm. Advantages of this approach compared to other pixel-super-resolution methods [48, 50] are that light source movement is not needed, and only three diffraction patterns are required to produce a high resolution image.

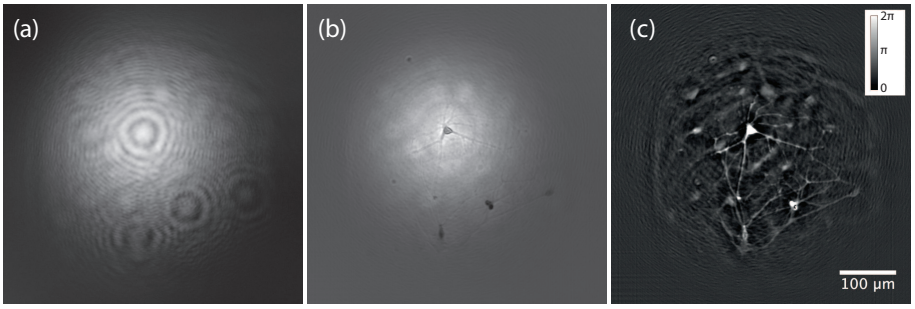

Figure 3.3: (a) Diffraction pattern (logarithmic intensity scale) of a sample of live neurons grown on astrocytes, recorded at 940 nm wavelength. (b) Reconstructed intensity image at the object plane, using diffraction patterns at three wavelengths. (c) Reconstructed phase image of the sample, clearly showing the neurons. The scale bar shows the measured phase shift in radians.

Figure 3.2(a) shows a diffraction pattern of the USAF1951 test target at a wavelength of 785 nm. Similar diffraction patterns are recorded at the other two wavelengths. To highlight the wavelength dependence of the Fresnel diffraction, an overlay of the diffraction patterns at the three different wavelength is displayed in Fig. 3.2(b). These images form the basis for the multi-wavelength phase retrieval algorithm. In principle, only two diffraction patterns are required for the algorithm to work. That this is indeed the case is shown in Fig. 3.2(c), where a clear image of the test target is obtained, although some residual interferences can be seen in the reconstruction. The use of more than two wave-

lengths improves the reconstruction further, as noise is averaged over more measurements and small artefacts due to camera read noise are at different image positions for different wavelengths. This is highlighted by Fig. 3.2(d), displaying a reconstruction using diffraction patterns at all three wavelengths, in which the imperfections that remained in the two-wavelength case are fully removed. By analyzing Fig. 3.2(d), we find that a transverse resolution of 1.8 μm is achieved, which is 1.5$\times$ the diffraction limit and 2.5$\times$ smaller than the camera pixel size. The algorithm converged within 30 iterations, which takes about 1 minute of processing time on a standard desktop computer when using 1936$\times$1456 pixel images. However, the required calculations are well suited for parallel processing: a first implementation of the algorithm on a graphical processing unit achieved around 100 iterations per second, indicating that an update rate of several Hz is achievable with a fully integrated data acquisition and processing system.

To demonstrate the capabilities of our multi-wavelength lensless microscope for live cell imaging, we perform imaging experiments on mouse hippocampal neurons, which have been cultured on top of a layer of rat astrocytes on a coverslip. A typical diffraction pattern at 940 nm wavelength is shown in Fig. 3.3(a). Both an intensity and a phase image are obtained after 30 iterations of the algorithm, which are shown in Figs. 3.3(b) and 3.3(c), respectively. Cells can be considered to be phase objects due to their transparency, which makes phase contrast microscopy essential for obtaining high-contrast images. This is illustrated by a comparison between the intensity image in Fig. 3.3(b), in which a few cell bodies and dendrites can be identified, and the phase image in Fig. 3.3(c), which clearly shows many fine details of the cells and their network of dendrites. In addition, the phase image also provides a clear view of the astrocytes on which the neurons are cultured. The ability to retrieve a quantitative phase map enables a measurement of the optical path length through the cells, from which additional information on the height profile of the cells can be obtained [30, 60].

In summary, we have developed a lensless quantitative phase contrast microscope, which exploits diffraction patterns recorded at multiple wavelengths to enable robust image reconstruction without the need for moving parts. Quantitative phase images with < 2 μm transverse resolution are obtained using an iterative phase retrieval algorithm, requiring diffraction patterns at only three different wavelengths as input. The setup consists of a fully fiber-integrated light source and a CCD camera, and allows a tunable magnification factor through the use of a diver-

gent illumination geometry. We have verified the potential of our setup for live cell imaging applications by recording high-resolution phase contrast images of living cultured neurons in solution. Further advances are expected through the implementation of a camera with a smaller pixel size, which relaxes the magnification requirements for achieving μm resolution, and allows a higher FOV at a given resolution. Our system has favourable properties in terms of compactness and cost-effectiveness compared to lens-based microscopes with similar capabilities. We therefore anticipate that our system may become a useful alternative in applications where quantitative phase imaging is important, such as cell biology or surface profiling.

Chapter 4

High-speed multi-wavelength Fresnel diffraction imaging

Abstract

We demonstrate a compact lensless microscope which can capture video-rate phase contrast images of moving objects and allows numerical scanning of the focal distance after recording. Using only an RGB-detector and illumination from a single mode fiber, diffraction patterns at three wavelengths are recorded simultaneously, enabling high-speed data collection and reconstruction of phase and amplitude. The technique is used for imaging of a moving test target, beads in a flow cell, and imaging of *Caenorhabditis elegans* moving in a droplet of liquid.

4.1 Introduction

Compact microscopes consisting of few parts are very desirable for many applications. One can think of microscopy in difficult to reach places or harsh environments, or applications where one would like to employ many microscopes in parallel. It is therefore important to get the most information out of the most basic imaging setups [48, 50, 61–63]. We describe a system for fast lensless phase-contrast microscopy that requires only a three-wavelength source, an RGB-detector and a computer, but

This chapter is adapted from: D. W. E. Noom, D. E. Boonzajer Flaes, E. Labordus, K. S. E. Eikema, and S. Witte, "High-speed multi-wavelength Fresnel diffraction imaging," *Optics Express*, vol. 22, p. 30504, dec 2014

is still able to reconstruct the complex refractive index of a sample using images taken in a single shot.

We have already shown that it is possible to use diffraction patterns at three different wavelengths to retrieve phase and amplitude information from a sample with very little constraints on the imaging setup [44]. That method required multiple images to be taken of a sample while it was illuminated with different wavelengths transmitted through the same optical fibre. Here we show that the method can be used to take single shot images by using an RGB-detector and light sources at suitable wavelengths, thus enabling the imaging of moving objects. Three diffraction patterns are measured at the same time and a few iterations of a phase retrieval algorithm reconstruct the phase and amplitude of the sample.

4.2 Fresnel Diffractive Imaging

An RGB image detector only measures the intensity at different pixels, but for reconstruction of an image, the phase is also needed. Retrieval of the phase of the electric field is possible using holographic methods [10], intensity changes in different planes [64], or iterative retrieval algorithms [23]. The change in intensity when the light field propagates, or when the illuminating wavelength changes, depends on the complex phase curvature of the wavefront. This information can be extracted from multiple diffraction patterns using a phase reconstruction algorithm. One way to do this is by recording propagation effects of the diffraction pattern from an object by taking multiple images at different distances [53, 65]. However, in Fresnel diffraction, the distance from the sample to the detector and the wavelength of the illuminating source play a similar role [18, 66]. By measuring diffraction patterns at different *wavelengths* we can measure how the intensity propagates without changing the position of the detector. The requirement for this to work is that the sample has only a limited wavelength dependence of both the refractive index and absorption.

While there are many other algorithms used for phase reconstruction, our multi-wavelength approach requires no additional information and converges robustly for many different samples. The sample does not need to be isolated from its surroundings and in this paper we show it can even be a complex target moving in a fluid. The only information required for a reconstruction, except for the images, is the approximate wavelengths

of the light used to illuminate the sample. After reconstruction the images can be refocused to any plane because of the quantitative phase information.

4.3 Setup

To reconstruct an image, we need diffraction patterns at three different wavelengths. With a monochrome image sensor this requires three detected frames, but using an RGB image sensor and suitable laser wavelengths this can be done in a single shot. To get an RGB-source we used fiber-coupled diode lasers at wavelengths of 402 nm, 519 nm and 636 nm, and employed fiber-coupled 50/50 beamsplitters as a simple way of beam combining. While this approach introduced losses, the laser intensities are still high enough to allow fast imaging. The combined beams are coupled into a final single mode fiber, which could be directed at a sample. We put our RGB image sensor, an IDS UI-5582LE-C CMOS camera with 2560x1920 pixels of size 2.2 μm and a color depth of 12 bits, after the sample to record diffraction patterns in transmission. A schematic of the setup is shown in Fig. 4.1. Only 3 microwatt of power per wavelength illuminates the sample, which requires an exposure time of 1 ms to achieve image saturation when the image sensor is placed 5 mm from the fiber. To obtain the phase of the electric field from an RGB image, we split the image into its three channels. With the three separate images we then apply the same reconstruction procedure as in [44].

CMOS sensors require extra care when triggered operation is required. Our chip has a "rolling shutter", where bottom pixel rows stop readout later than top rows. The readout of each horizontal row of pixels can be started simultaneously by using a "global start" option. This means the bottom rows will have a shorter exposure time than the top rows, making it harder to optimize exposure for a good dynamic range and a maximum signal to noise ratio. Furthermore, to reduce motion-induced blurring we want to have the shortest exposure time possible. To meet this demand, and to get an even exposure over the whole chip we pulse the lasers for a much shorter time than the shortest gate time of the CMOS chip. The framerate of the measurements is limited by the readout rate of the camera, and the exposure time for a single frame is limited by the amount of light needed for a good image (typically requiring a laser pulse length of 1 ms).

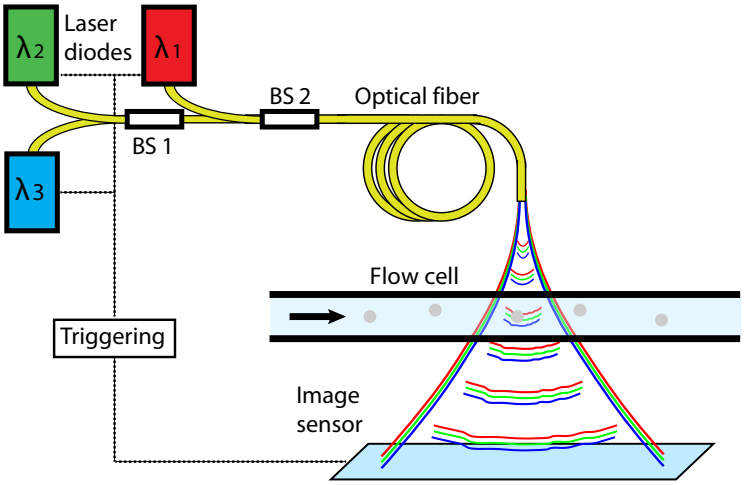

FIGURE 4.1: The imaging setup, where a flow cell with beads is taken as an example sample. The wavelengths λ_1, λ_2, λ_3 are obtained from laser diodes at 636 nm, 519 nm and 402 nm, respectively, coupled in a single-mode fiber. BS: fiber beamsplitter/combiner.

The algorithm is implemented in Python on a graphics processing unit (GPU) using pyCUDA. A single iteration of the algorithm for an image of 1 megapixel takes about 35 ms on a Geforce GTX780 GPU. Processing the images with two RGB iterations - which suffices for raw alignment - takes 82 ms, including overhead for transferring images from the host to the GPU memory. In theory this enables reconstruction at 12 Hz. The speed could be further optimized by writing the source in a programming language like C++, or by using a faster graphics card.

4.4 Moving USAF Test Target and beads in a flow cell

In our first experiment we show images of a fast moving target with high resolution. We mounted a USAF test target on a piezo stage and let it move with a sinusiodal pattern at 0.5 Hz with an amplitude of 100 μm. To achieve a high resolution we put the fiber tip close to the sample so it would be illuminated with a curved wavefront and project an enlarged diffraction pattern on the camera. In Fig. 4.2 we show two frames from

the video which was captured at 18.5 Hz. From these images it is clear the movent does not blur the sample significantly, and high resolution images can be rendered at video rate with a lensless setup.

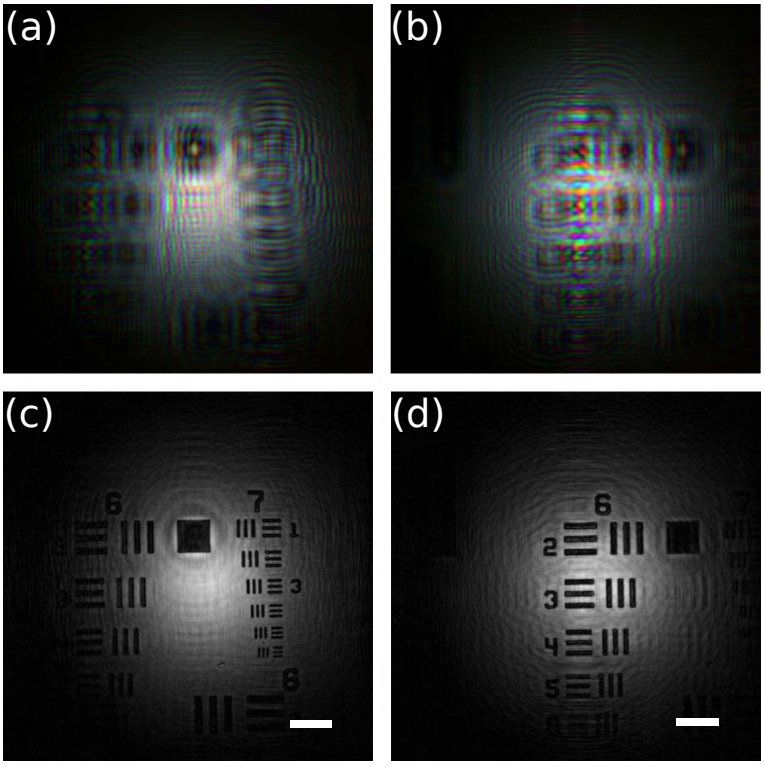

Figure 4.2: High speed refocusable lensless imaging of a moving USAF test target. (a), (b) Single shot images at different times. (c), (d) Reconstructed image at different times. In (c), the smallest features of group seven, 2.19 μm wide, are cleary visible. The scale bars are 50 μm wide.

The refocusing ability on moving particles is demonstrated by using beads passing through a flow cell. The height of this flow cell is 1 mm, which exceeds the depth of field of a single refocused image by more than an order of magnitude. In Fig. 4.3(a), five different time frames are shown at a single focal distance. Then in Fig. 4.3(b), we show five different focal distances at a single time frame. This shows that our presented method enables a full 2D scan over focal distance and time.

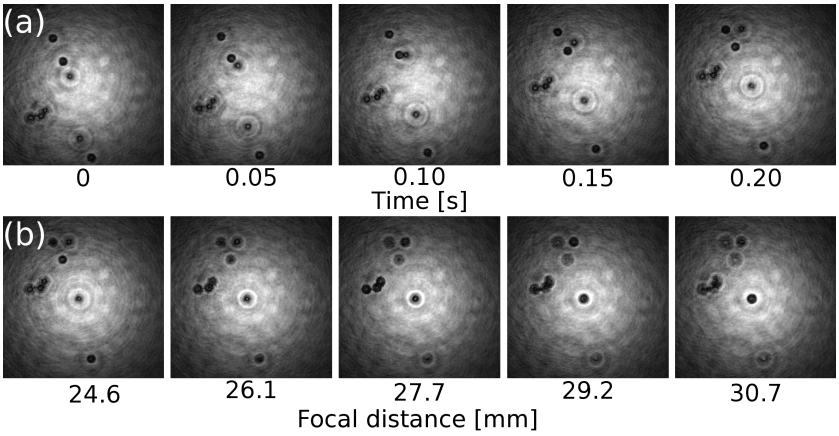

FIGURE 4.3: Beads with a diameter of 20 μm in a flow cell. (a) Images at different times at a single focal distance. (b) Images at different focal distances at a single point in time. The indicated focal distances are the numbers that have been used in the phase retrieval algorithm, which correspond to the geometric distance between object and camera scaled by a factor $(1 + d/R)$ because of the finite wavefront curvature (see Discussion section for details).

4.5 Refocusable Imaging of *C. elegans*

To demonstrate our method in a more complex environment, and make use of the refocusing capabilities, we used a sample of *C. elegans* swimming in a solution, shown in Fig. 4.4. The single-shot measurement is shown in Fig. 4.4(a), where the sample is illuminated with three lasers at the same time. In Fig. 4.4(b), a reconstruction using data obtained with the three wavelengths is shown. In this image, several reconstruction artifacts are visible. Figure 4.4(c) shows a reconstruction from the same data set, but now using only the red and green wavelength channels. This two-wavelength reconstruction leads to a better image compared to the three-wavelength result. This indicates that the assumption of a small wavelength dependence of the complex refractive index is invalid for this sample. Figure 4.4(d) shows the reconstructed phase image for the two-wavelength reconstruction. In Figs. 4.4(c) and 4.4(d) it can be seen that not all worms are in focus, and Figs. 4.4(e) and 4.4(f) show an amplitude and phase reconstruction at a different focal plane. The obtained phase reconstructions provide quantitative information of the optical thickness of the sample, which is made especially clear by the

worm at the top of the image which is folded back onto itself. With this object, a whole refocusable movie has been captured.

4.6 Discussion

As shown in the previous sections, diffraction imaging using just a single mode fiber as light source and an RGB chip for detection works very well. However, there are a few aspects that need closer inspection. One issue is that the technique requires coherent sources, which also means that diffraction patterns are visible from elements in the image that are not in focus. As a result, anything out of the focus plane will lead to clearly visible spurious diffraction rings in the reconstructed image.

Another potential issue is related to the use of an RGB-detector: pixels of different color are positioned next to each other, and therefore detect slightly shifted diffraction patterns on the scale of a pixel size. Furthermore, the different colored pixels have a significant detection efficiency for more than one source wavelength. However, we have seen no problems with reconstructions up to the smallest structures of our USAF test-sample, which have a width of 2.19 μm. When the detected images at different RGB-channels differ significantly because of effects other than propagation, like a color-dependent absorption and refractive index, it is possible the phase reconstruction fails. In this case, two out of three colors can be used to limit these effects.

Since our microscope geometry involves a curved wavefront for illumination, this curvature should be taken into account in the reconstruction algorithm. An interesting property that we find for the propagated diffraction patterns, is that a given diffraction pattern can either result from an object illuminated with a curved wavefront, or from a scaled version of the object located at a different distance. We looked into this aspect by using ray matrices [67], which have this form:

$$\begin{pmatrix} x_2 \\ x_2' \end{pmatrix} = \begin{pmatrix} A & B \\ C & D \end{pmatrix} \begin{pmatrix} x_1 \\ x_1' \end{pmatrix}, \tag{4.1}$$

where x_1 and x_1' are the input rays' position and slope, respectively, and the outputs of an optical system are given by x_2 and x_2'. If we use a wavefront with radius of curvature R and propagate by a distance d, we get the following matrix equation:

$$\begin{pmatrix} 1 & d \\ 0 & 1 \end{pmatrix} \begin{pmatrix} 1 & 0 \\ \frac{1}{R} & 1 \end{pmatrix} = \begin{pmatrix} 1 + \frac{d}{R} & d \\ \frac{1}{R} & 1 \end{pmatrix}. \tag{4.2}$$

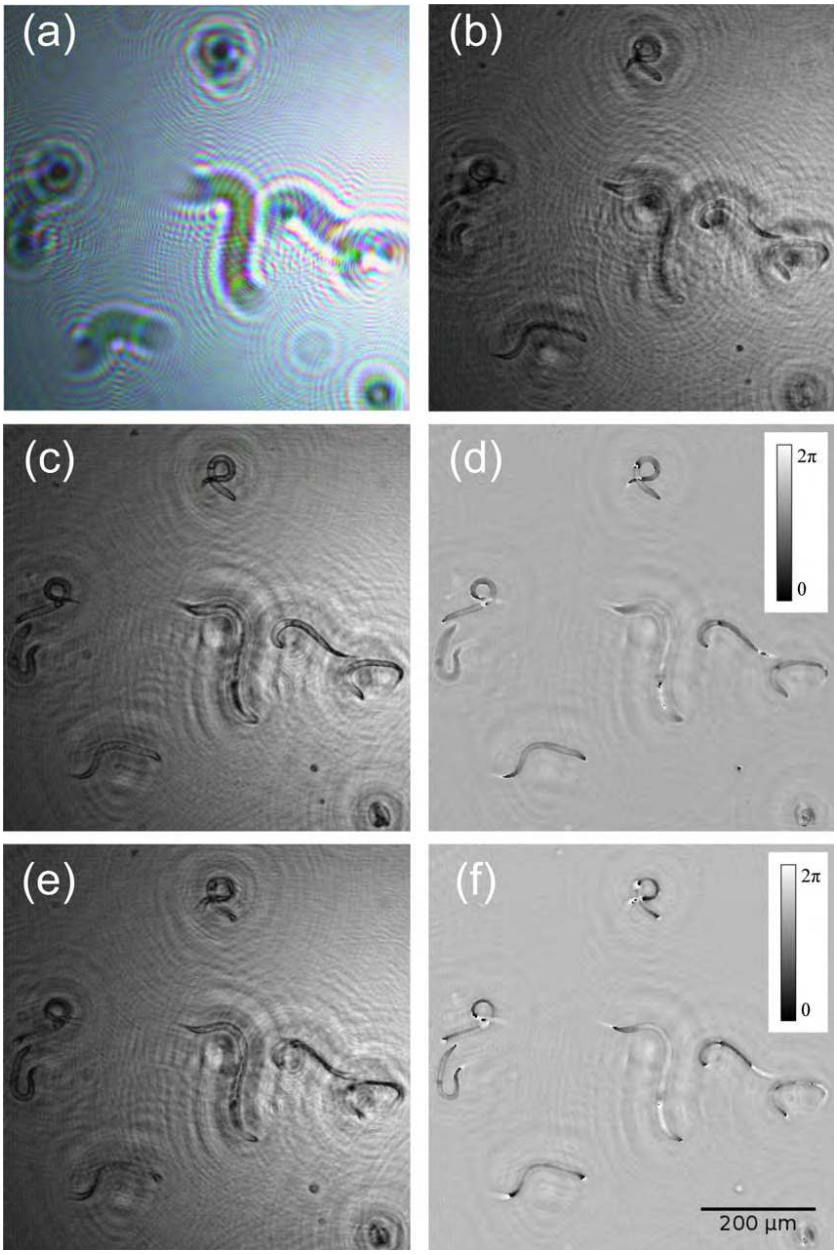

FIGURE 4.4: (a) Single shot diffraction pattern of C. Elegans. (b) Reconstructed intensity image using data at three wavelengths as input for the reconstruction algorithm. (c) Reconstructed intensity image using only the red and green wavelength channels. (d) Reconstructed phase image at the same focal distance as (c). (e) Intensity image at different focal plane, using the red and green wavelength channels for reconstruction. (f) Phase image at the same focal distance as (e).

This situation is illustrated in Fig. 4.5(a). We can instead consider

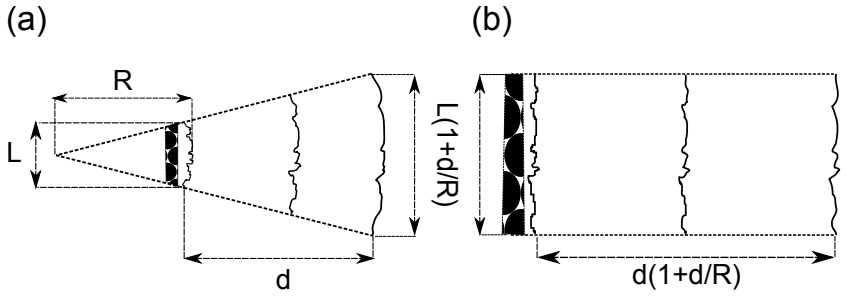

Figure 4.5: (a) Illumination of a sample of size L with a wavefront with a radius of curvature R and propagation by a distance d, which will have the same intensity distribution as (b), where the sample is illuminated by a flat wavefront and the sample size and propagation distance are magnified by (1+d/R).

a parallel beam of the same size by simulating a infinitesimally small telescope by multiplying the A term with $1 + \frac{d}{R}$ and the D term with A^{-1}. If we then propagate by a distance $d(1 + \frac{d}{R})$:

$$\begin{pmatrix} 1 & d(1+\frac{d}{R}) \\ 0 & 1 \end{pmatrix} \begin{pmatrix} 1+\frac{d}{R} & 0 \\ 0 & (1+\frac{d}{R})^{-1} \end{pmatrix} = \begin{pmatrix} 1+\frac{d}{R} & d \\ 0 & (1+\frac{d}{R})^{-1} \end{pmatrix}, \quad (4.3)$$

we get the same A and B terms in the final matrix, or the same intensity distribution of the beam at the detector plane, illustrated in Fig. 4.5(b). Because of this similarity, the reconstruction will often converge to the latter situation, even though the first situation would describe the experiment. This still yields the correct image, but the true scale needs to be determined from the experimental geometry or a calibration measurement. In practice, we therefore calibrate this scaling factor $(1 + d/R)$ from the recorded images, as this is equivalent to determining the wavefront curvature, but more convenient to implement numerically.

The known size of a sample can be used to calculate the magnification of the objects in focus. For the beads shown in Fig. 4.3 the magnification depends on the distance of the bead to the camera: because of the thickness of the flow cell, individual beads need to be refocused using different propagation distances. This leads to a higher magnification for beads that are further away from the camera. In this experiment, beads are observed with a magnification ranging from 4.1 to 4.4.

4.7 Conclusion

We have demonstrated a compact lensless microscope, employing a bare RGB-detector and three different illumination wavelengths delivered through a single-mode fiber, which has the capability to generate refocusable video images of complex objects with better than 2.2 μm resolution and video-like framerate. The exposure time is only limited by the intensity of the illuminating source, which makes it possible to view images of moving samples and live *C. elegans* without motion-induced artefacts. These refocusable video setups can be very useful when size constraints are an issue or when many cameras are to be used simultaneously, which is a situation that is often encountered in high-throughput imaging applications such as imaging flow cytometry. The present lensless RGB microscope can provide an alignment-free, cost-effective solution for various applications in life science and medical diagnostics.

Chapter 5

The pump laser and the optical parametric amplifier

Abstract

We report on a high power quasi-CW pumped Nd:YAG laser system, producing 130 mJ, 64 ps pulses at 1064 nm wavelength with a repetition rate of 300 Hz. Pulses from a Nd:YVO_4 oscillator are first amplified by a regenerative amplifier to the mJ level and then further amplified in quasi-CW diode pumped Nd:YAG modules. Pulsed diode pumping enables a high gain at repetition rates of several hundred Hz, while keeping thermal effects manageable. Birefringence compensation and multiple thermal-lensing-compensated relay-imaging stages are used to maintain a top-hat beam profile. After frequency doubling, 75 mJ pulses are obtained at 532 nm. The intensity stability is better than 1.1%, which makes this laser an attractive pump source for a high-repetition rate optical parametric amplification system.

5.1 High Energy, High Repetition Rate Picosecond Pulses from a Quasi-CW Diode Pumped Nd:YAG System

High-energy ultrashort laser pulses are used in high-harmonic generation schemes for the production of coherent radiation in the ultraviolet and

This section is adapted from: D. W. E. Noom, S. Witte, J. Morgenweg, R. K. Altmann, and K. S. E. Eikema, "High-energy, high-repetition-rate picosecond pulses from a quasi-CW diode-pumped Nd:YAG system," *Optics letters*, vol. 38, pp. 3021–3, aug 2013

soft X-ray spectral region [40]. These pulses can be produced with optical parametric chirped pulse amplification (OPCPA) [69], which is particularly suited for the generation of intense few-cycle pulses. OPCPA combines the high energy of long, narrowband pump pulses with the broadband spectrum of ultrashort seed pulses.

The main challenge in OPCPA development is the relatively high technical demands placed on the pump laser. The pump pulse duration should be matched to that of the stretched seed pulse [69], which is typically in the picosecond range, as excessive pulse stretching results in problems with low seed intensity, and complicates recompression. At the same time, both a high pulse energy and high repetition rate are desirable for many experiments.

High-energy pump pulses are generally produced in a master-oscillator power-amplifier scheme, where the generation of pulses is decoupled from the high-power amplification. Amplifier construction depends on the properties of the used gain materials, such as Nd- or Yb-doped crystals. Yb:YAG has gained a lot attention lately because of its favorable properties as a gain material. It has a high saturation fluence, and cryogenic cooling improves thermal conductivity and also transforms this medium from a quasi-three level to a more favorable four level system. Yb:YAG has been used in Innoslab [70], disk [71][72] and rod [73][74] schemes. Yb has also been used in different host materials, such as Yb:GSAG [75] and Yb:YLF [76] to increase the gain bandwidth.

Nd:YAG on the other hand is a well established material which has been widely used in flashlamp-pumped cylindrical rod amplifiers. However, the repetition rate of such systems has typically been limited to the 10 Hz range [77][78], due to both the excessive thermal load and the limited number of shots before degradation of the flashlamps. New developments in laser diode engineering have made it possible to use quasi-continuously (QCW) pumping diodes in amplification modules. These QCW diodes enable a much more efficient pumping as they can be turned off between consecutive pulses. This strongly reduces the thermal load on the gain medium while preserving a high gain. As a result, the repetition rate can be increased by more than an order of magnitude.

In this paper we report our results on a quasi-cw diode pumped, Nd:YAG based amplification system which delivers 75 mJ, 64 ps pulses at a wavelength of 532 nm and a repetition rate of 300 Hz. For homogeneous amplification in the OPCPA, and to maximize energy extraction, a top hat beam profile is implemented. Thermal birefringence compensation is used in combination with relay imaging to generate this beam profile

with a flat wavefront at 1064 nm, resulting in efficient frequency doubling after amplification. The total footprint of the laser system is less than 1.8 m^2.

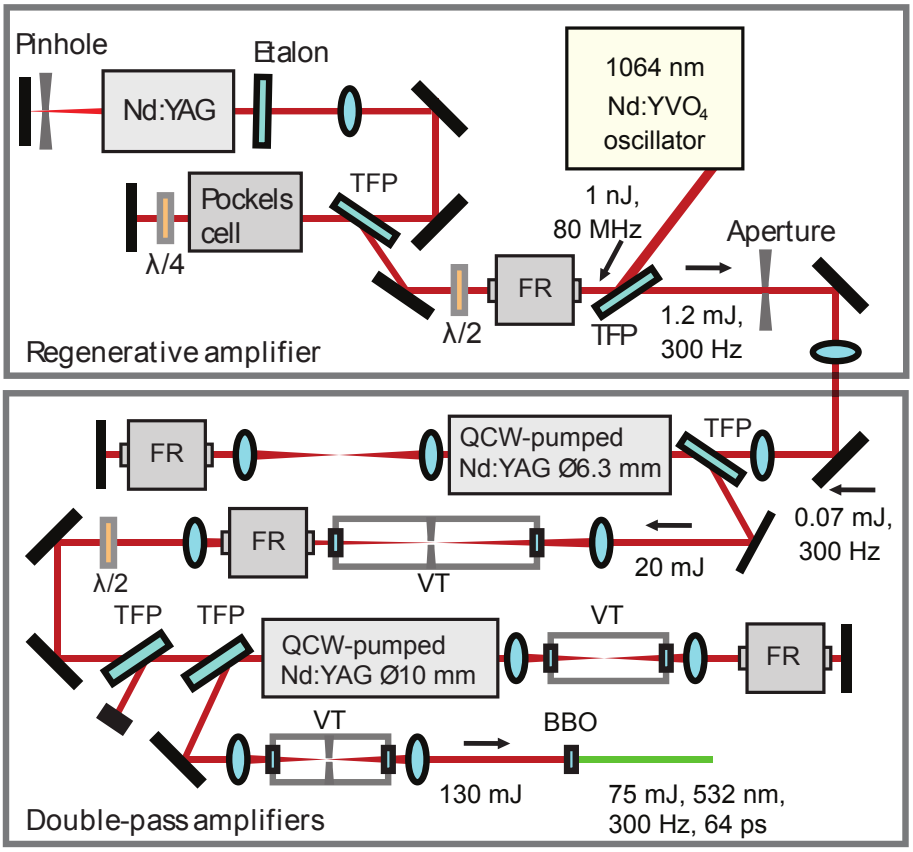

Figure 5.1: Schematic of the developed Nd:YAG regenerative amplifier and quasi-CW-pumped post-amplifier system. TFP, thin-film polarizer; $\lambda/2$, half-wave plate; $\lambda/4$, quarter wave plate; FR, Faraday rotator; VT, vacuum tube.

The setup is shown in Fig. 5.1. First, pulses are generated in a home-built Nd:YVO_4 oscillator, pumped with an 18 W, 880 nm CW diode laser. A semiconductor saturable absorber mirror inside the laser cavity ensures passive modelocking. The oscillator provides 60 nJ, 10 ps pulses at 80 MHz repetition rate at 1064 nm wavelength. After reducing the energy to 1 nJ to lower the background output of unamplified pulses, the output is used to seed a regenerative amplifier.

Inside the regenerative amplifier a Nd:YAG rod is pumped with CW laser diodes. A Pockels cell is switched on at 300 Hz, for a duration of 500 ns, to keep a single pulse travelling in the cavity for amplification in 60 roundtrips. A 0.5 mm thick intracavity etalon stretches the pulses in the regenerative amplifier to 64 ps, to reduce the peak intensity and to match the stretched pulse length from a Ti:sapphire oscillator which will later be used to seed an OPCPA system.

The 1.2 mJ output pulses of the regenerative amplifier are amplified in two modules from the REA-series manufactured by Northrop Grumman, containing QCW diode pumped Nd:YAG rods. The first module has a cylindrical rod of 6.35 mm diameter and 146 mm length. Five rows of 24 diode bars are placed around the rod. The operating voltage of the diodes is 240 V and the maximum possible peak drive current is 145 A. It is operated at 85.5 A for 245 microseconds for each pulse, which matches the upper state lifetime of the Nd:YAG gain medium. In the second module the rod diameter is 10 mm. This module has a maximum possible current of 175 A, but it is also operated at 85.5 A.

Before seeding the double-pass amplifiers, two cylindrical lenses reduce astigmatism from the output of the regenerative amplifier. To produce a flat intensity profile in the modules, the beam is increased in size by a telescope before it is passed through a 5.5 mm aperture. This reduces the pulse energy to 0.07 mJ. The beam at the aperture is then relay-imaged inside the Nd:YAG rod of the first module. We define the front (end) face of the modules as the side where the incoming beam first enters (exits) a module. After the beam exits the first module at the end face, it is relay-imaged onto a mirror and then relay-imaged inside the rod again. This is done to preserve the flat intensity profile at the modules and at the Faraday rotators which are used to compensate thermal birefringence (discussed in more detail below). After double-passing the first module, the beam reflects off a thin film polarizer (TFP) and is relay-imaged onto the end face of the second module. In the focus between the image planes a 3 mm diameter aperture is used to block backreflections, and from there on vacuum tubes are used to avoid nonlinear effects in air at locations where the beam is focused. In our current setup, the total gain of the modules is 2×10^3, and thus the total extinction ratio of the TFPs should be at least $\sim 10^3$ to prevent damage to optics. For this reason, two polarizers are used in front of the last Nd:YAG module.

Heating of the crystal rods by the pump diodes, combined with surface cooling, leads to a nonuniform temperature distribution inside the rods. The resulting thermal-stress-induced birefringence has radially and

tangentially directed principal axes [79]. This results in beam profile deformations after interaction with optics with a polarization-dependent reflectivity. When the beam travels the same path through the rod twice with a 90 degrees polarization rotation in between, both the radial and tangential polarization will have traveled the same optical path length, which compensates thermal birefringence effects [80]. This principle is implemented through a Faraday rotator in the imaging setup behind each module. The compensation is optimized by moving the position of the end mirror in this setup. From test experiments, we find that the end face of a module should be relay-imaged onto itself for optimal compensation.

The radial variation of the refractive index in the crystal rods is temperature- and stress-dependent, and together with end-face bulging this causes the rods to act as a lens. This lensing effect is mitigated by placing the lenses in each imaging setup closer together than would be required in a standard 4f relay-imaging setup.

After passing through the entire amplifier system, pulses of 130 mJ are produced at 1064 nm. We limit the pulse energy at this value to reduce the risk of damage to the Nd:YAG rods and end-face coatings. Pulses at 532 nm wavelength are generated by second harmonic generation (SHG) in a $14 \times 14 \times 3$ mm^3 BBO crystal. Figure 5.2 shows the resulting energy per pulse at 532 nm for different 1064 nm pulse energies. The conversion efficiency at an input pulse energy of 130 mJ is 58%. We characterized the stability of the system by measuring the pulse-to-pulse fluctuations of both the input and amplified output pulses. We find that both are stable within 1.1% rms, which is an upper bound, as the measurement was limited by electronic noise in the detection system. Furthermore, we have performed energy stability measurements over longer timescales, and find that the output remains stable to within 1.2% rms over several tens of minutes of continuous operation. An autocorrelation trace is shown in Fig. 5.3. The measured autocorrelation fits very well to a Gaussian curve, and from this fit we derive a pulse length of 64 ps.

Because a flat gain profile in the OPCPA is desirable and damage depends mostly on the peak intensity, it is imperative that a flat intensity profile is maintained at critical surfaces. The top-hat beam profile will be distorted when it passes through apertures away from the image planes. Since the rods are transversely pumped, the homogeneity of amplification depends on how well the pump spectrum is absorbed in Nd:YAG. This spectrum, and therefore the absorption, depends on

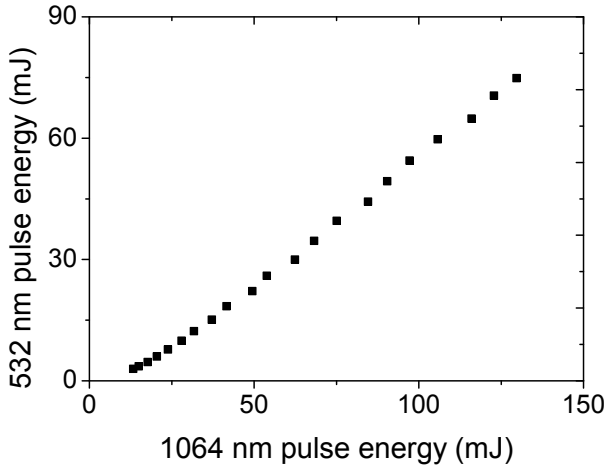

FIGURE 5.2: Output pulse energy at 532 nm after second harmonic generation plotted against the 1064 nm input pulse energy.

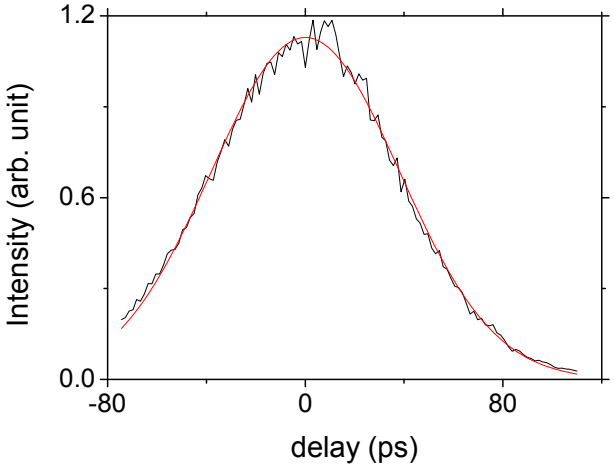

FIGURE 5.3: Measured autocorrelation trace and Gaussian fit. The fit has a full width at half maximum of 90 ps, which would indicate a pulse length of 64 ps for a Gaussian temporal profile.

the temperature of the diodes. When this temperature is optimized for maximum absorption, the amplified beam profile shows a dip in the cen-

ter. In the final design, the temperature of the diodes was adjusted in combination with the driving current to the laser diodes to increase the absorption length and homogenize the transverse gain profile in the amplifier. We measured the infrared beam profile (without SHG) and the green beam profile separately with imaging setups when the system was running at full power. Good quality top-hat beam profiles are obtained in both cases, as can be seen from Fig. 5.4.

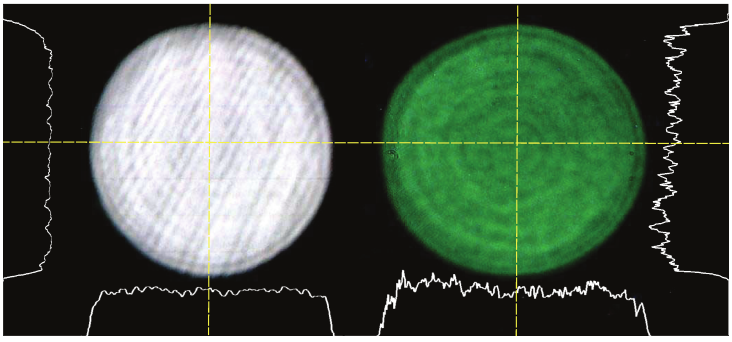

Figure 5.4: Transverse beam profiles of the amplified pulses at 1064 nm (left) and after frequency doubling to 532 nm (right), measured at the position of the BBO crystal via relay imaging. Single-line cross-sections at the dashed lines are included. Note that the diagonal fringes in the 1064 nm image are an artefact, due to interferences in the CCD camera. Some spots are visible in the 532 nm beam, which are caused by dust particles on neutral grey filters and the CCD itself.

To conclude, quasi-CW diode pumping provides the efficiency required to effectively use Nd:YAG as a gain material at high repetition rates. The high pulse energies and repetition rate of this system are ideal for pumping high-intensity few-cycle OPCPA. Such OPCPA systems, in turn, are an excellent starting point for high-flux generation of soft X-rays. Cryogenics are avoided, which results in a fairly simple setup compared to Yb:YAG systems. The power, stability and transverse beam profile all reach the requirements needed to pump a high power optical parametric amplification system.

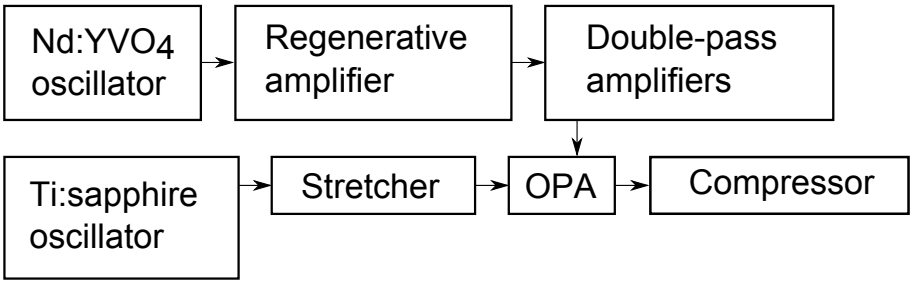

FIGURE 5.5: An overview of the setup for generating milijoule femtosecond pulses.

5.2 The optical parametric amplifier

The double-pass amplifier system is used to pump an OPA, which is seeded by stretched Ti:sapphire pulses (see Fig. 5.5). The setup for the optical parametric amplifier is shown in Fig. 5.6. In this amplifier a powerful 532 nm pump beam is used to parametrically amplify a beam from a Ti:Sapphire oscillator in three separate BBO crystals. There are several aspects important for the design of the system: the pump beam should be split up in such a way that there is a high pump intensity at the first two crystals, but most of the power should be in the third crystal. This is because in the first two passes a lot of gain is required but a high power would be wasted here because of the low seed/signal beam strength that does not saturate the parametric process yet. In the third pass the signal is stronger and a lot of energy is transferred to the signal beam. The power that is split off to the first arm and thus the first two crystals of the OPA setup, is optimized in such a way that the amplification in the first two crystals is as saturated as possible, but optical damage and parametric fluorescence is prevented. About 1.6 W out of the total 23 W pump laser is split off into the first arm, so the loss of a few hundred mW of power in the second arm to push the first arm into saturation will only reduce the maximum power after the third crystal with 1 percent, which is acceptable. The output of the OPA is 10 mJ, which gives an efficiency of 13% and after compression 4 mJ is left.

Damage to optics is another concideration. The pump beam is imaged on each crystal to prevent damage resulting from a high peak intensity at hot spots. The pump beam close to the crystals can be intense enough to damage mirrors, and therefore some mirrors in the pump

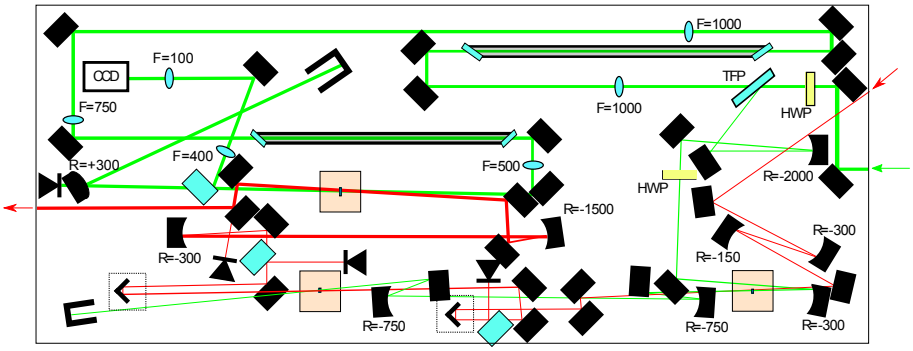

Figure 5.6: The setup for the optical parametric amplifier. TFP, thin-film polarizer; HWP, half-wave plate. The 532 nm pump beam comes in from the right side and the power is split using a half-wave plate and a thin-film polarizer. The seed beam comes in from the upper right, is made smaller and passes through the first crystal. It then goes to the next crystal via a translation stage to adjust the timing, and then again towards the third stage where the beam is also enlarged. After every stage the power of the signal pulses are monitored with photodiodes. The pump beam is imaged on each crystal, it is checked for deformations after passing through the whole setup and a photodiode is used to measure pump depletion in the last stage. The pump beam passes through vacuum tubes at focal points of the relay-image telescopes to prevent breakdown in air.

beam to the first and second crystals were moved further from the crystals. When the beam is focused in relay-image stages, nonlinear effects can occur in air which destabilize the beam. This is prevented by using vacuum tubes.

Even though the pump beam is relay imaged through the double-pass amplifiers and the OPA and the intensity profile is close to a top-hat, the phase profile is distorted by the thermal stress in the amplifying rods. This reduces the efficiency of the OPA because of changed phase-matching conditions.

There are two ways of setting up the beams and crystals for the right phasematching angles. In one situation there is also phasematched frequency doubling of the signal beam. This generated beam is especially powerful after the third crystal and can be dangerous to the crystal, and also the eyes because optics are not fit for this wavelength and unwanted reflections and tranmissions are not captured.

The pump beam is so powerful that even transmission through mirrors optimized for reflection at 532 nm and reflection of anti-reflection

coated optics should be taken into account for safety. One important case is the reflection of the pump beam off the anti-reflection coating of the third crystal. If everything is set up such that signal frequency-doubling is minimized, the pump beam reflection can not to be blocked without also blocking the seed beam. Because of this we had to tilt the crystal slightly so it would reflect downwards.

Optical parametric amplification is an instantaneous process, so pulse timing is crucial. First, the Ti:sapphire oscillator repetition rate has to be a mutiple of the rate of the Nd: YVO_4 oscillator used for the 532 nm pump beam. This is done by using the signal from two fast photodiodes for a PID-controller which sends feedback to a mirror on a piezo in the Ti:sapphire laser cavity. Because a 60 ps long pulse is only 18 mm long, while pulses from an 160 MHz repetition rate laser are 6 ns, or 1.80 m apart, the arrival time of pump and seed pulses are first measured on a fast photodiode, and then the amplification of the signal beam is used for finding the correct timing (and therefore optical path length). In principle the signal and pump laser pulses need to coincide in the crystal within $\sim$1 ps or better for optimum amplification and stability.

Angles between the pump beam and the seed beam in each crystal are optimized for broadband phase matching (see section 2.3). The crystals are on rotational stages to make angular alignment easier, and to set the phase matching angle ($\theta \approx 24°$) between the pump beam and the optical axis of the crystal. The spectrum of the Ti:sapphire oscillator has been measured and is shown in Fig. 5.7. The spectrum after the OPA and after the compressor is shown in Fig. 5.8.

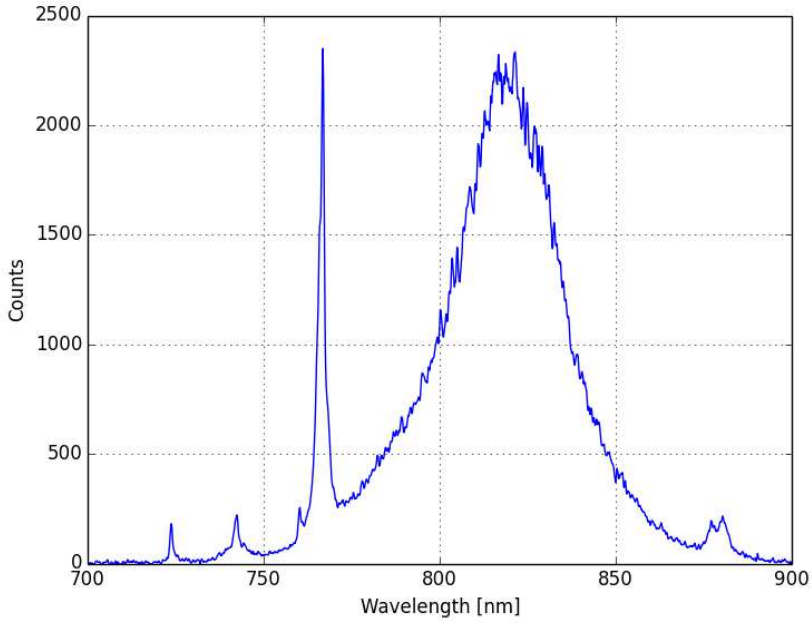

Figure 5.7: Spectrum of the Ti:sapphire oscillator used to seed the OPA. This spectrum is relatively narrow, and a better functioning Ti:sapphire laser could greatly improve the peak power after the OPA. In fact, a new Ti:sapphire laser producing a 200 nm FWHM spectrum was installed after completion of these experiments, so that an improved output is expected in the near future.

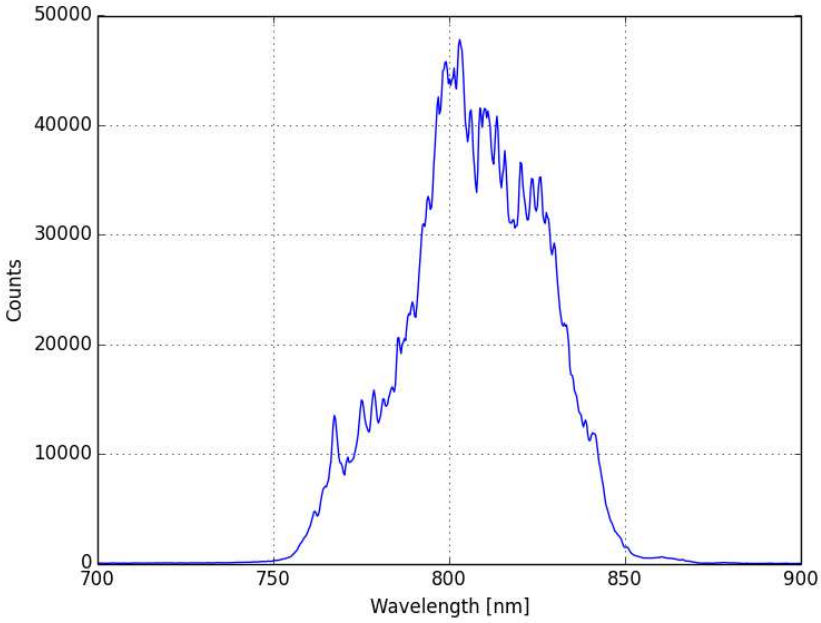

FIGURE 5.8: Spectrum of the OPA after compression. Because of the narrow seed bandwidth, this result does not yet show the broad-bandwidth amplifying capabilities of the noncollinear OPA. In principle this OPA should be able to amplify from 720-1030 nm when seeded with an oscillator covering the same spectral range [78].

Chapter 6

Lensless diffractive imaging with ultra-broadband table-top sources: from infrared to extreme-ultraviolet wavelengths

Abstract

Lensless imaging is an approach to microscopy in which a high-resolution image of an object is reconstructed from one or more measured diffraction patterns, providing a solution in situations where the use of imaging optics is not possible. However, current lensless imaging methods are typically limited by the need for a light source with a narrow, stable, and accurately known spectrum. We have developed a general approach to lensless imaging without spectral bandwidth limitations or sample requirements. We use two time-delayed coherent light pulses, and show that scanning the pulse-to-pulse time delay allows the reconstruction of diffraction-limited images for all spectral components in the pulse. In addition, an iterative phase retrieval algorithm is introduced, which uses these spectrally resolved Fresnel diffraction patterns to obtain high-resolution images of complex extended objects. We demonstrate this two-pulse imaging method with octave-spanning

This chapter is adapted from: S. Witte, V. T. Tenner, D. W. E. Noom, and K. S. E. Eikema, "Lensless diffractive imaging with ultra-broadband table-top sources: from infrared to extreme-ultraviolet wavelengths," *Light: Science & Applications*, vol. 3, p. e163, mar 2014

visible light sources, in both transmission and reflection geometries, and with broadband extreme-ultraviolet radiation from a high-harmonic generation source. Our approach enables effective use of low-flux ultra-broadband sources, such as table-top high-harmonic generation systems, for high-resolution imaging.

6.1 Introduction

Lensless imaging is an elegant approach to high-resolution microscopy, which is rapidly gaining popularity in applications where the use of imaging optics is problematic. This situation occurs e.g. in imaging experiments using radiation at extremely short wavelengths, such as the extreme-ultraviolet (XUV) and X-ray spectral ranges, for which the development of good-quality imaging optics is highly complex [81, 82]. Another important application is the development of miniaturized visible-light microscopes, where imaging optics are avoided to optimize the size and cost of a device [48, 83].

In lensless imaging, an object is illuminated by a coherent light source, and the resulting diffraction pattern is recorded. An image of the object then has to be reconstructed numerically, which can be done by field propagation methods if both intensity and phase of the diffraction pattern are known. As only intensity is recorded in a typical diffraction measurement, the central issue in lensless imaging is the retrieval of phase information from a recorded diffraction pattern. Solutions to this problem have been found both through numerical and optical means [81, 84, 85]. In coherent diffractive imaging, the missing phase information is numerically reconstructed by iterative algorithms [24], which has been shown to have a unique solution as long as the oversampling condition is satisfied [52]. This condition can be satisfied by using either a finite object support [51, 86], a localized illumination profile [87], and/or recording multiple partially overlapping diffraction patterns [11, 88]. Holographic methods, which directly record the phase through interference with a separate reference wave, have also been developed in a lensless imaging context [85, 89].

There is a growing need for lensless imaging methods that operate with broadband radiation, to make much more efficient use of state-of-the-art light sources such as 3rd generation synchrotrons and table-top high-harmonic generation (HHG) sources for imaging. Especially HHG-based sources hold promise for compact and cost-effective ultrahigh-

resolution microscopy, and recent breakthroughs have led to the generation of a significant photon flux in the biologically important water-window spectral range [40, 90]. However, HHG sources intrinsically produce an ultra-broadband soft-X-ray spectrum, and the need to spectrally filter these sources leads to a reduction in flux of 3-4 orders of magnitude, which strongly limits their use for imaging applications. Several pioneering proof-of-concept experiments have already been performed with table-top HHG sources [91–96], and the ability to use the full flux of such a source for imaging could provide a breakthrough for practical imaging applications.

In general, the use of monochromatic radiation has always been a major requirement for any diffractive imaging experiment, since the angle at which light diffracts from any structure depends on its wavelength. A diffraction pattern generated by a polychromatic source will therefore consist of a superposition of diffraction patterns of all the individual spectral components [97]. Depending on the spectral bandwidth of the source, this effect limits the achievable resolution [98] , and for more broadband sources can inhibit image reconstruction entirely. By incorporating knowledge of the source spectrum into the reconstruction algorithm, discrete spectra [97] and finite bandwidths [99] can be handled. But such calculations require a stable, accurately calibrated source spectrum, and therefore remains limited to relatively narrow spectral bandwidths ($\Delta\lambda/\lambda \sim 0.028$ has been shown [99]).

We demonstrate that all bandwidth limitations on lensless imaging can be removed by illumination of the sample with two coherent time-delayed pulses (Fig. 6.1a). If a series of diffraction patterns as a function of the time delay between the two pulses is recorded, methods from Fourier-transform spectroscopy [100] can be used to obtain spectrally resolved information from the recorded diffraction patterns themselves. No additional measurement of the source spectrum is required, and the spectrum may be ultra-broadband, highly structured and even exhibit significant intensity fluctuations (see 6.6 for detailed simulations). Our two-pulse imaging method is universal and can be applied to any diffractive imaging experiment. In the following we illustrate this with experimental demonstrations for both Fresnel and far-field diffraction, for transmission and reflection geometries, and for diffractive imaging using an extreme-ultraviolet HHG source.

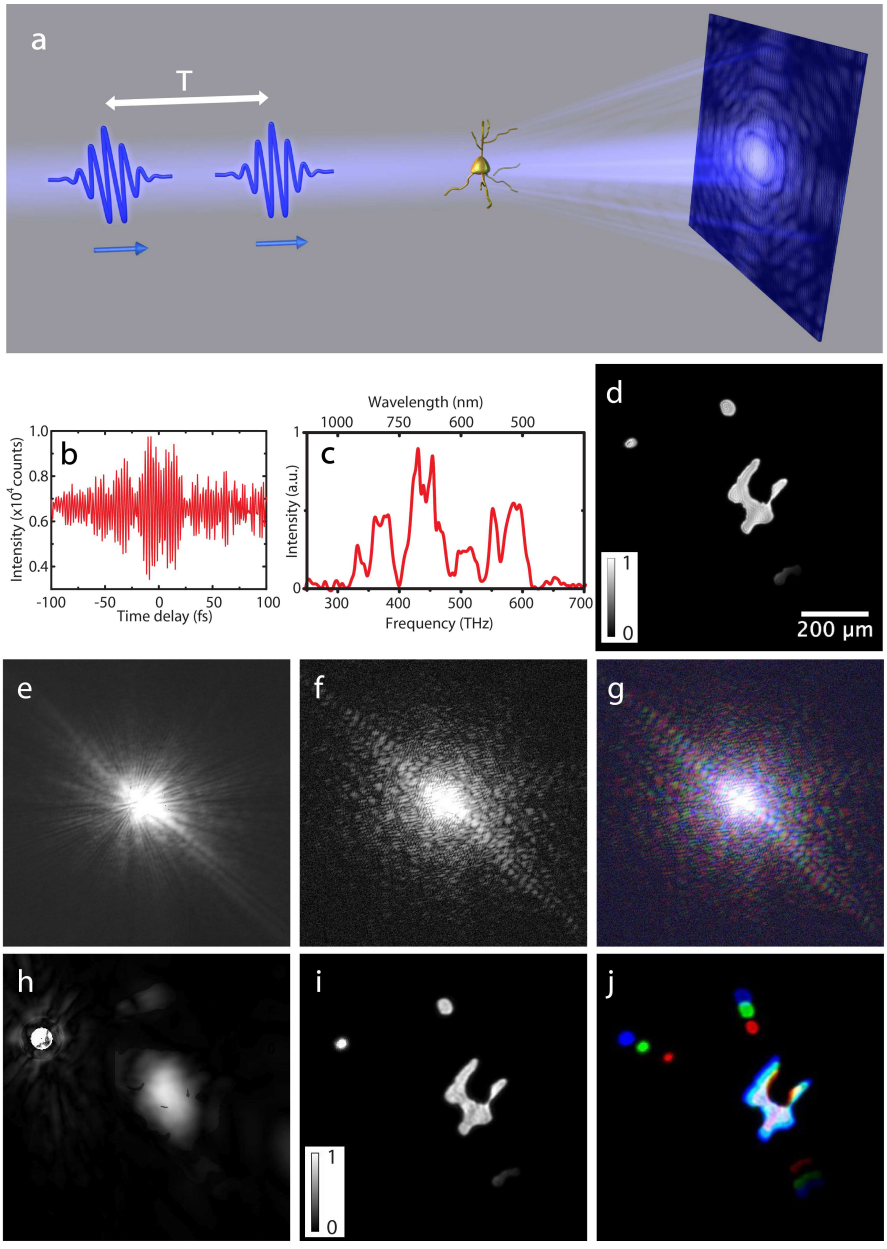
a
T
b
Intensity (x10^4 counts)
1.0
0.8
0.6
0.4
-100
-50
0
50
100
Time delay (fs)
c
Wavelength (nm)
1000
750
600
500
Intensity (a.u.)
1
0
300
400
500
600
700
Frequency (THz)
d
1
0
200 µm
e
f
g
h
i
1
0
j

Figure 6.1: (Previous page) Principle of two-pulse imaging and experimental results in the Fraunhofer regime. (a) A sample is illuminated with two coherent pulses, and a set of diffraction patterns is recorded as a function of time delay T in a lensless imaging geometry. (b) Typical signal recorded on a single pixel during a coherent diffractive imaging experiment using two pulses, as a function of time delay T. (c) Fourier transform of the signal in 1b, showing the spectrum of the light that diffracted onto that specific pixel. By reconstructing such spectra for all pixels, spectrally resolved diffraction patterns can be extracted throughout the full source spectrum. (d) White-light microscope image of a laser-machined sample, containing transmitting structures in a gold layer. (e) Measured far-field diffraction pattern (log-scale) using the full source spectrum. (f) Reconstructed diffraction pattern (log-scale) at 565 nm wavelength, retrieved from a two-pulse scan. (g) Overlay of three different retrieved diffraction patterns (log-scale) at wavelengths of 508, 565 and 694 nm, respectively. (h) Result of iterative phase retrieval using the broadband diffraction pattern of e. No image can be retrieved due to the excessive spectral bandwidth. (i) Result of iterative phase retrieval using a diffraction pattern retrieved from the two-pulse scan (from f). (j) Overlay of three independent reconstructed images from the diffraction patterns in g, which all show good-quality images of the sample. The field-of-view is wavelength-dependent, resulting in a different image size for each wavelength.

6.2 Materials and Methods

6.2.1 Two-pulse imaging with an ultra-broadband source

When performing lensless imaging with an ultra-broadband source, the recorded ultra-broadband diffraction patterns can be interpreted as a linear superposition of monochromatic diffraction patterns. Knowledge of the superposition coefficients would therefore enable spectral decomposition of the diffraction patterns into the individual spectral components. In practice, this means that we need a way to measure the distribution of spectral components that have scattered onto each camera pixel (see section 6.6 and Fig. 6.5 for details). The key point of our method is that spectral decomposition of the diffraction patterns can be achieved by recording the scattering signal for all individual camera pixels as a function of the pulse-to-pulse time delay (Fig. 6.1b). For each pixel, this delay-time dependent signal is equal to Fourier-transform of the spectrum of the light scattered onto that individual pixel. Therefore a Fourier-transform converts it back to the frequency domain, and reveals the spectral components scattered onto each pixel (Fig. 6.1c). With this information, spectrally resolved diffraction patterns can be recon-

structed throughout the entire source spectrum from a single time-delay scan (see section 6.6 for details). The spectral resolution is inversely proportional to the scanned time delay, similar to Fourier-transform spectroscopy [100]. A powerful feature of this approach, common to many Fourier-transform-based methods [100–102], is that the full source spectrum is used throughout the entire measurement, resulting in an efficient use of the available photon flux.

6.2.2 Two-pulse imaging in the Fraunhofer regime

For the first experimental realization of two-pulse imaging at visible wavelengths, we use a spatially coherent octave-spanning continuum as the light source. Two time-delayed pulses are generated in a scanning Michelson interferometer, and sent into a lensless imaging setup (Fig. 6.6). Coherent white-light continuum pulses are produced by launching ultrashort laser pulses into a photonic crystal fiber. A time-delayed pulse pair is produced with a Michelson interferometer, with one of the end mirrors mounted on a closed-loop piezo stage. The pulse pair is then used to illuminate a sample, and the diffracted light is recorded with a 14-bit CCD camera with 1936x1456 pixels and 4.54 μm pixel size. We typically acquire 500 individual images with 0.01 to 1 millisecond exposure time, while increasing the time delay in 0.67 fs (200 nm) steps. As a proof-of-concept experiment, we image a test sample shown in Fig. 6.1d, which consists of some small structures that have been laser-etched in a gold layer deposited on a glass substrate. We achieve far-field conditions by positioning the CCD camera at 5 cm behind an f = 5 cm lens located behind the sample, which ensures both a far-field imaging geometry and a moderate NA for visible wavelengths.

6.3 Results

The measured diffraction pattern using the full source spectrum is shown in Fig. 6.1e. A strong radial smearing is present: due to the wavelength-dependent diffraction angle, each point in the diffraction pattern is convolved with a large spectral bandwidth in the radial dimension. However, from the two-pulse scan and Fourier transformation, quasi-monochromatic diffraction patterns are obtained (Fig. 6.1f), in which the radial structure of the diffraction pattern is clearly resolved. The spectral bandwidth of these retrieved images is determined by the length of the two-pulse scan, and can readily be made sufficiently small (by a longer delay scan)

to consider the images as monochromatic. Fig. 6.1g shows an overlay of three diffraction patterns at different wavelengths, obtained from a single two-pulse scan. The dramatic improvement in image reconstruction is clearly visible from Figs. 6.1h-j, in which an iterative phase retrieval algorithm is applied to retrieve an image from the diffraction patterns in Figs. 6.1e-g. For the phase retrieval, a support was defined from the autocorrelation of the diffraction pattern, after which 300 iterations of the error reduction algorithm [51] are used with a random initial phase guess. The algorithm is run 20 times, and the results are averaged into the final image. Due to the low coherence in the unresolved broadband diffraction pattern of Fig. 6.1e, the requirements for applying Gerchberg-Saxton-type iterative phase retrieval algorithms are not satisfied, and the resulting image (Fig. 6.1h) is extremely poor. In stark contrast, the image reconstructed from the two-pulse scan (Fig. 6.1i) is a high-quality image of the test object, with a diffraction-limited resolution of 6 μm (limited by the NA of 0.046). Three reconstructions at different wavelengths, corresponding to the diffraction patterns shown in Fig. 6.1g, are overlaid in Fig. 6.1j. All reconstructions provide a clear image of the test object, but their relative sizes are different due to the wavelength-dependent field-of-view discussed above. After appropriate scaling, all these images can be averaged to improve the final signal-to-noise ratio. In this case, the full source spectrum is used efficiently for image reconstruction.

6.3.1 Multi-wavelength phase retrieval

The spectrally resolved diffraction data provides also new possibilities for fast and robust phase reconstruction, based on propagation effects in coherent diffractive imaging in the Fresnel regime. In the far field (Fraunhofer) regime discussed before, the only effect of propagation is a global scaling of the diffraction pattern. However, in the Fresnel regime there is an additional propagation and wavelength-dependent spatial phase evolution. This propagation-dependent phase evolution can be exploited for more robust phase retrieval strategies, based on the knowledge of the wavefront curvature [103–105] or by performing measurements at multiple sample-to-camera distances [53, 65]. We have developed a novel iterative phase retrieval scheme, which explicitly uses the recorded multi-wavelength data to reconstruct the phase without the need for support constraints. In the Fresnel regime, wave propagation couples amplitude

and phase of an electric field through the Fresnel diffraction integral:

$$E(x,y,z) = \frac{e^{i2\pi z/\lambda}}{i\lambda z} \iint E(x',y',0) e^{\frac{i\pi}{\lambda z}[(x-x')^2+(y-y')^2]} \,\mathrm{d}x'\mathrm{d}y' \qquad (6.1)$$

where propagation is along the z-coordinate, and λ is the wavelength of the light. Equation (6.1) states that Fresnel propagation depends on distance and wavelength in an identical way (aside from a global phase factor), allowing us to exploit our spectrally resolved diffraction data to propagate between different spectral components, as schematically depicted in Fig. 6.2a. This scheme does not require sample or camera movement, and only relies on measured diffraction patterns at multiple wavelengths as input. It converges reliably and works for extended samples. Keyhole imaging [87, 106] and ptychography [11, 88] have also been used successfully to image parts of extended samples, but our multi-wavelength approach does have the advantage that spatially confined illumination is not required for stable convergence. To demonstrate this multi-wavelength phase retrieval approach, we record two-pulse scans of Fresnel diffraction patterns of a fixed sample of Convallaria majalis (Lily of the Valley) rhizome, of which a broadband diffraction pattern is shown in Fig. 6.2b. Fig. 6.2c shows a narrow-band ($\Delta\lambda = 5$ nm) diffraction pattern of this Convallaria sample at a wavelength of 695 nm, which has been extracted from a two-pulse imaging scan. Sharp diffraction features are clearly visible, which were washed out in the broadband images. For our multi-wavelength Fresnel reconstruction method, phase retrieval is performed in a Gerchberg-Saxton type iterative scheme, where the intensity data from the first wavelength is propagated to the next wavelength through evaluation of the Fresnel propagation equation (6.1). After propagation, the phase information is retained, while the intensity is replaced with the measured intensity at this new wavelength. A detailed description of the multi-wavelength phase retrieval algorithm is provided in section 6.6. The choice of wavelengths to be used in the reconstruction is flexible: the main requirement is that they are spectrally sufficiently separated to display significant differences after propagation over a distance z, i.e. the phase term inside the integral in Eq. (6.1) should change by a measurable amount between wavelengths for a detector pixel at position (x,y). This phase shift condition depends on the detection geometry and is readily fulfilled in practice. We typically select 2-5 images separated by 5-20 THz in frequency from the spectrally resolved dataset for iterative phase retrieval. The algorithm converges rapidly, typically requiring only 10-50 iterations to reach a fi-

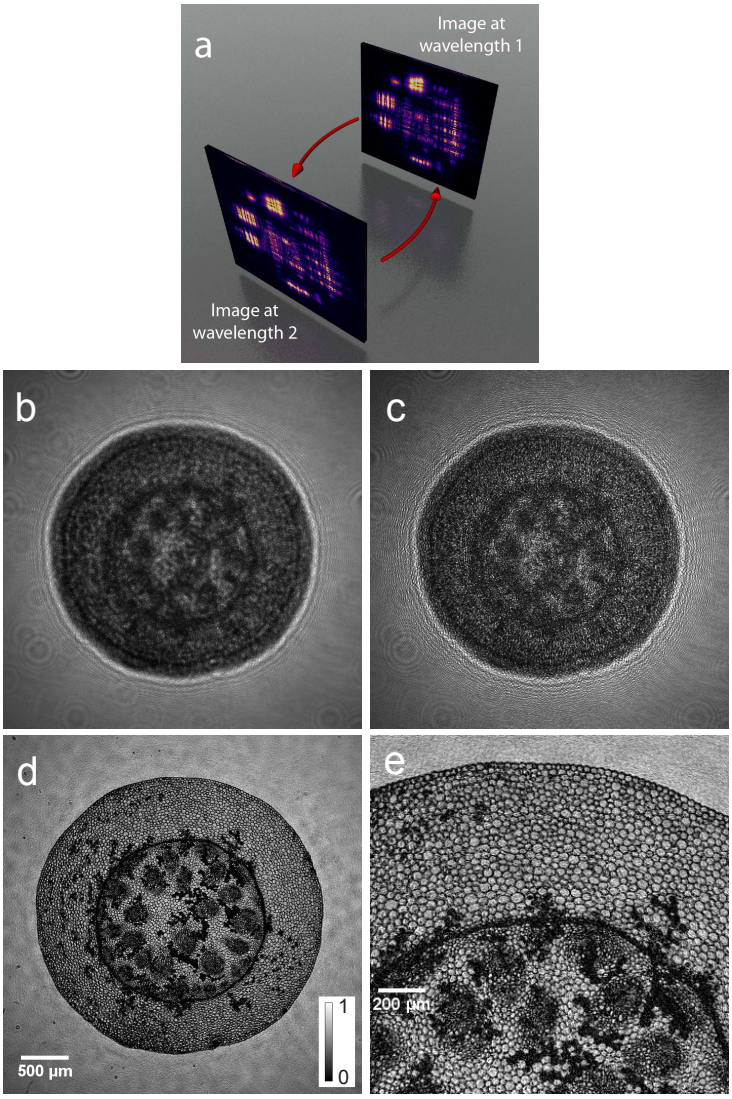

Figure 6.2: Multi-wavelength phase retrieval in the Fresnel regime. (a) Graphic representation of the multi-wavelength phase retrieval algorithm. Iterative propagation is performed between Fresnel diffraction patterns recorded at the same distance, but with different wavelengths. (b) Broadband Fresnel diffraction pattern of Convallaria majalis rhizome, recorded with an octave-wide visible light source. (c) Quasi-monochromatic Fresnel diffraction pattern of the same Convallaria sample as in b, obtained from a two-pulse imaging scan. Much finer diffraction features are visible. (d) Resulting image after 25 iterations of the multi-wavelength iterative phase retrieval, using diffraction patterns at 5 different wavelengths. (e) Zoom-in on a part of the reconstructed image, clearly showing the individual cells. The intensity scale bar in Fig. 6.2d also applies to this image.

nal solution. While the algorithm already works with two images, the use of more wavelengths usually provides superior results. When more wavelengths are used, the algorithm averages over more independent datasets, causing noisy pixels in a single image to be less influential. The multi-wavelength phase retrieval algorithm results in a high-quality image reconstruction, which is displayed in Fig. 6.2d. Since the sample fills most of the field-of-view (FOV) and consists of dark structures on a bright illuminated background, the oversampling condition is not satisfied and support-based phase retrieval algorithms would not provide a solution in this situation. In contrast, our multi-wavelength algorithm enables image reconstruction at instrument-limited resolution, clearly showing the individual cells as well as some sub-cellular features (Fig. 6.2e). After the phase has been retrieved, all spectrally resolved images can be propagated to the object plane and averaged to improve signal-to-noise, resulting in an efficient use of the full source spectrum. The resolution of such a reconstruction is then determined by the imaging geometry and the weighted mean of the spectral bandwidth. The main prerequisite of our multi-wavelength phase retrieval approach is that the phase profile of the object has the same spatial structure for the spectral components used in the reconstruction. However, it should be stressed that the phase does not need to be constant as a function of wavelength: a known wavelength-dependent refractive index can readily be incorporated into the algorithm, as this only requires an additional refractive-index-dependent multiplication factor upon propagation between different wavelength images. Therefore, our multi-wavelength phase retrieval approach extends to dispersive samples, and can be used for lensless imaging with short wavelengths. Wavelength-dependent differences in absorption result in different signal intensities for the respective images, and can also still provide a good-quality reconstruction. Only in the case where the phase images are qualitatively different at the different wavelengths, e.g. due to an elemental absorption edge between the wavelengths that are used, then the algorithm would not converge. In this case, support-based iterative phase retrieval schemes can still provide image reconstruction, provided that the object meets the oversampling requirements that are required for such algorithms to converge [24].

6.3.2 Lensless imaging in reflection

In addition to transmission imaging, lensless imaging in a reflection geometry is important for many applications in nanoscience and technology

[82, 107]. The need for a finite support is particularly challenging to satisfy for reflection geometries [108], which has therefore mostly relied on finite-beam-size methods such as ptychography. In contrast, our multi-wavelength approach enables imaging of large areas of extended samples in a reflection geometry (Fig. 6.3a). Fig. 6.3b shows a spectrally resolved Fresnel diffraction pattern, retrieved from a two-pulse scan in reflection of a USAF 1951 test target. The reconstructed image obtained through multi-wavelength phase retrieval is shown in Fig. 6.3c, demonstrating the ability to image large reflective samples without support requirements.

In a coherent diffractive imaging (CDI) experiment, the achievable diffraction-limited resolution is determined by the wavelength of the light and the numerical aperture of the detection geometry (i.e. the size of the camera and the sample-to-camera distance). In the Fresnel geometry, also the CCD pixel size influences the final resolution. This resolution defines the distance between adjacent sampling points, and the field-of-view is then determined by this distance multiplied by the number of pixels in each dimension. Therefore, the FOV is also wavelength dependent. As a consequence, when three diffraction patterns of an object are recorded at different wavelengths, the shorter wavelength pattern will have a slightly smaller FOV than the longer wavelength patterns. In the reconstruction, the FOV will therefore be limited by the shortest wavelength used. This is illustrated in Fig. 6.3c, where the red dashed line indicates the FOV for the shortest wavelength. Outside this line, not all wavelengths contribute to the reconstruction, which results in aberrations.

In general, the iterative phase retrieval algorithm provides accurate phase information. If the diffraction comes from a pure surface reflection, this phase information can be used to reconstruct a height map of the sample. Figure 6.3d displays a height map of the test target that has been retrieved in this way, clearly showing the 100 nm thick Chromium lines deposited on a glass substrate. The phase retrieval algorithm already provides a height resolution of ~ 20 nm in this case, which can be increased further by improving the signal-to-noise ratio in the measurement. In the present sample, a small reflection from the sample back surface was also present, resulting in an additional image that appears negative and shifted. Interference between these two surface images has some influence on the reconstructed phase, which would not be the case for a pure single surface reflection. Note that this is a measurement of optical path length, so that the refractive index of an immersion liquid or

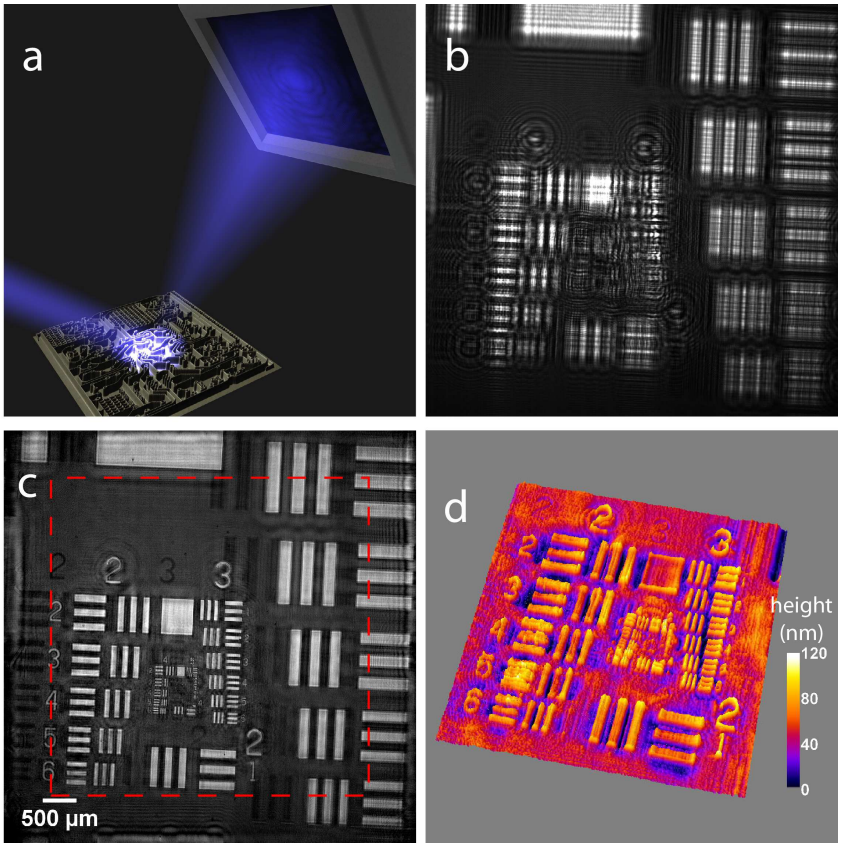

FIGURE 6.3: (a) Lensless imaging in a reflection geometry. (b) Quasi-monochromatic Fresnel diffraction pattern of a 1951 USAF test target, recorded in a reflection geometry and obtained through a two-pulse Fourier-transform scan. (c) Resulting image after 25 iterations of the multi-wavelength iterative phase retrieval, using diffraction patterns at 5 different wavelengths. Some negative (dark) features are also observed, which are due to reflections from the sample back surface. The dashed red line marks the area in which all wavelengths contribute to the reconstruction. (d) Reconstructed height map from part of the USAF target surface from b, showing the chrome structures on the glass substrate.

phase shifts due to partial reflection should be taken into account when calculating the geometrical height from the retrieved phase.

6.4 Ultra-broadband extreme ultraviolet imaging

To demonstrate that our two-pulse imaging approach extends to shorter wavelengths, we perform an imaging experiment with a HHG source. A schematic of the setup is shown in Fig. 6.4a: the pulse pair is produced in the near infrared with a split-wavefront interferometer before the HHG setup, using quartz wedges to scan the time delay. This particular interferometer implementation is highly stable: it is nearly common path, and there are no mirrors in the setup that only reflect one of the pulses. These properties eliminate most of the noise caused by vibrations, air flow and acoustics present in conventional Michelson interferometers. We used a 1° wedge for scanning the delay, mounted on a closed-loop piezo-stage with 5 nm resolution and 500 μm scan range. A 100 nm movement of the stage resulted in a 1.32 nm optical path length difference between the pulses, enabling scans with sub-nm step size. A single wedge in the other interferometer arm introduces an angle between the beams. The lens (focal length F), that focuses the pulses into the HHG gas cell, is placed at a distance F behind the point where the beams cross. This geometry ensures that the two beams run parallel to each other behind the lens. Both beams focus near the end of the gas cell with a small transverse separation between the focal spots. In this manner, ionization due to the first pulse does not influence the HHG process for the second (time-delayed) pulse, allowing linear Fourier-transform scans at HHG frequencies [109]. The HHG pulses overlap spatially at the imaging target due to their beam divergence. The focal length F is 350 mm, and the focal spot diameter is 40 μm FWHM. Harmonics are produced in xenon gas at $\sim$50 mbar pressure in the gas cell, with an energy of 0.2 mJ in each 40 fs duration pulse. Behind the cell, a differential pumping stage is used to prevent re-absorption of the produced HHG. Scanning the time delay was performed by moving a wedge into one half of the beam, enabling scans with sub-nm position accuracy.

We use the full HHG flux directly to image a nickel grid, with 20 μm wide bars, attached to a 300 nm thick aluminium foil. The Al foil reflects the fundamental beam, while transmitting radiation below 80 nm wavelength. In this experiment, the nickel grid is placed at 40 cm behind

the focus. The diffracted light is detected in a transmission geometry using an XUV-sensitive CCD camera (Andor Technology) with 1024x1024 pixels, a pixel size of 13 μm, and a bit depth of 12 bits. This camera is placed 0.6 m behind the sample. In a typical Fourier-transform scan, 512 diffraction images are recorded as a function of time delay. Between consecutive images, the time interval is increased in steps of 44 attoseconds (corresponding to a physical step size of 13.2 nm). At each time step, 5 frames are recorded with 0.3 second exposure time and averaged to improve the signal-to-noise ratio.

Figure 6.4b displays a broadband diffraction pattern of the nickel grid recorded with the transmitted HHG spectrum. Figure 6.4c shows the HHG spectrum used in these imaging experiments, which is obtained from the two-pulse scan itself. Three harmonics are present, spanning a wavelength range between 47 and 63 nm. Lower harmonics are not transmitted by the Al foil and the xenon gas, while the HHG phase-matching cut-off is near harmonic 17. For the HHG phase retrieval we use images at harmonics 13, 15 and 17 (center wavelengths 62 nm, 53 nm and 47 nm, respectively) as input for the multi-wavelength phase retrieval algorithm. At each harmonic, we filter out a spectral bandwidth of 1.5 nm, which suffices to achieve diffraction-limited resolution in this experiment. Typically, only 10 iterations of the algorithm are required for stable convergence.

Due to the transverse displacement between the two HHG pulses, the recorded data contain two displaced copies of the object's diffraction pattern. This can be accounted for by incorporating an additional deconvolution step in the image reconstruction procedure, since the image at each wavelength can be interpreted as the convolution between a single diffraction pattern of the object and a pair of Dirac delta functions. The distance between these Dirac delta functions is calculated from the imaging geometry and the initial separation between the focal spots in the gas cell. The single diffraction patterns can then be retrieved from the spectrally resolved images by deconvolution. Subsequently, the resulting diffraction patterns can be used in the multi-wavelength phase retrieval algorithm. Small angular deviations between the two beams can also be handled, enabling two-pulse imaging even with non-collinear beams from a split-wavefront interferometer [110, 111].

The resulting reconstructed image of the Ni grid is shown in Figs. 6.4d and 6.4e. To quantify the achieved image resolution, the image intensity across one of the nickel bars is plotted in Fig. 6.4f. This cross-section is compared to a simulation of the known shape of the bar

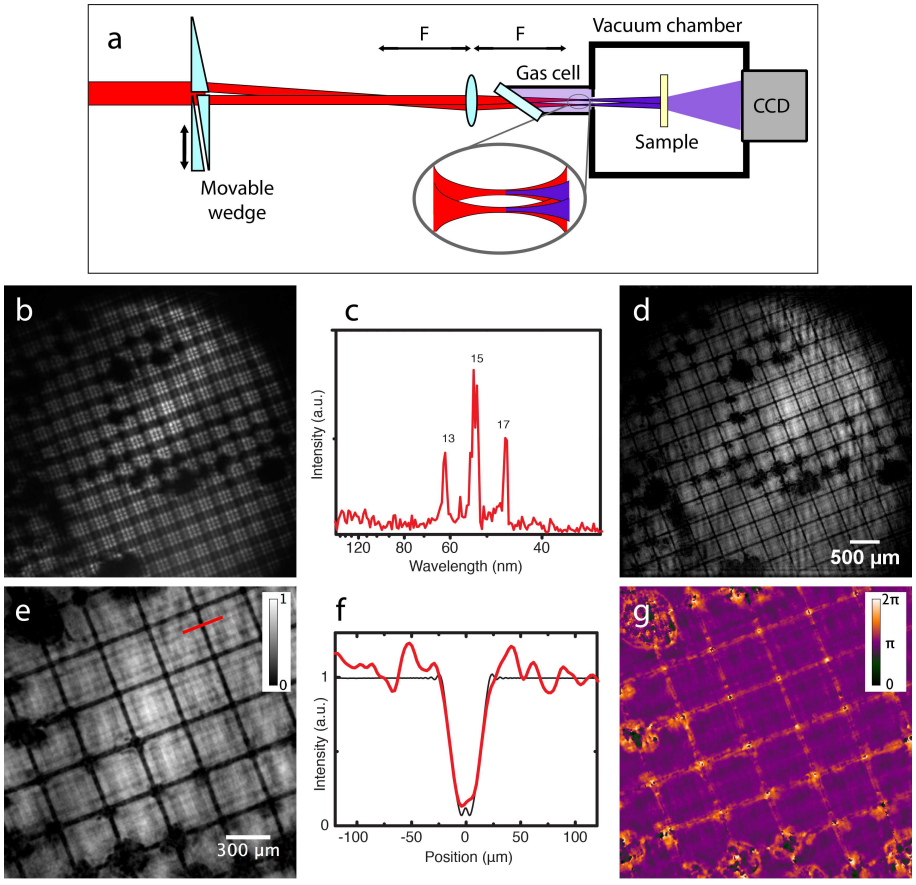

Figure 6.4: Lensless imaging with ultra-broadband extreme-ultraviolet radiation. (a) Schematic of the setup for two-pulse imaging with high-harmonic radiation. A variable time delay is introduced by inserting a wedge into the beam (note that this drawing is only for schematic purposes: the actual orientation of the wedges is rotated by 90 degrees with respect to this drawing). (b) Broadband diffraction pattern of a nickel grid on a 300 nm thick Al foil, recorded using harmonics 13, 15 and 17. (c) Spectrum extracted from the two-pulse Fourier-transform scan. (d) Retrieved image of the Ni grid at 47 nm wavelength, using the multi-wavelength phase retrieval algorithm. The regular features of the grid are clearly visible, along with several damage spots induced by intense laser irradiation in earlier experiments. (e) Enlarged view of part of the image in d, showing the 20 μm wide grid lines. (f) Cross-section of the intensity along the red bar in e (red trace), together with a simulated curve of a square bar convolved with the expected diffraction limited point-spread function (black trace). (g) Phase image of the grid retrieved by the multi-wavelength phase retrieval algorithm.

convolved with a sinc-shaped point-spread function corresponding to the diffraction-limited half-pitch resolution of 6.7 μm. A good agreement is obtained, from which we deduce that the retrieved image resolution is near the diffraction limit for the used sample-camera distance. A small artefact from imperfect deconvolution can be seen in the form of a shadow image (with an intensity of a few percent) on both sides of the main image. Furthermore, some subtle vertical interference fringes are observed in the reconstructed image in Fig. 6.4d, mainly at the right edge of the beam. These are likely caused by imperfections in the incident XUV wavefront. In addition to the regular Ni grid, several dark damage spots are observed, which were caused in earlier experiments with intense laser pulses that partially melted the nickel structures. In addition to the reconstructed intensity image, the retrieved phase profile at 47 nm wavelength is shown in Fig. 6.4g. A relatively constant phase is obtained for the gaps in between the nickel bars, while the phase at the position of the bars shows large phase variations. This observation is explained by the negligible light intensities at the location of the bars, which are 5 μm thick and do not transmit the XUV radiation. Therefore, the phase at these positions is undefined. While the diffraction limit in the current proof-of-concept experiment was relatively low due to geometrical constraints, a much higher resolution can readily be achieved in Fresnel diffractive imaging by illuminating the sample with a curved wavefront [87, 103], which is fully compatible with our two-pulse imaging approach.

6.5 Conclusions

In summary, we have presented two-pulse imaging as a method that enables lensless microscopy with ultra-broadband light sources. The full spectrum is efficiently used for imaging, making this approach well suited for XUV imaging with compact, low-flux, broadband sources such as table-top HHG systems. In addition, we have introduced a new approach for robust phase retrieval for lensless imaging in the Fresnel regime, based on the use of diffraction patterns at multiple wavelengths in an iterative phase retrieval scheme. This method provides stable and rapid convergence even for complex samples, and does not require any support constraints or localized illumination. This multi-wavelength phase retrieval approach can readily be used with the spectrally resolved data obtained with two-pulse imaging, and we have demonstrated its use in

both transmission and reflection. We find that two-pulse imaging enables robust and accurate lensless imaging with broadband and unstable spectra, without a priori knowledge of the spectrum for image reconstruction. This is a situation often encountered with HHG sources, where efficient use of the available photon flux is essential for practical imaging applications. We have performed numerical simulations to study the influence of intensity and timing variations in more detail (section 6.6 and Fig. 6.8), which indicate that good-quality images can be obtained even in the presence of significant noise. From our measurements, we find a pulse delay stability of 8 nm without active stabilisation (section 6.6 and Fig. 6.7), which is sufficient for imaging at wavelengths down to 16 nm. With additional stabilization measures [112], an extension to the soft-X-ray domain should be feasible. We therefore foresee that two-pulse imaging will find widespread application in the development of compact table-top HHG-based microscopes, thus providing new possibilities for e.g. structural biology and nanotechnology by enabling label-free ultrahigh-resolution microscopy in a laboratory-scale environment.

6.6 Supplementary information

6.6.1 Fourier-transform spectroscopy and two-pulse imaging

An essential ingredient in two-pulse imaging is the concept of Fourier-transform spectroscopy, in which a spectrum is recorded through a time-domain measurement rather than a spectrometer. In Fourier-transform spectroscopy, a light pulse is split in two replicas with an identical spectrum $A(\omega)$. Giving one of the replicas a time delay τ results in a frequency-dependent phase difference $\phi(\omega) = \omega\tau$. When the spectrum of the pulse pair is measured for a constant time delay, this results in spectral interference:

$$I(\omega) = |A(\omega)(1 + e^{-i\omega t})|^2 = 2|A(\omega)|^2(1 + \cos(\omega\tau)) \tag{6.2}$$

Inversely, when the total intensity is measured as a function of time delay, what is recorded is:

$$I(\tau) = 2\int_0^\infty |A(\omega)|^2(1 + \cos(\omega\tau))\,\mathrm{d}\omega \tag{6.3}$$

which can be identified as the Fourier cosine transform of the spectral intensity (plus a DC offset). The diffraction pattern of an object illumi-

nated by a broadband light source can be viewed as a linear superposition of monochromatic diffraction patterns produced by all the spectral components in the source spectrum. As the angle at which light is diffracted by a finite object is intrinsically wavelength-dependent, the information about a specific k-vector will be located at a different point for each wavelength in the resulting broadband diffraction pattern. In a broadband diffraction pattern, the measured intensity at each pixel will therefore be an unknown superposition of the source spectral components. To reconstruct sharp, monochromatic diffraction patterns, the spectrum of the diffracted light at each camera pixel needs to be retrieved. From the above discussion, a possible way to identify the spectral content of each pixel is by Fourier-transform spectroscopy. By splitting the incident pulse in two replicas with a controlled time delay, we can introduce an identical frequency-dependent phase shift into the spectrum at all camera pixels. By scanning the time delay and recording a series of images as a function of τ, we essentially perform Fourier-transform spectroscopy in a massively parallel way, recording the Fourier transform of the spectrum at all pixels simultaneously. This approach is schematically depicted for a 1D-case in Fig. 6.5. By Fourier-transforming the measured time-delay scan for each pixel, we directly obtain the spectrum of the light scattered onto that pixel. We can then decompose the initial broadband superposition into a set of monochromatic diffraction patterns.

In the simulations below (Fig. 6.8), we show that in practice a significant amount of spectral fluctuations between the pulses can be tolerated. Furthermore, as the measurement is linear, any difference in dispersion between the pulses does not influence the measured spectrum: only the relative phase between the Fourier components is changed, which does not affect the measured spectral intensity.

6.6.2 Interferometer stability measurements

To assess the stability of our interferometer, we use the data from our two pulse scan itself. We record 5 images consecutively at each time delay, and we compare these images to obtain an estimate of the path length fluctuations between the two pulses. Due to the non-collinear geometry of our experiment, the individual images contain spatial interference fringes. We isolate this interference pattern by a 2D spatial Fourier transformation, filtering the spatial frequency corresponding to this interference pattern, and inverse transformation. We can then extract the phase of the interference at a single pixel.

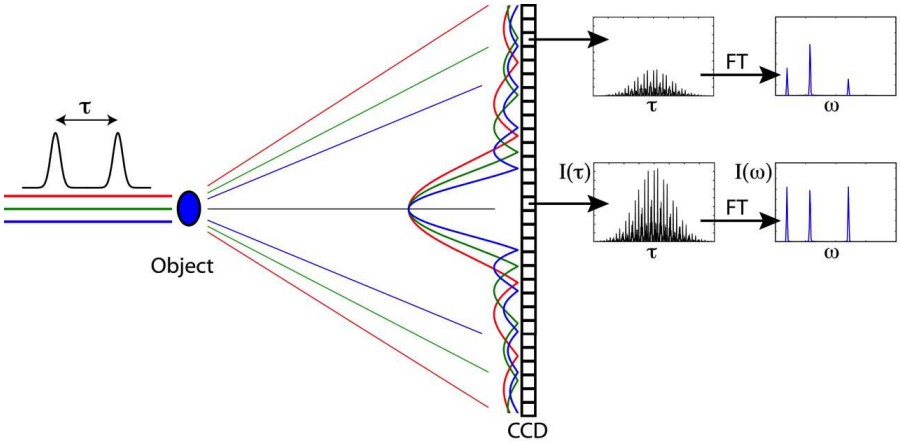

Figure 6.5: Schematic principle of the use of Fourier-transform spectroscopy for retrieving the diffracted spectrum at all CCD pixels. By scanning the time delay ÏĎ between the pulses, an interferogram is recorded at each pixel, from which the spectrum can be recovered through a Fourier transform (FT).

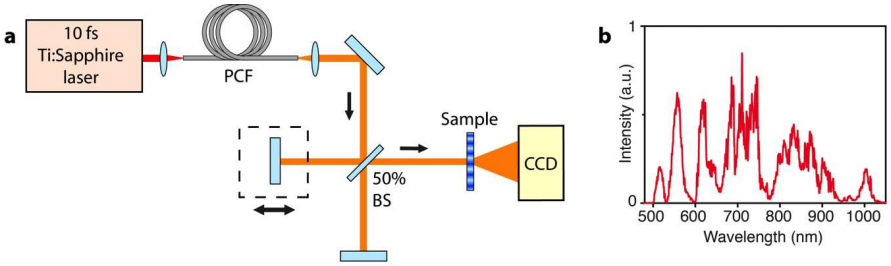

Figure 6.6: Setup for lensless two-pulse imaging. (a) White-light continuum pulses are produced by launching 10 fs, 2.5 nJ pulses from a modelocked Ti:Sapphire laser, running at 80 MHz repetition rate, into a photonic crystal fibre (PCF) with a 2.3 μm core diameter. Supercontinuum generation in the fibre produces a highly structured white light continuum that spans an optical octave, as shown in (b). A pulse pair with variable time delay is produced by a Michelson interferometer, with one of the end mirrors mounted on a closed-loop piezo-driven translation stage.

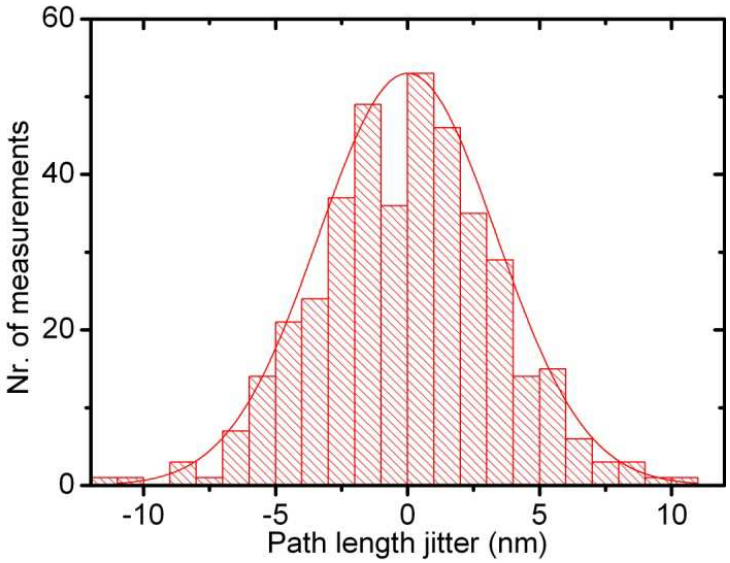

FIGURE 6.7: Measurement of the path length fluctuations during a scan. Histogram of the phase deviations observed during a two-pulse imaging experiment. The width of the Gaussian distribution is 7.9 nm FWHM. See text for details.

An estimate for the path length jitter is obtained by calculating the average phase of each group of 5 measurements at a fixed position, and then calculating the difference of the phase of each individual measurement with this average. Since a 2π phase shift corresponds to a path length change of one average wavelength, this phase shift is a direct measure of the path length fluctuations.

Performing such an analysis on an entire two-pulse imaging dataset provides a histogram of the path length fluctuations during the scan, of which an example is given in Fig. 6.7. From this data, we find that the path length fluctuations in our scan follow a Gaussian distribution with a FWHM width of 8 nm. We have repeated this analysis on multiple datasets, yielding identical results. From this analysis and the results of our numerical simulations (see text below) we conclude that imaging with wavelengths down to 16 nm should already be possible with the level of stability of our current setup. With further stabilization measures, such as active feedback and placing the interferometer in vacuum, these fluctuations can be reduced to the nm level, enabling two-pulse imaging in the water-window spectral range.

6.6.3 Multi-wavelength Fresnel image reconstruction procedure

For our multi-wavelength Fresnel reconstruction method, phase retrieval is performed in a Gerchberg-Saxton type iterative scheme [51, 86], where the intensity data from the first wavelength is propagated to the next wavelength using the Fresnel propagation equation (6.1). After propagation, the phase information is retained, while the intensity is replaced by the measured intensity at this new wavelength.

The algorithm itself works as follows. Spectrally resolved images are obtained from a two-pulse scan by loading the full (x,y,t)-dataset into a 3D array and performing a 1D-FFT as a function of time delay for each individual camera (x,y)-pixel. This directly yields a (x,y,f)-dataset, where each spatial 2D image is now a spectrally resolved diffraction pattern at frequency $f = c/\lambda$, with a spectral resolution of $1/T$. Each of these diffraction patterns can then be further processed with the algorithms available for lensless image reconstruction. The spectral resolution $\Delta\lambda$ of the individual reconstructed images is only limited by the total scanned time delay T, and can be expressed as $\Delta\lambda/\lambda = \lambda/(ct)$, where c is the speed of light and λ is the wavelength of the light. Similar to Fourier-transform spectroscopy, the maximum step size between images is limited to $\lambda/2$ by the Nyquist sampling criterion.

6.6.4 Two-pulse imaging in the presence of noise: simulations

In Fourier-transform spectroscopy, the signal at any frequency component is encoded as a sinusoidal signal with a constant oscillation period in the time-delay scan. Therefore, only temporal intensity fluctuations with a frequency that matches this signal oscillation will add noise to the image at this particular frequency component.

To investigate the amount of temporal intensity fluctuations that can be tolerated, we performed numerical simulations of our two-pulse scans at realistic experimental parameters, but with various types of noise added to either one or both pulses. We then performed our multi-wavelength phase-retrieval procedure, to assess the influence of specific types of noise on the quality of the final reconstructed image. Fig. 6.8 shows the results of these simulations. We used a typical image of part of a resolution test target as the input object, and calculated diffraction patterns at 0.25 meter propagation distance, with an octave-wide input

spectrum between 2.25 and 4.5 PHz (67 - 133 nm wavelength range). The red box in Fig. 6.8 shows the input spectrum, input object, and a typical calculated diffraction pattern at 133 nm wavelength.

We simulated two-pulse scans for several cases: 1) perfectly stable pulses, 2) certain amounts of timing jitter between the pulses, 3) spectral intensity fluctuations in both pulses simultaneously, and 4) spectral intensity fluctuations in only one of the pulses. In each case, 512 steps with 20 nm step size (66.7 attoseconds) are taken, symmetrically around zero time delay. For each situation, we plot the resulting temporal interference at a single pixel (from the top bright part of the '4' in the diffraction pattern), the retrieved spectrum averaged over the full spectrally resolved dataset after the Fourier transformation step, and the final image of the object retrieved by multi-wavelength phase retrieval (using 3 diffraction patterns at wavelengths of 126.7 nm, 92.1 nm and 69.9 nm as input data).

For the case of stable pulses, the time delay scan shows a clean interference pattern, the source spectrum is retrieved with good quality (aside from smoothed edges due to the finite spectral resolution), and the reconstructed image of the object is of high quality.

Next, we simulated a scan in which introduced a random timing error to each scan step, taken from a Gaussian distribution with a FWHM of 50 attoseconds (15 nm path length). Such a timing jitter corresponds to nearly a quarter cycle of the shortest wavelength in the source spectrum. While the time delay scan still looks good, a significant amount of white noise is introduced onto the retrieved spectrum. Nevertheless, the shape of the spectrum is retrieved correctly, and the reconstructed image seems to suffer only a minor contrast decrease. Increasing this timing jitter to 100 attoseconds (30 nm path length) results in more severe errors. The noise level on the spectrum has increased to the level of the signal. As a result, the reconstructed image also shows a significant background noise, although a faithful reconstruction of the object is still obtained. This is quite remarkable, since this timing jitter corresponds to nearly half a cycle of the shortest wavelength in the spectrum.

To simulate spectral intensity jitter, we divided the spectrum into 50 components. At each scan step, we gave each individual component a random intensity between 50 and 100%. This would simulate a situation where a single fluctuating pulse is split in two for the measurement. The reconstructed spectrum is as expected, and the retrieved image of the object is of high quality. To study the situation where two pulses experience independent fluctuations (as could be the case for HHG with

separated generation zones), we simulated a scan with such spectral intensity fluctuations in only one of the pulses. Again in this case, both the retrieved spectrum and reconstructed image are good representations of the input parameters. It should be stressed that the simulated intensity fluctuations are excessive even for HHG sources, and can easily be minimized by averaging over multiple laser pulses at each scan step. The simulated timing variations are also significantly larger than experimentally observed. The exact influence of the noise on the contrast and resolution of the retrieved image depends on the object under investigation, and is therefore difficult to quantify. Yet the two-pulse imaging approach is found to be remarkably robust, and results in a faithful reconstruction of the object even in the presence of significant noise sources. This gives confidence that the method can be scaled to significantly shorter wavelengths than presented in the current work.

6.6.5 Multi-wavelength phase retrieval: practical implementation

In this section we provide a detailed description of the multi-wavelength phase retrieval algorithm. The required input data is a set of diffraction intensity patterns at different wavelengths. The distance between the sample and the camera should also be known, and is typically measured beforehand or determined from a single-step back-propagation of a diffraction pattern. Fresnel propagation of an image over a distance z is calculated by 2D Fast Fourier Transform (FFT), multiplication with a propagation transfer function for free space, and subsequent 2D inverse FFT. This propagation transfer function is given by [22]:

$$H(f_x, f_y, \lambda_n) = e^{i2\pi z\sqrt{\frac{1}{\lambda_n^2} - f_x^2 - f_y^2}} \tag{6.4}$$

The phase retrieval algorithm then works along the following steps:

1. Fresnel propagation of the image at wavelength λ_n to the object plane using $H(f_x, f_y, \lambda_n)$.

2. At the object plane, divide the phase of the field by the wavelength ratio λ_{n+1}/λ_n.

3. Propagate to the field back to the detector plane using the conjugate propagation transfer function $H(f_x, f_y, \lambda_{n+1})$ for the next wavelength λ_{n+1}.

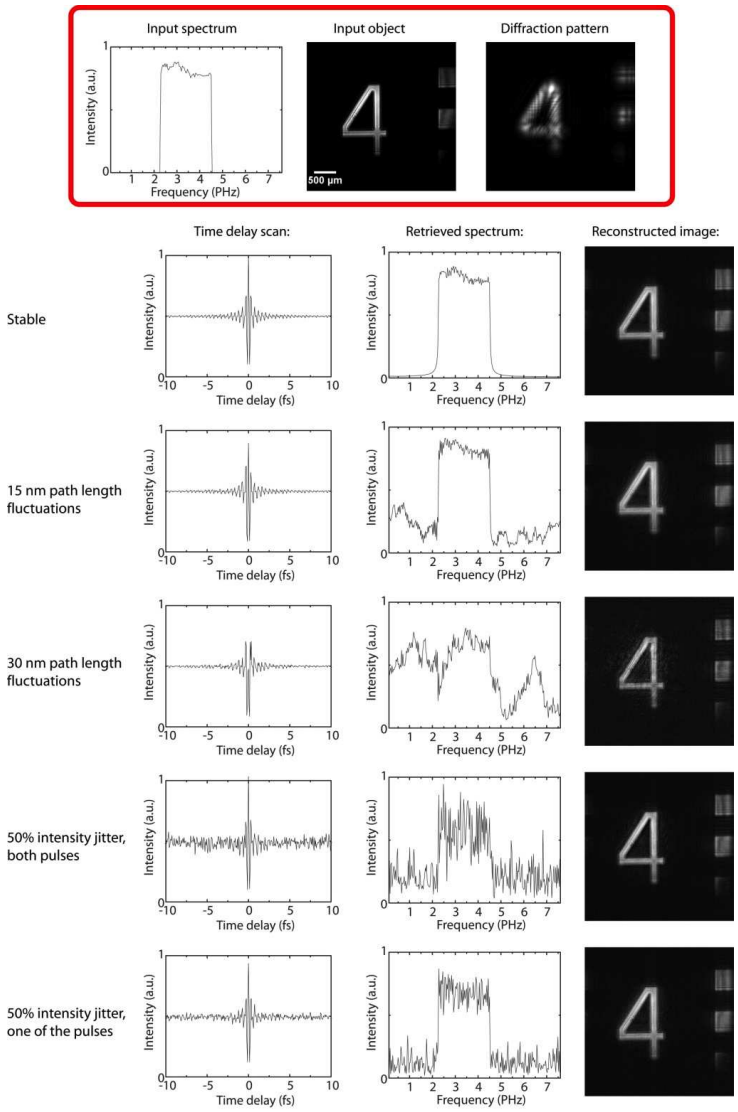

FIGURE 6.8: Effects of different types of noise on the two-pulse scan and the resulting image reconstruction. The input spectrum and image object are displayed in the red box at the top, along with a simulated diffraction pattern at one wavelength. In the respective rows, five different simulation results are shown. For each simulation, the left column displays the intensity at a single pixel as a function of pulse-to-pulse time delay, the middle column displays the spectral intensity after Fourier transformation, and the right column shows the reconstructed image from the multi-wavelength phase retrieval algorithm. See text for details.

4. At the detector plane, replace the resulting amplitude by the measured amplitude at λ_{n+1}, while retaining the phase.

5. Repeat steps 1 - 4 for the subsequent wavelengths, and propagate from the final wavelength back to λ_1. This completes one iteration.

6. Perform multiple iterations while checking for convergence of the algorithm.

7. Perform a single final Fresnel propagation step to the object plane to obtain the retrieved amplitude and phase of the field at the position of the object.

The resulting retrieved field is the product of the incident light field and the complex object transmission function. If the light field is known (e.g. by a measurement without a sample in place), the complex object transmission function can be retrieved as well.

Bibliography

[1] R. P. Feynman, "There's Plenty of Room at the Bottom," feb 1960.

[2] A. I. Carswell and C. Richard, "Resolving Power of Focusing Systems with Coherent Illumination," *Applied Optics*, 1965.

[3] S. W. Hell and J. Wichmann, "Breaking the diffraction resolution limit by stimulated emission: stimulated-emission-depletion fluorescence microscopy," *Optics letters*, 1994.

[4] E. Betzig and J. K. Trautman, "Near-field optics: microscopy, spectroscopy, and surface modification beyond the diffraction limit," *Science*, 1992.

[5] B. L. Henke, E. M. Gullikson, and J. C. Davis, "X-Ray Interactions: Photoabsorption, Scattering, Transmission, and Reflection at E = 50-30,000 eV, Z = 1-92," *Atomic Data and Nuclear Data Tables*, vol. 54, pp. 181–342, jul 1993.

[6] C. A. Larabell and M. A. Le Gros, "X-ray tomography generates 3-D reconstructions of the yeast, saccharomyces cerevisiae, at 60-nm resolution," *Molecular biology of the cell*, vol. 15, pp. 957–62, mar 2004.

[7] W. Chao, B. D. Harteneck, J. A. Liddle, E. H. Anderson, and D. T. Attwood, "Soft X-ray microscopy at a spatial resolution better than 15 nm," *Nature*, vol. 435, pp. 1210–3, jun 2005.

[8] H. N. Chapman, P. Fromme, A. Barty, T. A. White, R. A. Kirian, A. Aquila, M. S. Hunter, J. Schulz, D. P. DePonte, U. Weierstall, R. B. Doak, F. R. N. C. Maia, A. V. Martin, I. Schlichting, L. Lomb, N. Coppola, R. L. Shoeman, S. W. Epp, R. Hartmann, D. Rolles, A. Rudenko, L. Foucar, N. Kimmel, G. Weidenspointner, P. Holl, M. Liang, M. Barthelmess, C. Caleman, S. Boutet, M. J. Bogan, J. Krzywinski, C. Bostedt, S. Bajt, L. Gumprecht, B. Rudek, B. Erk, C. Schmidt, A. Hömke, C. Reich, D. Pietschner, L. Strüder, G. Hauser, H. Gorke, J. Ullrich, S. Herrmann, G. Schaller, F. Schopper, H. Soltau, K.-U. Kühnel, M. Messerschmidt, J. D. Bozek, S. P. Hau-Riege, M. Frank, C. Y. Hampton,

R. G. Sierra, D. Starodub, G. J. Williams, J. Hajdu, N. Timneanu, M. M. Seibert, J. Andreasson, A. Rocker, O. Jönsson, M. Svenda, S. Stern, K. Nass, R. Andritschke, C.-D. Schröter, F. Krasniqi, M. Bott, K. E. Schmidt, X. Wang, I. Grotjohann, J. M. Holton, T. R. M. Barends, R. Neutze, S. Marchesini, R. Fromme, S. Schorb, D. Rupp, M. Adolph, T. Gorkhover, I. Andersson, H. Hirsemann, G. Potdevin, H. Graafsma, B. Nilsson, and J. C. H. Spence, "Femtosecond X-ray protein nanocrystallography," *Nature*, vol. 470, pp. 73–7, feb 2011.

[9] R. Erni, M. Rossell, C. Kisielowski, and U. Dahmen, "Atomic-Resolution Imaging with a Sub-50-pm Electron Probe," *Physical Review Letters*, vol. 102, p. 096101, mar 2009.

[10] E. Cuche, F. Bevilacqua, and C. Depeursinge, "Digital holography for quantitative phase-contrast imaging," *Optics Letters*, vol. 24, p. 291, mar 1999.

[11] H. Faulkner and J. Rodenburg, "Movable aperture lensless transmission microscopy: a novel phase retrieval algorithm," *Physical review letters*, 2004.

[12] P. Corkum, "Plasma perspective on strong field multiphoton ionization," *Physical Review Letters*, vol. 71, pp. 1994–1997, sep 1993.

[13] W. Koechner, *Solid-state Laser Engineering*. 2006.

[14] Y. Chu, X. Liang, L. Yu, Y. Xu, L. Xu, L. Ma, X. Lu, Y. Liu, Y. Leng, R. Li, and Z. Xu, "High-contrast 2.0 Petawatt Ti:sapphire laser system," *Optics express*, vol. 21, pp. 29231–9, dec 2013.

[15] J. Zhou, C.-P. Huang, C. Shi, M. M. Murnane, and H. C. Kapteyn, "Generation of 21-fs millijoule-energy pulses by use of Ti:sapphire," *Optics Letters*, vol. 19, p. 126, jan 1994.

[16] S. A. Akhmanov, A. I. Kovrigin, and A. S. Piskarskas, "Observation of parametric amplification in the optical range," *Jetp Lett*, 1965.

[17] G. Cerullo and S. De Silvestri, "Ultrafast optical parametric amplifiers," *Review of Scientific Instruments*, vol. 74, p. 1, jan 2003.

[18] T. Gureyev, S. Mayo, S. Wilkins, D. Paganin, and A. Stevenson, "Quantitative In-Line Phase-Contrast Imaging with Multienergy X

Rays," *Physical Review Letters*, vol. 86, pp. 5827–5830, jun 2001.

[19] M. A. Harthcock and S. C. Atkin, "Imaging with Functional Group Maps Using Infrared Microspectroscopy," *Appl. Spectrosc.*, vol. 42, no. 3, pp. 449–455, 1988.

[20] D. W. E. Noom, D. E. Boonzajer Flaes, E. Labordus, K. S. E. Eikema, and S. Witte, "High-speed multi-wavelength Fresnel diffraction imaging," *Optics Express*, vol. 22, p. 30504, dec 2014.

[21] P. C. D. Hobbs, *Building Electro-Optical Systems: Making It all Work*. 2009.

[22] J. Goodman, "Introduction to Fourier optics," *Introduction to Fourier optics*, 2005.

[23] J. R. Fienup, "Phase retrieval algorithms: a comparison," *Applied optics*, vol. 21, pp. 2758–69, aug 1982.

[24] S. Marchesini, "Invited article: A unified evaluation of iterative projection algorithms for phase retrieval," *Review of Scientific Instruments*, 2007.

[25] L. E. Hargrove, R. L. Fork, and M. A. Pollack, "LOCKING OF He-Ne LASER MODES INDUCED BY SYNCHRONOUS INTRACAVITY MODULATION," *Applied Physics Letters*, vol. 5, p. 4, nov 1964.

[26] M. E. Fermann, "Passive mode locking by using nonlinear polarization evolution in a polarization-maintaining erbium-doped fiber," *Optics Letters*, vol. 18, p. 894, jun 1993.

[27] B. K. Garside, "Laser mode locking using saturable absorbers," *Journal of Applied Physics*, vol. 44, p. 2335, oct 1973.

[28] D. E. Spence, P. N. Kean, and W. Sibbett, "60-fsec pulse generation from a self-mode-locked Ti:sapphire laser," *Optics Letters*, vol. 16, p. 42, jan 1991.

[29] U. Keller and K. J. Weingarten, "Semiconductor saturable absorber mirrors (SESAM's) for femtosecond to nanosecond pulse generation in solid-state lasers," *IEEE Journal of Selected Topics in Quantum Electronics*, 1996.

[30] S. Witte and K. S. E. Eikema, "Ultrafast Optical Parametric Chirped-Pulse Amplification," *IEEE Journal of Selected Topics in*

Quantum Electronics, vol. 18, pp. 296–307, jan 2012.

[31] R. Paschotta, *Encyclopedia of laser physics and technology*. 2008.

[32] M. D. Skeldon and S. T. Bui, "Temporal mode structure of a regenerative amplifier with intracavity étalons," *Journal of the Optical Society of America B*, vol. 10, p. 677, apr 1993.

[33] J. Giordmaine, "Mixing of Light Beams in Crystals," *Physical Review Letters*, vol. 8, pp. 19–20, jan 1962.

[34] E. Riedle, M. Beutter, S. Lochbrunner, J. Piel, S. Schenkl, S. Spörlein, and W. Zinth, "Generation of 10 to 50 fs pulses tunable through all of the visible and the NIR," *Applied Physics B*, vol. 71, pp. 457–465, feb 2000.

[35] E. A. Gibson, A. Paul, N. Wagner, R. Tobey, D. Gaudiosi, S. Backus, I. P. Christov, A. Aquila, E. M. Gullikson, D. T. Attwood, M. M. Murnane, and H. C. Kapteyn, "Coherent soft x-ray generation in the water window with quasi-phase matching," *Science*, vol. 302, pp. 95–8, oct 2003.

[36] X. F. Li, A. L'Huillier, M. Ferray, L. A. Lompré, and G. Mainfray, "Multiple-harmonic generation in rare gases at high laser intensity," *Physical Review A*, vol. 39, pp. 5751–5761, jun 1989.

[37] J. L. Krause, K. J. Schafer, and K. C. Kulander, "High-order harmonic generation from atoms and ions in the high intensity regime," *Physical Review Letters*, vol. 68, pp. 3535–3538, jun 1992.

[38] M. Lewenstein, P. Balcou, M. Y. Ivanov, A. L'Huillier, and P. B. Corkum, "Theory of high-harmonic generation by low-frequency laser fields," *Physical Review A*, vol. 49, pp. 2117–2132, mar 1994.

[39] A. D. Shiner, C. Trallero-Herrero, N. Kajumba, H.-C. Bandulet, D. Comtois, F. Légaré, M. Giguère, J.-C. Kieffer, P. B. Corkum, and D. M. Villeneuve, "Wavelength Scaling of High Harmonic Generation Efficiency," *Physical Review Letters*, vol. 103, p. 073902, aug 2009.

[40] M.-C. Chen, P. Arpin, T. Popmintchev, M. Gerrity, B. Zhang, M. Seaberg, D. Popmintchev, M. M. Murnane, and H. C. Kapteyn, "Bright, Coherent, Ultrafast Soft X-Ray Harmonics Spanning the Water Window from a Tabletop Light Source," *Physical Review*

Letters, vol. 105, p. 173901, oct 2010.

[41] T. Popmintchev, M.-C. Chen, A. Bahabad, M. Gerrity, P. Sidorenko, O. Cohen, I. P. Christov, M. M. Murnane, and H. C. Kapteyn, "Phase matching of high harmonic generation in the soft and hard X-ray regions of the spectrum," *Proceedings of the National Academy of Sciences of the United States of America*, vol. 106, pp. 10516–21, jun 2009.

[42] E. Constant, D. Garzella, P. Breger, E. Mével, C. Dorrer, C. Le Blanc, F. Salin, and P. Agostini, "Optimizing High Harmonic Generation in Absorbing Gases: Model and Experiment," *Physical Review Letters*, vol. 82, pp. 1668–1671, feb 1999.

[43] T. Popmintchev, M.-C. Chen, P. Arpin, M. M. Murnane, and H. C. Kapteyn, "The attosecond nonlinear optics of bright coherent X-ray generation," *Nature Photonics*, vol. 4, pp. 822–832, dec 2010.

[44] D. W. E. Noom, K. S. E. Eikema, and S. Witte, "Lensless phase contrast microscopy based on multiwavelength Fresnel diffraction," *Optics letters*, vol. 39, pp. 193–6, jan 2014.

[45] W. Denk, J. Strickler, and W. Webb, "Two-photon laser scanning fluorescence microscopy," *Science*, vol. 248, pp. 73–76, apr 1990.

[46] S. W. Hell, "Far-field optical nanoscopy," *Science*, vol. 316, pp. 1153–8, may 2007.

[47] P. Kner, B. B. Chhun, E. R. Griffis, L. Winoto, and M. G. L. Gustafsson, "Super-resolution video microscopy of live cells by structured illumination," *Nature methods*, vol. 6, pp. 339–42, may 2009.

[48] G. Zheng, S. A. Lee, Y. Antebi, M. B. Elowitz, and C. Yang, "The ePetri dish, an on-chip cell imaging platform based on subpixel perspective sweeping microscopy (SPSM)," *Proceedings of the National Academy of Sciences of the United States of America*, vol. 108, pp. 16889–94, oct 2011.

[49] W. Xu, M. H. Jericho, I. A. Meinertzhagen, and H. J. Kreuzer, "Digital in-line holography for biological applications," *Proceedings of the National Academy of Sciences of the United States of America*, vol. 98, pp. 11301–5, sep 2001.

[50] W. Bishara, T.-W. Su, A. F. Coskun, and A. Ozcan, "Lensfree

on-chip microscopy over a wide field-of-view using pixel super-resolution," *Optics express*, vol. 18, pp. 11181–91, may 2010.

[51] J. R. Fienup, "Reconstruction of a complex-valued object from the modulus of its Fourier transform using a support constraint," *Journal of the Optical Society of America A*, vol. 4, p. 118, jan 1987.

[52] Y. M. Bruck and L. G. Sodin, "On the ambiguity of the image reconstruction problem," *Optics Communications*, 1979.

[53] L. J. Allen and M. P. Oxley, "Phase retrieval from series of images obtained by defocus variation," *Optics Communications*, vol. 199, pp. 65–75, nov 2001.

[54] Y. Zhang, G. Pedrini, W. Osten, and H. Tiziani, "Whole optical wave field reconstruction from double or multi in-line holograms by phase retrieval algorithm," *Optics Express*, vol. 11, p. 3234, dec 2003.

[55] A. Greenbaum, W. Luo, T.-W. Su, Z. Göröcs, L. Xue, S. O. Isikman, A. F. Coskun, O. Mudanyali, and A. Ozcan, "Imaging without lenses: achievements and remaining challenges of wide-field on-chip microscopy," *Nature methods*, vol. 9, pp. 889–95, sep 2012.

[56] J. Rodenburg, A. Hurst, A. Cullis, B. Dobson, F. Pfeiffer, O. Bunk, C. David, K. Jefimovs, and I. Johnson, "Hard-X-Ray Lensless Imaging of Extended Objects," *Physical Review Letters*, vol. 98, p. 034801, jan 2007.

[57] A. M. Maiden, J. M. Rodenburg, and M. J. Humphry, "Optical ptychography: a practical implementation with useful resolution," *Optics letters*, vol. 35, pp. 2585–7, aug 2010.

[58] A. Jesacher, C. Roider, and M. Ritsch-Marte, "Enhancing diffractive multi-plane microscopy using colored illumination," *Optics express*, vol. 21, pp. 11150–61, may 2013.

[59] S. Witte, V. T. Tenner, D. W. E. Noom, and K. S. E. Eikema, "Lensless diffractive imaging with ultra-broadband table-top sources: from infrared to extreme-ultraviolet wavelengths," *Light: Science & Applications*, vol. 3, p. e163, mar 2014.

[60] B. Rappaz, P. Marquet, E. Cuche, Y. Emery, C. Depeursinge, and

P. J. Magistretti, "Measurement of the integral refractive index and dynamic cell morphometry of living cells with digital holographic microscopy," *Optics Express*, vol. 13, no. 23, p. 9361, 2005.

[61] L. Tian, J. Wang, and L. Waller, "3D differential phase-contrast microscopy with computational illumination using an LED array," *Optics letters*, vol. 39, pp. 1326–9, mar 2014.

[62] I. Sencan, A. F. Coskun, U. Sikora, and A. Ozcan, "Spectral demultiplexing in holographic and fluorescent on-chip microscopy," *Scientific reports*, vol. 4, p. 3760, jan 2014.

[63] O. Mudanyali, D. Tseng, C. Oh, S. O. Isikman, I. Sencan, W. Bishara, C. Oztoprak, S. Seo, B. Khademhosseini, and A. Ozcan, "Compact, light-weight and cost-effective microscope based on lensless incoherent holography for telemedicine applications," *Lab on a chip*, vol. 10, pp. 1417–28, jun 2010.

[64] M. Reed Teague, "Deterministic phase retrieval: a Green's function solution," *Journal of the Optical Society of America*, vol. 73, p. 1434, nov 1983.

[65] A. Greenbaum and A. Ozcan, "Maskless imaging of dense samples using pixel super-resolution based multi-height lensfree on-chip microscopy," *Optics express*, vol. 20, pp. 3129–43, jan 2012.

[66] K. A. Nugent, "X-ray noninterferometric phase imaging: a unified picture," *Journal of the Optical Society of America A*, vol. 24, p. 536, feb 2007.

[67] H. Kogelnik and T. Li, "Laser beams and resonators," *Applied optics*, vol. 5, pp. 1550–67, oct 1966.

[68] D. W. E. Noom, S. Witte, J. Morgenweg, R. K. Altmann, and K. S. E. Eikema, "High-energy, high-repetition-rate picosecond pulses from a quasi-CW diode-pumped Nd:YAG system," *Optics letters*, vol. 38, pp. 3021–3, aug 2013.

[69] S. Witte, R. T. Zinkstok, A. L. Wolf, W. Hogervorst, W. Ubachs, and K. S. E. Eikema, "A source of 2 terawatt, 2.7 cycle laser pulses based on noncollinear optical parametric chirped pulse amplification," *Optics Express*, vol. 14, p. 8168, sep 2006.

[70] M. Schulz, R. Riedel, A. Willner, T. Mans, C. Schnitzler, P. Russbueldt, J. Dolkemeyer, E. Seise, T. Gottschall, S. Hädrich,

S. Duesterer, H. Schlarb, J. Feldhaus, J. Limpert, B. Faatz, A. Tünnermann, J. Rossbach, M. Drescher, and F. Tavella, "Yb:YAG Innoslab amplifier: efficient high repetition rate subpicosecond pumping system for optical parametric chirped pulse amplification," *Optics Letters*, vol. 36, p. 2456, jun 2011.

[71] J. Tümmler, R. Jung, H. Stiel, P. V. Nickles, and W. Sandner, "High-repetition-rate chirped-pulse-amplification thin-disk laser system with joule-level pulse energy," *Optics Letters*, vol. 34, p. 1378, apr 2009.

[72] A. H. Curtis, B. A. Reagan, K. A. Wernsing, F. J. Furch, B. M. Luther, and J. J. Rocca, "Demonstration of a compact 100 Hz, 0.1 J, diode-pumped picosecond laser," *Optics Letters*, vol. 36, p. 2164, jun 2011.

[73] S. Klingebiel, C. Wandt, C. Skrobol, I. Ahmad, S. A. Trushin, Z. Major, F. Krausz, and S. Karsch, "High energy picosecond Yb:YAG CPA system at 10 Hz repetition rate for pumping optical parametric amplifiers," *Optics Express*, vol. 19, p. 5357, mar 2011.

[74] K.-H. Hong, J. T. Gopinath, D. Rand, A. M. Siddiqui, S.-W. Huang, E. Li, B. J. Eggleton, J. D. Hybl, T. Y. Fan, and F. X. Kärtner, "High-energy, kHz-repetition-rate, ps cryogenic Yb:YAG chirped-pulse amplifier," *Optics Letters*, vol. 35, p. 1752, may 2010.

[75] D. A. Rand, S. E. J. Shaw, J. R. Ochoa, D. J. Ripin, A. Taylor, T. Y. Fan, H. Martin, S. Hawes, J. Zhang, S. Sarkisyan, E. Wilson, and P. Lundquist, "Picosecond pulses from a cryogenically cooled, composite amplifier using Yb:YAG and Yb:GSAG," *Optics Letters*, vol. 36, p. 340, jan 2011.

[76] D. E. Miller, L. E. Zapata, D. J. Ripin, and T. Y. Fan, "Sub-picosecond pulses at 100 W average power from a Yb:YLF chirped-pulse amplification system," *Optics Letters*, vol. 37, p. 2700, jun 2012.

[77] F. Tavella, A. Marcinkevicius, and F. Krausz, "90 mJ parametric chirped pulse amplification of 10 fs pulses," *Optics Express*, vol. 14, p. 12822, dec 2006.

[78] S. Witte, R. T. Zinkstok, W. Hogervorst, and K. S. E. Eikema, "Generation of few-cycle terawatt light pulses using optical parametric chirped pulse amplification," *Optics Express*, vol. 13,

p. 4903, jun 2005.

[79] W. Koechner, *Solid-State Laser Engineering (Springer Series in Optical Sciences)*. Springer, 1999.

[80] Q. Lü, N. Kugler, H. Weber, S. Dong, N. Müller, and U. Wittrock, "A novel approach for compensation of birefringence in cylindrical Nd: YAG rods," *Optical and Quantum Electronics*, vol. 28, pp. 57–69, jan 1996.

[81] H. N. Chapman and K. A. Nugent, "Coherent lensless X-ray imaging," *Nature Photonics*, vol. 4, pp. 833–839, dec 2010.

[82] A. Sakdinawat and D. Attwood, "Nanoscale X-ray imaging," *Nature photonics*, 2010.

[83] S. O. Isikman and W. Bishara, "Lens-free optical tomographic microscope with a large imaging volume on a chip," *Proceedings of the National Academy of Sciences of the United States of America*, 2011.

[84] J. Miao, P. Charalambous, J. Kirz, and D. Sayre, "Extending the methodology of X-ray crystallography to allow imaging of micrometre-sized non-crystalline specimens," *Nature*, 1999.

[85] I. McNulty, J. Kirz, and C. Jacobsen, "High-resolution imaging by Fourier transform x-ray holography," *Science*, 1992.

[86] S. Marchesini, H. He, and H. N. Chapman, "X-ray image reconstruction from a diffraction pattern alone," *Physical Review B*, 2003.

[87] B. Abbey, K. A. Nugent, G. J. Williams, and J. N. Clark, "Keyhole coherent diffractive imaging," *Nature Physics*, 2008.

[88] P. Thibault, M. Dierolf, A. Menzel, and O. Bunk, "High-resolution scanning x-ray diffraction microscopy," *Science*, 2008.

[89] S. Marchesini, S. Boutet, and A. E. Sakdinawat, "Massively parallel X-ray holography," *Nature Photonics*, 2008.

[90] T. Popmintchev, M. C. Chen, and D. Popmintchev, "Bright coherent ultrahigh harmonics in the keV x-ray regime from mid-infrared femtosecond lasers," *science*, 2012.

[91] R. L. Sandberg and C. Song, "High numerical aperture tabletop soft x-ray diffraction microscopy with 70-nm resolution," *Proceed-*

ings of the National Academy of Sciences of the United States of America, 2008.

[92] R. L. Sandberg and D. A. Raymondson, "Tabletop soft-x-ray Fourier transform holography with 50 nm resolution," *Optics letters*, 2009.

[93] A. S. Morlens, J. Gautier, and G. Rey, "Submicrometer digital in-line holographic microscopy at 32 nm with high-order harmonics," *Optics letters*, 2006.

[94] A. Ravasio, D. Gauthier, F. Maia, and M. Billon, "Single-shot diffractive imaging with a table-top femtosecond soft x-ray laser-harmonics source," *Physical Review Letters*, 2009.

[95] M. Wieland, R. Frueke, and T. Wilhein, "Submicron extreme ultraviolet imaging using high-harmonic radiation," *Applied Physics Letters*, 2002.

[96] M. D. Seaberg and D. E. Adams, "Ultrahigh 22 nm resolution coherent diffractive imaging using a desktop 13 nm high harmonic source," *Optics express*, 2011.

[97] B. Chen, R. A. Dilanian, and S. Teichmann, "Multiple wavelength diffractive imaging," *Physical Review A*, 2009.

[98] A. D. Parsons and R. T. Chapman, "90 nm resolution reconstruction from a polychromatic signal using monochromatic phase retrieval techniques," *CLEO/Europe and EQEC 2011 Conference Digest*, 2011.

[99] B. Abbey, L. W. Whitehead, and H. M. Quiney, "Lensless imaging using broadband X-ray sources," *Nature Photonics*, 2011.

[100] E. D. Becker and T. C. Farrar, "Fourier Transform Spectroscopy New methods dramatically improve the sensitivity of infrared and nuclear magnetic resonance spectroscopy," *Science*, 1972.

[101] A. D. Yablon, "Multi-wavelength optical fiber refractive index profiling by spatially resolved Fourier transform spectroscopy," *Journal of Lightwave Technology*, 2010.

[102] V. F. Paz and S. Peterhänsel, "Solving the inverse grating problem by white light interference Fourier scatterometry," *Light: Science & Applications*, 2012.

[103] G. J. Williams, H. M. Quiney, and B. B. Dhal, "Fresnel coherent diffractive imaging," *Physical Review Letters*, 2006.

[104] H. M. Quiney, K. A. Nugent, and A. G. Peele, "Iterative image reconstruction algorithms using wave-front intensity and phase variation," *Optics letters*, 2005.

[105] T. Latychevskaia and H. W. Fink, "Solution to the twin image problem in holography," *Physical review letters*, 2007.

[106] B. Zhang, M. D. Seaberg, and D. E. Adams, "Full field tabletop EUV coherent diffractive imaging in a transmission geometry," *Optics express*, 2013.

[107] L. Chan, M. Siemens, and M. M. Murnane, "Ultrafast demagnetization dynamics at the M edges of magnetic elements observed using a tabletop high-harmonic soft x-ray source," *Physical Review Letters*, 2009.

[108] S. Roy, D. Parks, K. A. Seu, R. Su, and J. J. Turner, "Lensless X-ray imaging in reflection geometry," *Nature Photonics*, 2011.

[109] M. Kovačev, S. V. Fomichev, and E. Priori, "Extreme ultraviolet Fourier-transform spectroscopy with high order harmonics," *Physical Review Letters*, 2005.

[110] N. D. Oliveira, M. Roudjane, and D. Joyeux, "High-resolution broad-bandwidth Fourier-transform absorption spectroscopy in the VUV range down to 40 nm," *Nature Photonics*, 2011.

[111] C. M. Günther, B. Pfau, R. Mitzner, B. Siemer, S. Roling, H. Zacharias, O. Kutz, I. Rudolph, D. Schondelmaier, R. Treusch, and S. Eisebitt, "Sequential femtosecond X-ray imaging," *Nature Photonics*, vol. 5, pp. 99–102, jan 2011.

[112] D. Brida, C. Manzoni, and G. Cerullo, "Phase-locked pulses for two-dimensional spectroscopy by a birefringent delay line," *Optics letters*, 2012.

Summary

Microscopes have been giving us insight into biological processes for centuries, and enable us to view small structures in solid materials. To view even smaller structures, many new techniques have been developed, one of which is the use of short wavelengths in the illuminating source. In this thesis a laser system is described which is developed to generate short wavelengths. This is done by using high-harmonic generation, which requires short light pulses. We also describe how to use these wavelengths in a microscope, despite the lack of materials with high refraction and low losses to make lenses. These lensless microscopes have also been tested with visible light, which provides for easily configurable, cheap microscopes.

We have done lensless microscopy with visible and infrared light by using CCD-chips, phase retrieval algorithms and computers to process this information. The CCD-chips capture light that has passed through a sample and measure the intensity pattern a small distance away. What should be calculated is the intensity as close to the sample as possible. The light intensity alone is not enough to achieve this. Phase information is also needed, and this can be gathered by comparing the intensity pattern at two different wavelengths. For this, the light needs to have a well defined phase, for which we use a laser.

We have performed experiments where we first turned on a laser which shines through a sample. Then we measure the intensity, turn off the laser and repeat this process with lasers emitting different colors. Then this information is used to calculate what the sample looks like.

The calculation goes as follows: first the intensity information is combined with random phase information. Together this gives an electric field of the light at a certain wavelength. From this field it is calculated what the field should look like at another wavelength. There the calculated intensity from the electric field is replaced by the measured intensity. After that, this process of wavelength transformation and intensity replacement is repeated a few times. This gives the phase information we need for the reconstruction of the image of the sample. The quantitative phase information itself can also be used to determine the structure of the sample.

This process is used on a test sample with a known image with different sizes and well defined edges to check if it works. Thereafter a neuron sample is used to show that it does not only work with simple samples but also with more subtle structures. Here it is also visible that the phase information shows clearer structures than the intensity. A transverse resolution of less than 2 micrometers is achieved.

Because this measurement process is slow and clumsy, we then used an RGB-sensor for the intensity measurements. In this way, all intensity information can be measured in one take, and the measurement time is only limited by the minimal shutter time of the measurement chip and the intensity of the lasers, and not by the time between takes. We have made videos of flowing beads and moving worms with a resolution better than 2.2 micrometers. In chapter 4 we also discuss that the size of an image is dependent on the illuminating wavefront, and the consequences thereof for the reconstruction.

After the lensless microscopy we discuss the generation of short wavelengths to see smaller things. The laser system for generating short wavelengths consists of multiple components which generate, shape and amplify pulses. One component is a pulsed laser based on a titanium doped sapphire crystal. This laser gives pulses with a wavelength around 800 nanometer and a pulse length of about 30 femtoseconds.

We then need a system to amplify the 800 nanometer pulses, of which the development is described in chapter 5. The starting point is that pulses are generated in a neodymium doped yttrium vanadate laser. These pulses are amplified in a regenerative amplifier, where a pulse is sent through a crystal multiple times to amplify it, and then sent out whole. There is also an etalon in the regenerative amplifier, which causes different wavelengths to travel different optical path lengths, which stretches the pulse.

After the regenerative amplifier these pulses pass through an amplifier where a pulse goes back and forth through a crystal in two amplifier modules. These modules are pulsed pumped by diodes, specially designed to withstand fast changing currents without breaking. A lot of heat is produced by the diodes, which deforms the crystals. This deformation causes radial birefringence, which then deforms the pulses, and to compensate for this the polarization of the pulses is rotated and the pulses are sent back through the same crystal. After the pulses have passed twice through both amplifier modules, this gives 130 millijoule pulses of 64 picoseconds with a wavelength of 1064 nanometer and a repetition frequency of 300 pulses per second.

Subsequently, the frequency of the light is doubled and we get 75 millijoule pulses with a wavelength of 532 nanometers. This green light is then used to amplify the femotsecond pulses in a non-collinear optical parametric chirped pulse amplifier. For this the pulses are chirped first, which means they are stretched by letting different wavelengths travel different distances using gratings. After stretching these pulses are sent through a crystal together with the green pulses, where direct energy transfer takes place from the green beam to the stretched pulses, with minimal absorption of light in the crystal. Those amplified pulses are compressed again using gratings so they can be used in high-harmonic generation. After compression we have 4 millijoule pulses. By focusing these pulses in a noble gas we can generate light at much shorter wavelengths using high-harmonic generation.

By combining radiation with short wavelengths with lensless microscopy we can in principle achieve a higher resolution. In chapter 6 we describe how this is realized with a borrowed laser, because the laser described in chapter 5 was not available at the time.

A difference between a visible light source, and one which uses short wavelengths generated by high harmonic generation, is that the second one contains multiple wavelength peaks so we cannot directly use the phase reconstruction algorithm. Because we cannot simply distinguish wavelengths like with the RGB-sensor, we need another technique.

The technique to split images up in wavelengths is derived from Fourier transform spectroscopy. In this case a beam is split up in two, with an adjustable path length difference between the two (overlapping) beams. Then multiple measurements are done with different path length differences, and via a Fourier transform the images at different wavelengths are extracted.

With this technique we did test measurements with a broadband source on a test sample, a root of a lily of the valley, and a reflection measurement on another test sample. With high harmonics of around 50 nanometers wavelength we made a transmission image of a 300 nanometers thin aluminium foil with a nickel grid. With these experiments we show for the first time that lensless microscopy is also possible with a broadband spectrum in the extreme ultraviolet, like those generated using high harmonic generation. We expect that this will also enable lensless microscopy with high-harmonic sources with much smaller wavelengths of a few nanometers.

Samenvatting

Microscopen geven ons al eeuwen inzicht in biologische processen en maken het mogelijk om kleine structuren in vaste stoffen te bekijken. Om nog kleinere structuren te kunnen bekijken zijn steeds nieuwe technieken ontwikkeld, en een daarvan is het gebruiken van kortere golflengtes als lichtbron. In dit werk wordt een lasersysteem beschreven dat er op gericht is om licht van korte golflengtes te maken. Dit gebeurt door hogeharmonischegeneratie, waarvoor korte intense lichtpulsen nodig zijn. Er wordt ook beschreven hoe deze golflengtes te gebruiken zijn voor een microscoop ondanks het gebrek aan materialen met de hoge breking en lage absorptie voor lenzen. Deze lensloze microscopen zijn ook getest met zichtbaar licht, wat voor een makkelijk instelbare, goedkope microscoop zorgt.

Wij hebben lensloze microscopie met zichtbaar en infrarood licht gedaan door gebruik te maken van CCD-chips, fasebepalingsalgoritmes, en computers om deze informatie snel te kunnen verwerken. De CCD-chips vangen licht op wat door een monster is gegaan, en meten de lichtintensiteit een stukje verderop. Wat uiteindelijk berekend moet worden is de lichtintensiteit zo vlak mogelijk na het monster. Het lichtpatroon op de CCD alleen is niet genoeg om dit te berekenen. Fase-informatie is ook nodig, en deze kan verkregen worden door de lichtintensiteit bij twee verschillende golflengtes te vergelijken. De lichtbron moet een goed gedefinieerde fase hebben, waarvoor wij een laser gebruiken.

We hebben experimenten uitgevoerd waarbij we eerst een laser aan hebben gezet die door een monster schijnt. Daarna nemen we een intensiteitsmeting, zetten we de laser uit en herhalen we dit proces met een lasers van andere kleuren. Vervolgens wordt met deze informatie berekend hoe het monster er uit ziet.

De berekening gaat als volgt: eerst wordt de intensiteitsinformatie gecombineerd met een willekeurige fase-informatie. Dit geeft samen een elektrisch veld bij een bepaalde golflengte. Vanuit dit veld wordt berekend hoe dit veld er uit hoort te zien bij een andere golflengte. Daar wordt de berekende intensiteit vervangen door de gemeten intensiteit. Vervolgens wordt dit proces van transformeren van golflengtes en vervanging van intensiteitsinformatie enkele keren herhaald. Dit levert de

fase-informatie op die we nodig hebben voor de reconstructie van het beeld van het monster. De quantitatieve fase-informatie zelf kan ook gebruikt worden om de structuur van het monster te bepalen.

Dit proces is uitgevoerd op een voorbeeldmonster met een bekend beeld met verschillende groottes en goed gedefinieerde randen om te testen of het werkt. Daarna is een neuronenmonster gebruikt om te laten zien dat het niet alleen werkt bij simpele monsters, maar ook bij subtielere structuren. Hierbij is ook te zien dat de fase-informatie duidelijkere structuren laat zien dan de intensiteit. Een transversale resolutie van minder dan 2 micrometer is verkregen.

Omdat dit meetproces traag en onhandig is hebben we daarna een RGB-sensor gebruikt voor intensiteitsmetingen. Op deze manier kan alle intensiteitsinformatie in één keer genomen worden, en wordt de meettijd alleen nog maar beperkt door de minimale sluitertijd van de CCD-chip en de intensiteit van de lasers, en niet meer door de tijd tussen verschillende opnames. We hebben hiermee videobeelden gemaakt van stromende balletjes en bewegende wormen met een resolutie onder de 2,2 micrometer. In hoofdstuk 4 bediscussiëren we ook dat de grootte van de afbeelding afhankelijk is van het belichtende golffront en de gevolgen hiervan op de reconstructie.

Na de lensloze microscopie wordt het genereren van korte golflengtes besproken om kleinere structuren te kunnen zien. Het lasersysteem voor het genereren van korte golflengten bestaat uit verscheidene componenten die pulsen genereren, vervormen en versterken. Een component daarvan is een gepulste laser op basis van een saffierkristal gedoteerd met titanium. Deze geeft pulsen met een golflengte rond 800 nanometer met een pulsduur rond 30 femtoseconden.

Vervolgens is er een systeem nodig om de 800 nanometer pulsen te versterken, waarvan de ontwikkeling wordt beschreven in hoofdstuk 5. Het startpunt is dat eerst pulsen gemaakt worden in een neodymium gedoteerde yttriumvanadaatlaser. Deze pulsen worden versterkt in een regeneratieve versterker, waarin een puls meerdere keren door een kristal worden gestuurd om het te versterken, waarna de puls in zijn geheel weer naar buiten wordt gestuurd. In de regeneratieve versterker zit ook nog een etalon, waardoor verschillende golflengtes een verschillende optische padlengte afleggen en de puls verlengt wordt.

Na de regeneratieve versterker gaan deze pulsen door een versterker waarbij een puls heen en terug door een kristal gaat in twee versterkermodules. Deze modules worden gepulst gepompt door diodes, speciaal ontwikkeld om snel wisselende stromen te weerstaan zonder kapot te

gaan. Er wordt hierbij veel warmte ontwikkeld die voor vervorming van de kristallen zorgt. Door deze vervorming wordt radiële dubbelbrekendheid in het kristal geïnduceerd. Deze vervormt daarop weer de pulsen, en om hiervoor te compenseren wordt de polarisatie van de pulsen gedraaid en de pulsen teruggestuurd door hetzelfde kristal. Nadat de pulsen twee keer door de twee versterkingsmodules zijn gegaan levert dit 130 millijoule pulsen op van 64 picoseconden lang met 1064 nanometer golflengte, en met een herhalingsfrequentie van 300 pulsen per seconde.

Dan wordt de frequentie van het licht verdubbeld en verkrijgen we 75 millijoule pulsen met een golflengte van 532 nanometer. Dit groene licht wordt dan gebruikt om de femtosecondepulsen te versterken in een niet-collineaire optische parametrische getjilptepulsversterker. Hiervoor worden de femtoseconde pulsen eerst getjilpt, dat willen zeggen uitgerekt door verschillende golflengtes een verschillende afstand af te laten leggen met behulp van tralies. Na het uitrekken worden deze pulsen samen met de groene pulsen door een kristal gestuurd waar directe energieoverdracht plaatsvind van de groene naar de uitgerekte pulsen met minimale absorptie van licht in het kristal. Hierna worden de zojuist versterkte pulsen weer gecomprimeerd met behulp van tralies zodat ze gebruikt kunnen worden in hogeharmonischegeneratie. Na compressie zijn pulsen van 4 millijoule verkregen. Door deze pulsen in een edelgas te focusseren kan vervolgens via hogeharmonischegeneratie licht bij veel kortere golflengtes gemaakt worden.

Door het combineren van straling met korte golflengtes en microscopie zonder lenzen kunnen we in principe een hogere resolutie halen. In hoofstuk 6 wordt beschreven hoe dit gerealiseerd is met behulp van een geleende laser, omdat de laser beschreven in dit proefschrift in hoofstuk 5 toen nog niet beschikbaar was.

In tegenstelling tot lichtbronnen voor zichtbaar licht, die heel precies een enkele kleur kunnen geven, bestaat licht bij korte golflengtes gemaakt door hogeharmonischegeneratie uit vele kleuren (harmonischen), zodat we daarvoor niet meer direct het faseberekeningsalgoritme kunnen gebruiken. Omdat we niet simpel zoals bij de RGB-sensor golflengtes kunnen onderscheiden hebben we een andere techniek nodig.

Deze techniek om beelden op te splitsen naar golflengte is afgeleid van Fourier-transformatiespectroscopie. In dit geval wordt een lichtbundel opgesplitst in tweeën, met een instelbaar weglengteverschil tussen de twee (overlappende) bundels. Dan worden er meerdere metingen gedaan met meerdere weglengteverschillen en via een Fourier-transformatie wordt hieruit gehaald wat het beeld is bij de verschillende golflengtes.

Met deze techniek hebben we testmetingen gedaan met een breedbandige bron op een testmonster, een lelietje-van-dalenwortel, en een reflectiemeting op een ander testmonster. Met hoge harmonischen rond 50 nanometer golflengte hebben we een afbeelding kunnen maken in transmissie van een 300 nanometer dun aluminiumfolie met een nikkelrooster. Met deze experimenten is voor het eerst aangetoond dat lensloze microscopie ook mogelijk is met een breedbandig spectrum in het extreem ultraviolet zoals dat wordt gemaakt via hogeharmonischegeneratie. Het is de verwachting dat dit ook lensloze microscopie met hogeharmonischebronnen mogelijk zal maken bij nog veel kortere golflengtes van een paar nanometer.

Acknowledgements

Kjeld, dankzij jouw colleges niet-lineaire optica heb ik besloten te gaan promoveren. Je hebt me leren lasers bouwen, hoewel ik dat altijd net wat slordiger aan zal pakken dan jij zou willen. Elke keer kon je me weer wat verder brengen als je langskwam. Al probeerde je graag uit te stralen dat je geen tijd had, als ik stiekem toch wat te vragen had gaf je altijd antwoord. Dank je voor je anekdotes, je teslatransformator-show, je prachtige kerstkaart, en de uitjes naar München samen met de frequentiekamclub. Het was mooi om te zien hoe je bijvoorbeeld aan de Verdi sleutelde, en dat je nog steeds het liefst in het lab wil zijn. Moge de natuurkundige in je nog lang stand houden tegen de overweldigende bureaucratie.

Stefan, dank je wel voor al je hulp. Hoe hard je ook aan het werk was met andere dingen, ik kon altijd bij je aankloppen. Ik zal proberen niet de bescheidenheid uit je te praten, maar je verdient heel veel lof voor al je werk, je hulp, en je vriendelijkheid.

Jonas, I wish we could have had more time to work together, but we were always too busy. I'm happy we compensated a little bit by hanging out in Berlin.

Robert, ik was niet echt in een goede bui toen je mee kwam helpen. Dank je wel dat je me er doorheen hebt geholpen door samen met mij aan de laser te knutselen.

Vasco, ik was soms een beetje jaloers op je doortastendheid, maar werd dan weer een beetje gerustgesteld als je bijvoorbeeld totaal onnodig een groot brok metaal ergens af zaagde. Je hebt enorm veel werk verzet in de tijd dat je bij ons was, en ik hoop dat je je enthousiasme nooit verliest.

Dirk, na een studie natuurkunde dacht ik dat ik al heel wat bijzondere mensen gezien had. Ik ben nog steeds niet helemaal over de schok heen. Dank je voor de leuke samenwerking en je danspartners.

Elias, we vertelden je ongeveer wat we van plan waren en even later stond er alweer wat klaar wat we konden gebruiken. Indrukwekkend!

Martijn, lieverd, mijn steun en toeverlaat, dank je voor je werk aan ons algoritme, maar ook voor je magische bank waar ik maar een paar uur op hoefde te zitten om alles weer een beetje dragelijk te maken.

Tom, je hielp me er aan herinneren hoe leuk ik het vind om over dingen na te denken toen ik alleen nog maar bezig was met spiegeltjes goed positioneren.

Jeroen, als mijn master niet zo leuk was geweest was ik nooit aan mijn promotie begonnen. Je hebt me ontzettend veel geleerd.

Jacques, dank je wel voor al je werk, alles wat ik van je geleerd heb, en je verhalen.

Rob, als ik iets gedaan wilde hebben deed je altijd eerst alsof het totaal idioot was wat ik je vroeg, en vervolgens was het een half uurtje later klaar. Heel erg bedankt voor al je werk.

Ik wil ook nog de mensen van de elektronica en fijnmechanische instrumentatie bedanken. Jullie leveren een heel belangrijke bijdrage aan de wetenschap. Als er op jullie bezuinigd wordt gaat iedereen er op achteruit.

I want to thank the whole group for the many many times you helped me out and good times we had. Playing games, skiing, seeing you fall down a cliff, seeing your newborn babies, you showing me your contraptions so I felt less worried about mine, all the stories about physics and the rest of the world, it was all a lot of fun. I can't thank you enough for all your help. I'm sorry for all the complaining I did the last years. I am still amazed there are always so many nice people in the group. Either the world is just a very nice place, or we have some great selection criteria (even though I slipped through the cracks).

Wim U., ik voelde me vanaf het begin welkom in de groep, toen ik aan je vroeg of ik iets met lasers kon doen. Dank je wel voor de enorme hoeveelheid werk die je doet om er voor te zorgen dat wij onze gang kunnen gaan.

Ik wil ook iedereen bedanken voor het gewoon met me rondhangen, tv kijken, ronddansen, rondklimmen, samen bandjes kijken, bliepjes maken, en die hele rambam. Zelfs al hebben we het helemaal niet over mijn werk gehad, je hebt er toch aan meegeholpen. Al die arme mensen die hun naam hier niet zien, je bent heus wel belangrijk voor me. Samen cocktails drinken in een zwembad klinkt niet productief, maar even pauze nemen kan soms best een goed idee zijn, zelfs als je zo snel mogelijk je laserstraalkanon af wil hebben.

There is also a huge amount of people who helped with this thesis whom I have never even met, but will maybe accidentally read this some day. Thanks for the open source software, the free educational videos, helpful instructions and blog posts on all kinds of websites, and lots more.

Marion, Wim, Hans, Karina, bedankt voor alles. Zonder jullie was het helemaal niks met me geworden. Ook de rest van mijn familie, ooms, tantes, neven, nichten, oma's, schoonzus, zwager, heel erg bedankt. Jullie geven me het gevoel dat dat jullie er altijd voor me zijn en dat het allemaal wel goed komt. Mike, Nick, Amy, ik zou graag de wijze oude man willen uithangen, maar zolang jullie vrolijk blijven rondspringen heb ik jullie weinig adviezen te geven.